COLLOIDAL OPTOELECTRONICS OF SELF-ASSEMBLED QUANTUM WELL SUPERSTRUCTURES

A DISSERTATION SUBMITTED TO
THE GRADUATE SCHOOL OF ENGINEERING AND SCIENCE
OF BILKENT UNIVERSITY
IN PARTIAL FULFILLMENT OF THE REQUIREMENTS FOR
THE DEGREE OF
DOCTOR OF PHILOSOPHY
IN
ELECTRICAL AND ELECTRONICS ENGINEERING

By
Onur Erdem
June 2020

COLLOIDAL OPTOELECTRONICS OF SELF-ASSEMBLED QUANTUM WELL SUPERSTRUCTURES

By Onur Erdem

June 2020

We certify that we have read this dissertation and that in our opinion it is fully adequate, in scope and in quality, as a dissertation for the degree of Doctor of Philosophy.

Hilmi Volkan Demir(Advisor)

Nihan Kosku Perkgöz

Vakur Behçet Ertürk

Fatih Ömer İlday

Alphan Sennaroğlu

Approved for the Graduate School of Engineering and Science:

Ezhan Karaşan
Director of the Graduate School

ABSTRACT

COLLOIDAL OPTOELECTRONICS OF SELF-ASSEMBLED QUANTUM WELL SUPERSTRUCTURES

Onur Erdem
Ph.D. in Electrical and Electronics Engineering
Advisor: Hilmi Volkan Demir
June 2020

Advances in the colloidal nanocrystal synthesis enabled creation of quasi two-dimensional colloidal quantum wells (CQWs) in the last decade. These CQWs possess similar properties to those of epitaxially grown quantum wells while at the same time offering the benefits of low-cost synthesis and solubility in various solvents. Their atomically precise thickness and one-dimensional quantum confinement grant them favorable properties such as narrow emission linewidth, reduced inhomogeneous broadening and giant oscillator strength. In addition, due to their quasi-two dimensional shape, they display intrinsic anisotropy. Because of this anisotropy, the particle interactions in closely packed films depend greatly on the orientation of these CQWs. To fully utilize the interaction of CQWs with each other or with other particles in their proximity, we develop a self-assembly technique, which is used to deposit highly uniform thin CQW films onto various solid substrates. This self-assembly technique allows us to deposit CQWs as a continuous monolayer while at the same time controlling their orientation throughout the substrate, thereby modifying their packing factor as well as near-field dipole-dipole interactions. This self-assembly technique is also employed to create large-area CQW films of any desired thickness, simply by applying the same deposition technique on the same substrate as many times as desired. We use these self-assembled CQW films to study the two main aspects of nanocrystal optoelectronics, namely, Förster resonance energy transfer (FRET) and optical gain, with CQWs. By using the orientation-controlled CQW monolayers, we show that the rate of FRET from colloidal quantum dots (QDs) to a monolayer of CQWs can be tuned via dipole-dipole interactions between QDs and CQWs. We use Förster's theory of nonradiative energy transfer while taking into account the anisotropy of the excitonic CQW excitonic state as well as its delocalization throughout the CQW to account for our results. Next, we show that our multilayered CQW films display optical gain in uncharacteriscally low thicknesses

(as small as 40 nm) due to the tight packing and extremely uniform deposition of the CQWs. We furthermore study systematically the observed threshold of amplified spontaneous emission (ASE) in these CQW multilayers as a function of the film thickness (i.e., the number of monolayers), and demonstrate that the gain threshold drops with increasing thickness, accompanied by the red-shift of the ASE peak. These trends can be explained by the varying degree of optical mode confinement, which is a function of both the film thickness as well as the wavelength of propagating mode. Our self-assembly technique allows to study and make use of the favorable properties of the CQWs including anisotropy and enhanced optical gain. Since this technique enables us to produce large-area films displaying excellent homogeneity, it can be a benchmark building block for creating device-scale 2- or 3-dimensional superstructures from CQWs as well as from other types of colloidal nanocrystals to be utilized in both in- and out-of-plane optical applications.

Keywords: colloidal quantum wells, nanocrystals, self-assembly, nonradiative energy transfer, optical gain, thin films.

ÖZET

ÖZDİZİLİ KUANTUM KUYUSU ÜSTYAPILARININ KOLOİDAL OPTOELEKTRONİĞİ

Onur Erdem
Elektrik ve Elektronik Mühendisliği, Doktora
Tez Danışmanı: Hilmi Volkan Demir
Haziran 2020

Koloidal nanokristal sentezindeki gelişmeler, iki boyutlu benzeri koloidal kuantum kuyularının (KKK'lerin) üretilebilmesini sağlamıştır. Bu KKK'ler yüzeyde büyütülen ince-film kuantum kuyularına benzer özellikler sergilemekle birlikte, düşük maliyetle sentezlenebilme ve çeşitli çözücülerde işlenme avantajlarına da sahiptirler. Atomik düzeyde yassı olmaları ve tek boyutlu kuantum kısıtlanmaları, KKK'lerin dar ışıma aralığına, düşük heterojen genişlemeye ve dev salınım şiddetine sahip olmasını sağlamaktadır. Ek olarak, iki boyutlu benzeri şekilleri nedeniyle içsel eşyönsüzlüğe sahiptirler. Bu eşyönsüzlük nedeniyle, sık yapılı filmlerindeki parçacık etkileşimleri büyük oranda bu KKK'lerin oryantasyonuna bağlıdır. KKK'lerin birbirleriyle veya yakınlarındaki başka parçacıklarla etkileşimini etkin bir biçimde kullanabilmek amacıyla, yüksek oranda tekdüzeliğe sahip KKK filmlerini çeşitli katı altlıklar üzerine kaplayabildiğimiz bir özdizilim tekniği geliştirdik. Bu özdizilim tekniği, KKK'leri sürekli bir tekkatman halinde kaplamamızı sağlarken, aynı zamanda onların bütün film boyunca oryantasyonlarını kontrol edebilmemize, böylece sıklıklarını ve yakın-alan dipol etkileşimlerini ayarlamamıza da olanak tanımaktadır. Bu özdizilim tekniğini, aynı zamanda, aynı altlığa istenilen sayıda arka arkaya uygulanarak, istenen kalınlıkta KKK filmlerinin büyük alanlara kaplanması için de kullandık. Bu özdizili filmler aracılığıyla, nanokristal optoelektroniğini iki farklı bağlamda inceledik: KKK'lerin Förster rezonans enerji transferi (FRET) ve optik kazancı. Oryantasyon kontrollü KKK tekkatmanları ile, koloidal kuantum noktalarından (KN'lerden) KKK'lere olan FRET'in, aralarındaki dipol etkileşimleri ile kontrol edilebileceğini gösterdik. Sonuçlarımızı açıklayabilmek için Förster'in ışınımsız enerji transferi kuramini, KKK eksiton dalga fonksiyonunun yayılmış ve eşyönsüz olmasını hesaba katarak kullandık. Ayrıca, çokkatmanlı KKK filmlerimizin, sık dizilim ve aşırı tekdüzelikleri sayesinde alışılmıştan çok düşük (yaklaşık 40 nm) kalınlıklarda optik kazanç sergileyebildiklerini gösterdik. Bu filmlerdeki

kendiliğinden ışıma yükseltilmesi (ASE) eşiğinin film kalınlığına (yani katman sayısına) göre değişimini sistematik olarak çalıştık ve film kalınlığının artmasıyla beraber kazanç eşiğinin düştüğünü ve ASE dalgaboyunun da kırmızıya kaydığını gösterdik. Bu gözlemler, optik mod sıkışmasının hem film kalınlığına hem de mod dalgaboyuna bağlı sergilediği değişimlerle açıklanabilmektedir. Özdizilim tekniğimiz, KKK'lerin eşyönsüzlük ve yüksek optik kazanç gibi elverişli özelliklerinin çalışılmasına ve kullanılmasına olanak tanımaktadır. Bu teknik, büyük alanlarda mükemmel tekdüzelik gösteren filmler üretebilmemizi mümkün kıldığından dolayı, KKK'ler veya diğer koloidal nanokristaller ile düzlem içi veya düzlem dışı optik uygulamalarda kullanılabilecek, cihaz ölçeğinde iki veya üç boyutlu üstyapıların inşa edilmesinde bir mihenk taşı olma potansiyeline sahiptir.

Anahtar sözcükler: koloidal kuantum kuyuları, nanokristaller, özdizilim, ışınımsız enerji transferi, optik kazanç, ince filmler.

Acknowledgement

In an afternoon at the end of the summer of 2011, I was sitting in a tiny, stuffy office in the company I was an intern for, half-listening to the advices of my internship supervisor about the life, future and such. It was my last day and I was counting minutes while trying to stay awake. His name was... Never mind, this is not personal.

Earlier, he had asked me what I wanted to do after I graduated. I had mentioned how exciting nanotechnology was to me, that I had recently joined a nanotechnology group in our department and that I wanted to go to graduate school and do research, because I loved science.

He laughed.

Do not get me wrong, he was always nice to me and we had no problems. But despite being the kind-hearted and helpful guy that he was, we had diverse views on what an engineering student should do after graduation. To him, grad school was not a reasonable option for an engineering student's career pathway. An Electrical and Electronics Engineering graduate, he said, should get a job at a military defence company, and start making money right away while "actually producing something". Graduate school research was "good for writing PhD theses but for nothing else". He really had not shattered my eagerness in any way; I was only sad (for him) because of the way he thought.

Today, I am happy to have realized what he said about the graduate school was an outright fabrication. It does not apply to our group anyways. I am proud to be part of many studies of ours, in which we created novel nanoparticles, fabrication techniques and devices, some of which are already patented and/or being used in various applications. It has been a delightful experience to see one work we created leading to another, one tool we developed opening up new possibilities and future directions, and solving one problem giving us one piece of puzzle while revealing that there are many more pieces than we thought to be looked for.

Of course, the point of this almost-10-year-long journey was not to prove wrong somebody I barely remember. Nor to make something somebody can make money off of. Nor to get the monthly free meal tickets given by the department (OK, maybe a little). The point was to make science, and only science.

Science is our tool to understanding everything going on around us. Science has been our means to survive by helping us make fire, finding our way in the middle of oceans, or developing vaccines. Science made it possible for us to achieve greatness in the form of gigantic square pyramids made of blocks weighing multiple tons, turbines that can convert the energy from a stream of water into electricity, or going to space. We owe science much more than we can ever realize. Science need more appreciation. I am here to appreciate science.

After seven years of graduate study for my MS and PhD degrees, about a couple of dozens of sleepovers at UNAM and nearly a thousand self-assemblies, I realize that our efforts to understand our scientific observations, regardless of whether we get an output from it or not, are always worth it.

I would like to sincerely thank Prof. Hilmi Volkan Demir for being the awesome advisor that he is and helping me become a better researcher through his excellent guidance, motivation and support. I am indebted to him for everything. I would like to thank Prof. Demir, Prof. Ayhan Altıntaş, Prof. Nihan Kosku Perkgöz and Prof. Vakur Behçet Ertürk for guiding me throughout my work as the members of my thesis committee. I would like to thank Prof. Demir, Prof. Kosku Perkgöz, Prof. Ertürk, Prof. Fatih Ömer İlday and Prof. Alphan Sennaroğlu for taking their time to read and evaluate my thesis and providing their invaluable feedback.

I thank Özgün Akyüz, Emre Ünal and Birsen Bilgili for making sure our group's operation is continuous. I thank Duygu Kazancı, Ayşegül Torun, Mete Duman, Murat Dere, Mustafa Doğan, Mustafa Güler, Dr. Gökçe Çelik, Övünç Karakurt, Murat Güre, Semih Bozkurt, Fatih Büker, Muhammed Emin Gürbay and rest of the UNAM crew for their underappreciated efforts to keep the facilities up and running. I thank the past and present members of our team, Dr. Kıvanç Güngör, Dr. Burak Güzeltürk, Dr. Yusuf Keleştemur, Dr. Negar Gheshlaghi, Dr. Savaş Delikanlı, Dr. Murat Olutaş, Dr. Talha Erdem, Dr. Zeliha Soran Erdem, Ulviyya Quliyeva, Dr. Manoj Sharma, Ashma Sharma (and dear Yuvraj), Furkan "Datome" Işık, Dr. Aydan Yeltik, Dr. Nina Sheremet, Dr. Volodymyr Sheremet, Farzan Shabani, İbrahim "Gaziantepspor" Tanrıöver, Mustafa "Too-Busy-To-Play-Portal-2-With-Me-But-Not-Too-Busy-To-Play-That-Silly-Mobile-Game-With-Others-All-The-Time" Sak, Hamza Humayun, Hamed Dehghanpour Baruj, Joudi Maskoun, Bilge Yağcı, Dr. Yemliha

Altıntaş, Selim “Too-Cool-To-Rent-A-Şahin-And-Drive-Around-In-Bilkent-Even-Though-He-Promised-To-Do-So-After-His-Defense” Bozdoğan, Nima Taghipour, Dr. Sayım Gökyar, Dr. Akbar Alipour, Aziz Taner Astarlıoğlu, Ramazan Özbek, Muhammad Ahmad, Sina Foroutan, Bülent “Fellow Spurs Fan” Kanmaz, Taylan Bozkaya and İklim Yurdakul for all the joyous moments we have had and their contribution to my work.

I thank the anonymous users of LaTeX forums for having the solution to almost every single problem I had while compiling my thesis. I owe them my sanity.

I thank Mr. Saygın Erdem, Mrs. Nedret Meral and Mr. Mustafa Meral for making my graduate school journey possible.

I thank my mother, Saadet Erdem, for her patience, love and continuous support for 30 years (and counting). She and my father are the ones that made me what I am, for which I will always be grateful.

I acknowledge TÜBİTAK for their financial support through BİDEB 2211 scholarship program.

Contents

1 Introduction **1**

1.1 Motivation 4

1.2 Outline of the Thesis 5

2 Scientific Background **6**

2.1 Semiconductor Nanocrystals 6

2.1.1 Colloidal Quantum Wells 12

2.2 Nanocrystal Self-Assembly 14

2.3 Förster Resonance Energy Transfer (FRET) 21

2.3.1 FRET Using Colloidal Nanocrystals 29

2.4 Optical Gain 31

2.4.1 Optical Gain of Nanocrystals 36

3 Self-Assembly of CQWs for Mono- and Multi-layered CQW Superstructures **41**

3.1 Orientation-Controlled Monolayers of Self-Assembled CQWs . . . 41

3.2 Multilayered Construction of Self-Assembled CQWs 50

3.3 Summary and Discussion 58

4 Orientation-Controlled FRET with Self-Assembled Monolayers of CQWs **61**

4.1 Experimental Observation of Orientation-Controlled FRET to CQWs 63

4.2 Theoretical Modeling of Orientation-Controlled FRET to CQWs . 70

4.3 Accounting for the Purcell Effect in FRET to CQWs 80

4.4 Summary 86

5 Optically Active Planar Waveguides of Multilayered, Self-Assembled CQW Constructs 88

5.1 Optical Gain in Thickness-Controlled CQW Self-Assemblies . . . 90

5.2 Tuning the Modal Confinement and Amplified Spontaneous Emission Wavelength 94

5.3 Summary and Discussion 100

6 Conclusion 102

6.1 Future Outlook 102

6.2 Contributions to Literature 104

6.2.1 Publications 104

6.2.2 Patents 106

List of Figures

2.1 Representative band alignments with respect to the Fermi level E_F and band filling at absolute zero temperature. For semiconductor and insulators, the highest occupied band (valence band) and the lowest unoccupied band (conduction band) are separated by an energy gap E_G, which is called the bandgap. 7

2.2 Representative E-k diagrams for (a) direct- and (b) indirect-bandgap semiconductors. 8

2.3 The process of a photon absorption and re-emission by a direct-bandgap semiconductor: I) An indicent photon with an energy larger than the bandgap might induce photoabsorption. II) As a result of the absorption, an electron (filled circle) is excited to the conduction band, leaving a hole (hollow circle) in the valence band. III) Electron and hole relax to the edges of the conduction and valence band, respectively. IV) In the case of a radiative recombination, a photon is released when electron loses its energy. 9

2.4 Semiconductor NCs have denser yet still discrete states similar to molecular states, whereas the states in bulk semiconductors form a continuum. 10

2.5 (a) Transmission electron micrograph of CdZnS/ZnS QDs synthesized and imaged by our group. (b) Schematic depiction of a quasi-spherical colloidal nanocrystal together with ligands on facets. Ligands on some facets are not drawn for clarity purposes. Adapted with permission from ref. [31]. Copyright 2008 American Chemical Society. 11

2.6 (a) Transmission electron micrographs of 4.5 monolayer thick CdSe CQWs taken by our group. Inset shows the schematic depiction of these CQWs having zinc blend crystal structure, where 5 layers of Cd atoms (grey) are alternating with 4 layers of Se atoms (orange). The atomically precise vertical thickness is 1.2 nm. (b) Absorbance (solid) and PL (dashed) spectra of 3.5 ML (top), 4.5 ML (middle) and 5.5 ML (bottom) CdSe CQWs. Adapted with permission from ref [11]. Copyright 2008 American Chemical Society 14

2.7 (a) Stearic acid molecule, which has a hydrophilic carboxyl group at one end (circled) of a hydrophobic alkyl group (b) Langmuir deposition of a stearic acid monolayer on a substrate. (c) Multilayered deposition of stearic acid with substrate immersion. . 16

2.8 (a) Scanning electron micrograph of self-assembled monodisperse QDs forming a 2D hexagonal lattice. (b) Self-assembly of vertically oriented NRs. Adapted with permission from Ref. [84]. Copyright 2010 American Chemical Society. (c) Colloidal QD superlattices with face-centered cubic (fcc) and hexagonal close packed (hcp) crystal structures in different regions. Adapted with permission from Ref. [82]. Copyright 2010 American Chemical Society. 18

2.9 Basic procedure of liquid-air interface self-assembly: The organic NC solvent is dropped onto a polar subphase. After the solvent is evaporated, NCs form a thin membrane on the liquid interface. The substrate is lifted up, during which a part of the NC film is transferred to it. 19

2.10 Electric field of a point dipole with dipole moment $\vec{\mu}_d$. Grey vectors indicate the direction of the electric field. Contours are drawn along points with a constant magnitude. 22

2.11 Plot of FRET efficiency as a function of donor-acceptor distance when the rate of FRET is proportional to $1/R^6$ (blue curve), $1/R^5$ (black curve) and $1/R^4$ (red curve). 26

2.12 Distance dependence of FRET for different acceptor dimensionalities 28

2.13 Band diagrams of a donor and acceptor NC (a) before and (b) after FRET. Asterisk indicates the particle in the excited state in both panels. 29
2.14 Fundamental processes related to the interaction of light and matter: Absorption (left), spontaneous emission (middle) and stimulated emission (right). 32
2.15 (a) Optical transitions on a (a) 2-level, (b) 3-level, and (c) 4-level system. Transitions related to the optical gain are marked red. Downward transitions between non-consecutive states are not shown in (b) and (c). 33
2.16 Schematic of optical amplification process. 36
2.17 Auger recombination in NCs, where energy of one exciton can be transferred to a third charge; in this case, the electron of the other exciton. Excited electron will be highly energetic and might be therefore trapped, creating a charged particle. 38

3.1 High-angle annular dark field scanning transmission electron microscopy (HAADF-STEM) image of 4.5 ML CdSe CQWs. Inset schematically shows the orientation of nonstacked (face-down) and stacked (edge-up) CQWs that co-exist in the shown image. Adapted with permission from Ref. [28]. Copyright 2019 American Chemical Society. 44
3.2 (a) Our home-built setup for the self-assembly of colloidal quantum wells and their deposition onto solid substrates. (b) Liquid-air interface self-assembly procedure: (I) Blank substrates are placed inside the subphase. (II) CQW solution is poured onto the subphase and is then allowed to dry. (III) The subphase is drained after the evaporation of the CQW solution. The resulting CQW orientation depends mainly on the subphase chosen. The CQW orientation in the monolayer is face-down for the acetonitrile (ACN) subphase and edge-up for the ethylene glycol (EG) subphase. Adapted with permission from Ref. [28]. Copyright 2019 American Chemical Society. 45

3.3 Scanning electron microscopy (SEM) images of (a, c) face-down and (b, d) edge-up CQWs deposited with our self-assembly technique. Images in (c) and (d) are taken with a lower magnification to observe the large-scale film deposition. Gaps and crack formation are visible in (c) and (d) (light grey areas), which are mostly formed during the transfer process. Adapted with permission from Ref. [28]. Copyright 2019 American Chemical Society. 46

3.4 Photographs of (a) nonstacked and (b) stacked CQW monolayers deposited onto 2-inch wafers under UV illumination. These photographs were taken from the top. (c) and (d) the same wafers with their photos taken from the side. (c, d) adapted with permission from Ref. [28]. Copyright 2019 American Chemical Society. 48

3.5 (a) Transmission electron micrograph of $CdSe/Cd_{0.25}Zn_{0.75}S$ CQWs used for their self-assembly. (b) TEM image of the same CQWs in vertical orientation. (c) Absorbance (dashed black line) and photoluminescence (solid red line) spectra of these CQWs. Adapted from Ref. [131] 52

3.6 (a) Schematic demonstration of our self-assembled CQW deposition. Blank or predeposited substrates are inserted into a subphase of diethylene glycol (DEG). The CQW solution is dropped onto the subphase and quickly spreads across the liquid-air interface. Dropped silicone oil compresses the CQW membrane. After complete evaporation of the hexane, DEG is drained out with the help of a peristaltic pump. As a result, all the substrates are deposited with one additional monolayer of CQWs. (b) Photograph of our home-built setup for the self-assembly. Inset: In-situ photograph of the CQW membrane (red) in the teflon dish illuminated with blue light. The CQW membrane is pushed to the left, towards over the substrates, by the silicone oil solution dropped from the right side of the teflon dish. (c) Scanning electron micrograph of the resulting CQW monolayer deposited. (d) Our self-assembly setup used for the large area deposition. (e, f) Photographs of a 4-inch wafer of fused silica deposited with one monolayer of CQWs, illuminated with UV light, from the top and from the side, respectively. Adapted from Ref. [131]. 53

3.7 Self-assembled deposition of CQWs (a, b) without and (c, d) with membrane compression using silicone oil. In panels a through d, dark areas are void while light areas are covered with CQWs. (e) 4-inch wafers deposited by using insufficient (left) and sufficient (right) amount of silicone oil solution. Adapted from Ref. [131]. . 55

3.8 (a) Cross-sectional TEM image of 11 CQW monolayers sequentially deposited onto silicon. All the CQW layers are distinctly visible, separated by their surface ligands. (b) Measurement of film thickness for the multilayered CQW constructs having different numbers of layers. The linear fit confirms 7.0 nm of thickness per deposited CQW layer. (b) Surface roughness measurements of multilayer CQW films on fused silica taken with atomic force microscopy imaging over 5 different regions having an area of 2×2 μm^2. Dashed line shows the roughness of the bare fused silica subtrate (∼0.2 nm). Adapted from Ref. [131]. 56

4.1 SEM images of CdZnS/ZnS QDs on a (a) face-down and (b) edge-up CQW monolayer. (c) Absorbance spectrum of the CQWs (green) and photoluminescence (PL) spectrum of the QDs (blue). Adapted with permission from Ref. [28]. Copyright 2019 American Chemical Society. 64

4.2 (a) Photograph of the time-resolved spectrometer. (b) Photoluminescence decay of the QDs in the absence of CQWs (blue), on top of the face-down CQWs (red) and on top of the edge-up CQWs (green). (c) Schematic demonstration of the enhancement of FRET from QDs to a CQW monolayer in the case of edge-up CQWs. b, c adapted with permission from Ref. [28]. Copyright 2019 American Chemical Society. 66

4.3 Overall structure of the FRET working model system between donor QDs and acceptor CQW monolayer for (a) face-down and (b) edge-up CQWs. PL decays of QDs over (c) face-down (nonstacked) and (d) edge-up (stacked) CQWs. The black curves are fits to multiexponential decays convolved with the instrument response function. (e) Average decay lifetimes of QDs and (f) extracted rates of FRET to the face-down (blue down triangles) and edge-up CQWs (orange up triangles). (g) FRET efficiencies as a function of the donor-acceptor distance along with their numerical fits to the FRET efficiency formula in the inset (Equation 4.4). The data captures the d^{-4} behaviour for both CQW orientations. The vertical dashed lines indicate the Förster distances for FRET to the face-down (blue) and edge-up (orange) CQW monolayers. Adapted with permission from Ref. [28]. Copyright 2019 American Chemical Society. 68

4.4 Average dipole orientation coefficient $\langle\kappa^2\rangle$ of a QD and a CQW when the CQWs are (a) face-down and (b) edge-up. Insets show that for the face-down CQW that is closest to the QD, (i.e. $\theta = 0$), $\langle\kappa^2\rangle$ becomes 1/3. For $\theta = 0$ in the edge-up array, $\langle\kappa^2\rangle$ is 5/6. Adapted with permission from Ref. [28]. Copyright 2019 American Chemical Society. 71

4.5 Variation of the average dipole-dipole orientation factor $\langle\kappa^2\rangle$ as a function of the coordinates of the dipole of a face-down CQW (a) calculated by the formula (Equation 4.18) and (b) estimated by the Monte-Carlo simulations. The QD and the CQWs are drawn out of scale for clarity purposes. (c), (d) Top-view of the surfaces in (a), (b), respectively. 75

4.6 Variation of the average dipole-dipole orientation factor $\langle\kappa^2\rangle$ as a function of the coordinates of the dipole of a edge-up CQW (a) calculated by the formula (Equation 4.25) and (b) estimated by the Monte-Carlo simulations. The QD and the CQWs are drawn out of scale for clarity purposes. (c), (d) Top-view of the surfaces in (a), (b), respectively. 77

4.7 Variation of the distance between a QD dipole and a delocalized CQW dipole for (a) face-down and (b) edge-up CQW orientation, depending on the position $\vec{r}'$ of the CQW dipole. (c) Experimental rates of FRET to the face-down CQW monolayer (blue down triangle) compared to those esimated by two different models based on Förster's theory: center-to-center distance approach (small black dots) and delocalized dipole approach (large blue dots). (d) Center-to-center distance approach (black dots) and delocalized dipole approach (large red dots) applied to the edge-up CQW monolayer case to estimate the FRET rates and compare them with the experimentally measured ones. Adapted with permission from Ref. [28]. Copyright 2019 American Chemical Society. 79

4.8 Schematic cross-section of the layered media below an isotropic QD dipole. For the only-donor system, there are no CQW or spacer layers. For the FRET system without a spacer, there is no Al_2O_3 layer on top. $\bar{k}$ is 0.065 for the face-down CQW monolayer and 0.080 for the edge-up one. 81

4.9 Purcell factor analysis on our FRET model system. (a) Calculated Purcell factors F as a function of the spacer thickness for all samples via Equation 4.27. Blue (orange) squares are Purcell factors of QDs over a monolayer of face-down (edge-up) CQWs. Black dashed line is the Purcell factor of the only-QD film. Estimated QD decay lifetimes by incorporating Purcell factor for (b) nonstacked and (c) stacked CQW films. (d) Calculation of FRET efficiency using the estimated lifetimes in (b) and (c). Solid lines show the fits using the FRET efficiency formula given in the inset. With the estimated QD lifetimes, the distance-dependence, as well as the Förster distance of FRET, is estimated and compared to the experimental lifetimes. 85

4.10 Purcell factor for QD-CQW films when the CQW layer is assumed to be lossless. 86

5.1 Photograph of the optical gain characterization setup. I: attenuator, II: barium boreate crystal, III: short-pass filter, IV: beam splitter, V: cylindrical lens, VI: tunable slit, VII: xyz stage, VIII: sample, IX: powermeter, X: optical fiber, and XI: optical spectrometer. The inset depicts the optical setup schematically. Blue arrows in the photo and the inset show the direction of propagation of the excitation pump. 91

5.2 (a) Emission spectra of the CQW films having a different number (n) of layers excited with a pulsed laser at 400 nm: left, $n = 6$, center, $n = 9$ and right, $n = 15$. Colorbar at the bottom is common for all three plots. (b) Integrated intensity as a function of the pump fluence for all the CQW films from $n = 6$ to $n = 15$. (c) Evolution of the optical gain threshold with the number of layers n as deduced from the data in panel b. (d) Shifting of the ASE peak with respect to the spontaneous emission for different n. Inset shows the difference between the ASE and spontaneous emission peaks. The color coding is identical in panels b-d. Reprinted from Ref. [131] 93

5.3 Asymmetric waveguide structure for a multilayered CQW construct of thickness t. 95

5.4 (a) Field intensity profile of the fundamental TE mode numerically calculated for the CQW slab with $n = 6$. (b) Optical confinement factor Γ calculated at 650 nm for varied numbers of CQW layers (and slab thickness). Dashed line indicates the critical thickness of 41.2 nm for the existence of propagating modes within the slab. (c) Left axis: Variation of the confinement factor Γ with wavelength for different numbers of layers. Right axis: Gain spectrum $\Gamma(\lambda)$ for our CQWs estimated using the measured ASE peaks at different film thicknesses, modeled as a Gaussian centered at 665 nm with a FWHM of 106.6 nm (blue) (d) ASE peaks calculated as the maximum of $\Gamma(\lambda) \times G(\lambda)$ for each n (red stars), together with the experimentally measured ASE peaks (blue squares). Adapted from Ref. [131]. 98

List of Tables

4.1 Multiexponential fitting parameters for PL decays of QDs over face-down CQWs. PL decay of only QDs are also added for reference. Reprinted with permission from Ref. [28]. Copyright 2019 American Chemical Society. 69

4.2 Multiexponential fitting parameters for PL decays of QDs over edge-up CQWs. PL decay of only QDs are also added for reference. Reprinted with permission from Ref. [28]. Copyright 2019 American Chemical Society. 69

5.1 Gaussian fitting parameters for the ASE spectra presented in Figure 5.2d. Peak and full-width-at-half maximum (FWHM) values for spontaneous emission (SE) and ASE features. Adapted from Ref. [131]. 94

Chapter 1

Introduction

After their introduction almost three decades ago, colloidally synthesized semiconductor nanocrystals (NCs) have revolutionized the field of nanophotonics, opening a new direction of colloidal optoelectronics, thanks to their remarkable electronic and optical properties, which can be tuned with the particle size [1, 2]. Over the years, advances in colloidal synthesis techniques enabled extensive studies on various shapes and compositions of NCs, which led to creation of highly emissive NCs that can cover the entire visible spectrum while maintaining their spectrally narrow emission. The current state-of-the-art methods enable synthesis of colloidal NCs that display high monodispersity as well as near-unity quantum efficiency. NCs having different compositions and shapes are shown to be suitable for applications such as lasers [3–5], LEDs [6–9] and displays [10].

One of the more recent classes of colloidal semiconductor NCs is colloidal quantum wells (CQWs), which are quasi-two dimensional NCs with atomically flat lateral surfaces [11, 12]. CQWs possess properties similar to those of epitaxially grown quantum wells owing to their similar shape, yet have the advantage of being created by the low-cost colloidal synthesis techniques. CQWs have been shown to have ultra-narrow emission linewidth [12, 13], giant oscillator strength [12] and enhanced optical absorption [14]. Furthermore, due to their shape, CQWs display optical anisotropy as the excitonic state of the CQWs

is oriented along the CQW plane. This causes their emission pattern to be anisotropic such that the propagation direction is mostly out-of-plane [15]. This indicates that the emission of the CQWs can be directed if their orientation can be controlled, e.g. in solid films. This can be helpful in applications such as lasers and LEDs, where limiting the light propagation only along certain directions can enhance the device efficiency [16]. However, with conventional techniques of film deposition such as drop-casting and spin-coating, orientation control of anisotropic NCs is often challenging, and it is quite possible to obtain mixed orientations, in which some CQW are horizontally oriented (nonstacked), while the others tend to form one-dimensional superstructures composed of face-to-face oriented (stacked) CQWs [17–19]. This hinders the utilization of the anisotropic properties of CQWs. To study and fully exploit their anisotropy, creating CQW films in which all the CQWs are in a single orientation (either fully-nonstacked or fully-stacked) is necessary.

As CQWs start to be incorporated into optoelectronic devices, their thin film deposition will be an important step in the fabrication process because these thin CQW films will also need to be more precisely deposited as the devices keep shrinking in size. It is often required to obtain NC films having a certain thickness and sufficient uniformity. For this, deposition techniques such as drop-casting and spin-coating are commonly employed. In drop-casting, one or few droplets of colloidal NC solution are dropped onto the substrate, which is then left for controlled drying. Once all the NC solution is dried, a thin film of NCs is formed on the substrate. However, drop-casted films often suffer from nonuniformity due to uneven thickness. Alternatively, spin-coating can be used to deposit the NCs much more uniformly. Herein, the NC solution is dropped onto a substrate that is being rapidly rotated, which helps their drops spread evenly throughout the substrate. Nevertheless, the control of film thickness with spin-coating is not precise as it depends on various independent factors such as NC concentration, amount of NC solution and rotation speed. Because of this, thickness control of NC films prepared by spin-coating might suffer from reproducibility. Also, neither drop-casting nor spin-coating allows for orientation control of the anisotropic particles in the deposited film. For better control in thickness, methods such as

Langmuir-Blodgett (LB) or layer-by-layer deposition, both of which are excellent tools for thickness-controlled deposition of thin films, were commonly employed for QDs [20–22] or nanorods (NRs) [23, 24]. Various liquid-air interface self-assembly deposition of binary QD superlattices [25] and NRs [26] have previously been reported. However, the studies that employ these techniques for deposition of Cd-based II-VI CQWs are quite limited [27]. For a better understanding of the optical properties of the CQWs and to facilitate their incorporation into device fabrication, it is of great importance to be able to create their thickness-controlled films.

Here, we address the aforementioned problems related to CQW deposition by proposing a novel technique of liquid-air interface self-assembly of CQWs enabling orientation control. With our technique, we are capable of depositing core CQWs as a close-packed orientation-controlled monolayer over tens of cm^2 large areas. This monolayer is composed of CQWs having a single orientation of fully nonstacked or fully stacked, depending on the choice of parameters during the deposition. Using these monolayers, we demonstrate that the rate of Förster resonance energy transfer (FRET) from QDs to the monolayer of CQWs can be tuned and controlled with CQW orientation. Our analytical model based on Förster theory reveals that the difference in FRET rate for both orientations is due to the changing dipole alignment factor between QDs and CQWs in two CQW orientations. With the help of our technique, we revealed and demonstrated the first account of orientation-controlled FRET with CQWs [28].

It is possible to modify our technique such that CQWs of core/shell structure can be deposited one monolayer at a time to single substrates. In this modified version, we are capable of depositing these CQWs onto various substrates with areas as large as 80 cm^2. By depositing the substrates as many times as desired, we can construct multilayered and close-packed CQW films having precise control in thickness while maintaining their excellent uniformity and strong emission. We use this technique to create CQW superstructures with any desired thickness in terms of number of layers, and test the resulting films for their optical gain performance. We find that these CQW multilayers can display amplified spontaneous emission (ASE) in their films as thin as 6 layers, which corresponds

to a physical thickness of 42 nm. This thickness is much smaller than the typical thicknesses of a few 100s of nm required for other NC films. Furthermore, we demonstrated that the threshold pumping intensity necessary for the observation of ASE gradually decreases with the number of CQW layers. Our calculations unveiled that the decreased ASE threshold with increasing film thickness is caused by the enhanced optical mode confinement in thicker CQW films. We therefore showed the first account of thickness-dependent optical gain with CQWs thanks to our technique, which makes it possible to precisely control the film thickness. Our results indicate that this self-assembly technique is an excellent tool to create large-area 3D superstructures out of CQWs, which can be extended to device fabrication.

1.1 Motivation

The purpose of this thesis is to shed light into the optical properties of CQWs by studying their thickness- and orientation-controlled films in various aspects. To this end, we use the novel techniques of self-assembly that we developed as a tool to prepare such films, and use optical spectroscopy to study their interactions with other NCs in their vicitinity, and to observe the optical amplification of the light propagating through their self-assembled waveguides. Our orientation-controlled deposition technique enables the use of CQW optical anisotropy to tune the strength of energy transfer by engineering the QD-CQW dipole-dipole interaction. Furthermore, thanks to our multilayered deposition technique, we observed optical gain in the form of ASE from a thin layer of CQWs, which can pave the way for devices that require ultra-thin gain media. These self-assembly tools, which are also applicable to depositing other types of colloidal semiconductor NCs, can be a benchmark building block for creating large-area two- or three-dimensional superstructures, to be used in device fabrication and as a means to study the direction-dependent optical properties.

1.2 Outline of the Thesis

We begin in the next chapter by introducing important scientific used in this thesis. This includes a brief review of colloidal NCs and their self-assembly, the concepts of FRET and optical gain, and their demonstrations with colloidal NCs.

In Chapter 3, we demonstrate and explain our techniques for orientation-controlled mono- and multi-layered CQW self-assembly. The techniques shown here are used in the following chapters for the preparation of CQW films.

In Chapter 4, we present our results in one of our previous publications [28] related to the orientation-controlled FRET from QDs to CQWs. Herein, we used our orientation-controlled self-assembly method to create large-area films of CQWs in a single desired orientation, and deposited QDs on top of them to study FRET from QDs to CQW monolayers.

In Chapter 5, we show mutlilayered CQW assemblies as thickness-controlled gain media. For this, we used our multilayered self-assembly technique to create thickness-controlled CQW superstructures. We studied the optical gain spectroscopy of the constructed CQW films having different thicknesses, and evaluated the resulting ASE behaviour by taking the film thickness into account.

We conclude this thesis in Chapter 6, where we sum up our presented results and discuss the future outlook for two- and three-dimensonal self-assembled CQW superstructures.

Chapter 2

Scientific Background

2.1 Semiconductor Nanocrystals

Semiconductor refers to the group of solid state materials that have electrical conductivity between those of metals and those of insulators. This electrical conductivity is determined by the position of the Fermi level with respect to the energy bands of the material. In metals, the Fermi level lies within an energy band, which causes this band to be partially occupied with electrons. This partial occupation allows electrons in this band to be highly mobile under external electric field, which leads to high conductivity. In insulators and semiconductors, however, the Fermi level is within a forbidden energy gap, where no electronic states are allowed (Figure 2.1). Therefore, at absolute zero temperature, all the energy bands below the Fermi level are fully occupied whereas the ones above the Fermi level are absolutely empty. The energy band closest to the Fermi level from below (above) is referred to as valence (conduction) band. Insulators and semiconductors are differentiated by the separation of their valence and conduction bands, the bandgap. Materials with a bandgap of 3-4 eV or more is regarded as insulators, whereas the ones having a smaller bandgap are called semiconductors [29, 30].

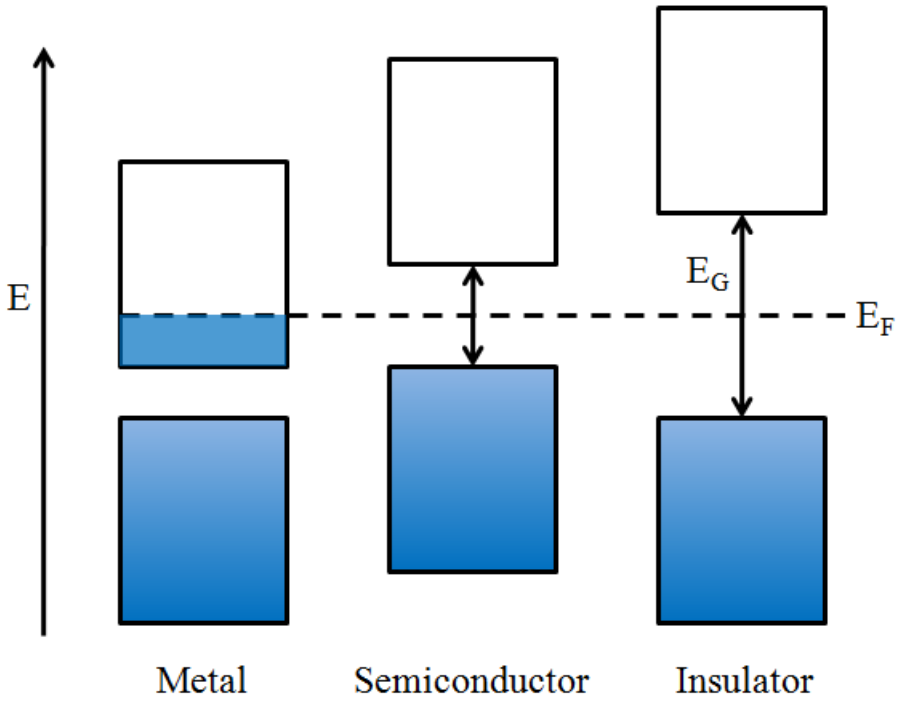

Figure 2.1: Representative band alignments with respect to the Fermi level E_F and band filling at absolute zero temperature. For semiconductor and insulators, the highest occupied band (valence band) and the lowest unoccupied band (conduction band) are separated by an energy gap E_G, which is called the bandgap.

A more detailed picture of the valence and conduction bands involve the electron wavenumber k along with its energy E. Accordingly, in semiconductor solids, each electron state is associated with a definitive pair of energy and momentum. Therefore, it is more appropriate to discuss the E-k diagrams for the valence and conduction bands. Figure 2.2 draws two representative E-k diagrams for semiconductors. Figure 2.2a is for direct-bandgap semiconductors, where the maximum of the valence band and the minimum of the conduction band correspond to the same wavenumber. In an indirect-bandgap semiconductor, these extrema are at different wavenumbers, corresponding to different momenta, as seen in Figure 2.2b. Examples of direct-bandgap semiconductors include CdSe, ZnS, InP, while Si and Ge are among indirect-bandgap semiconductors.

Direct bandgap semiconductors are particularly attractive for optoelectronics since it is possible to obtain photoluminescence by exciting their electrons with

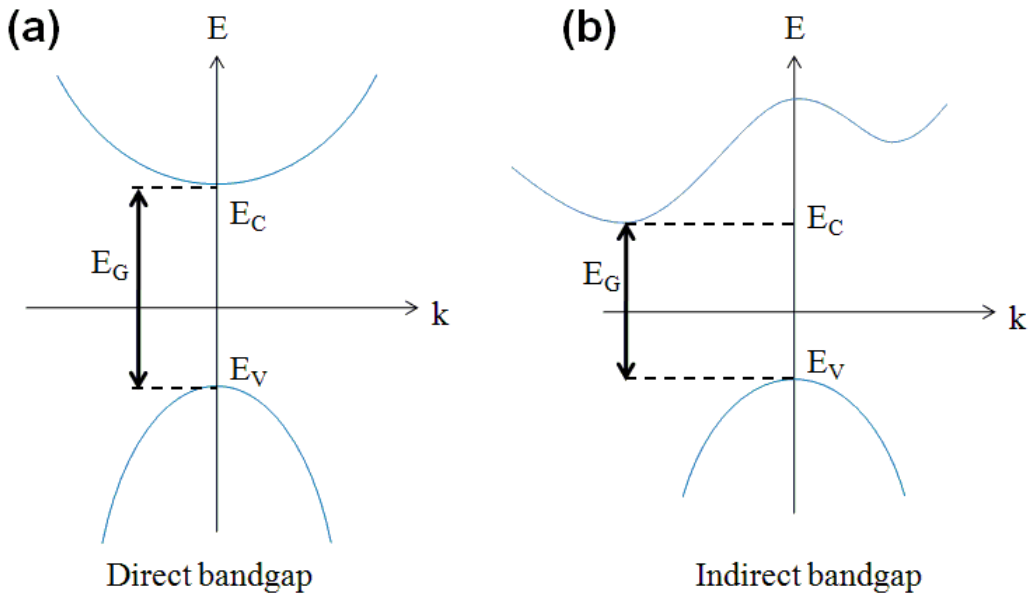

Figure 2.2: Representative E-k diagrams for (a) direct- and (b) indirect-bandgap semiconductors.

light (e.g., by visible light in the energy range of 1.8 - 3.1 eV) and obtain photoluminescence. In case that a photon with an energy greater than the bandgap is absorbed, one electron from the valence band is transferred to the conduction band, leaving a vacant state in the valance band. This electron vacancy can be treated as a positively charged particle with its own effective mass and mobility. This particle is called a *hole* and it contributes to the electrical conductivity in the semiconductors just like electrons. Furthermore, in the excited state, electron and its hole will attract each other through Coulombic interaction and form a hydrogen-like quasi-particle called an *exciton*. Excitons have their own effective mass and Bohr radius, which indicates the average distance between the pair of electron and hole in the excited state. After the excitation, the electron and hole will "cool down" to the bottom of the conduction band and top of the valence band, respectively. The electron will eventually "recombine" with the hole and in the process can release a photon, if through a radiative process, while going back to the valence band. This process is summarized in Figure 2.3.

Formation of the energy bands is the result of interatomic interactions between the many atoms of a solid. These atoms have their own discrete energy states,

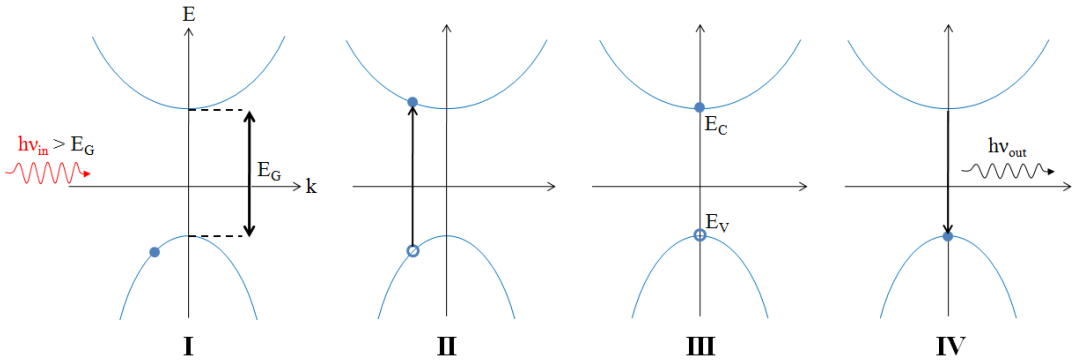

Figure 2.3: The process of a photon absorption and re-emission by a direct-bandgap semiconductor: I) An indicent photon with an energy larger than the bandgap might induce photoabsorption. II) As a result of the absorption, an electron (filled circle) is excited to the conduction band, leaving a hole (hollow circle) in the valence band. III) Electron and hole relax to the edges of the conduction and valence band, respectively. IV) In the case of a radiative recombination, a photon is released when electron loses its energy.

which are identical in all individual atoms when they are isolated. When these atoms are in proximity of each other, however, these energy levels split and form a continuum of energy states, which are the energy bands. Formation of these energy bands is due to the number of atoms in the bulk material being huge, which causes the final electronic states to become very closely spaced. When the number of atoms are limited, however, these states remain discrete. In nanocrystals (NCs), for instance, the number of atoms is typically between 100 and 10^5 [31], which results in discretization of the energy bands (Figure 2.4). This discretization has drastic effects on the properties of the material such as relaxation of the momentum conversation and the modification in the dynamics of intraband charge relaxation [32]. Secondly, the band gap will change with the number of available states, i.e. size of the nanoparticle. Therefore, both electronic and optical properties of the semiconductors are significantly altered by the particle size in the nanoscale. Since the states remain discrete, the NCs are occasionally referred to as "artificial atoms" as well.

The size-dependent changes in the properties of the semiconductors can also be understood through the "quantum confinement" effect. Similar to the particle-in-a-box problem, where narrowing down the box leads to more separate states

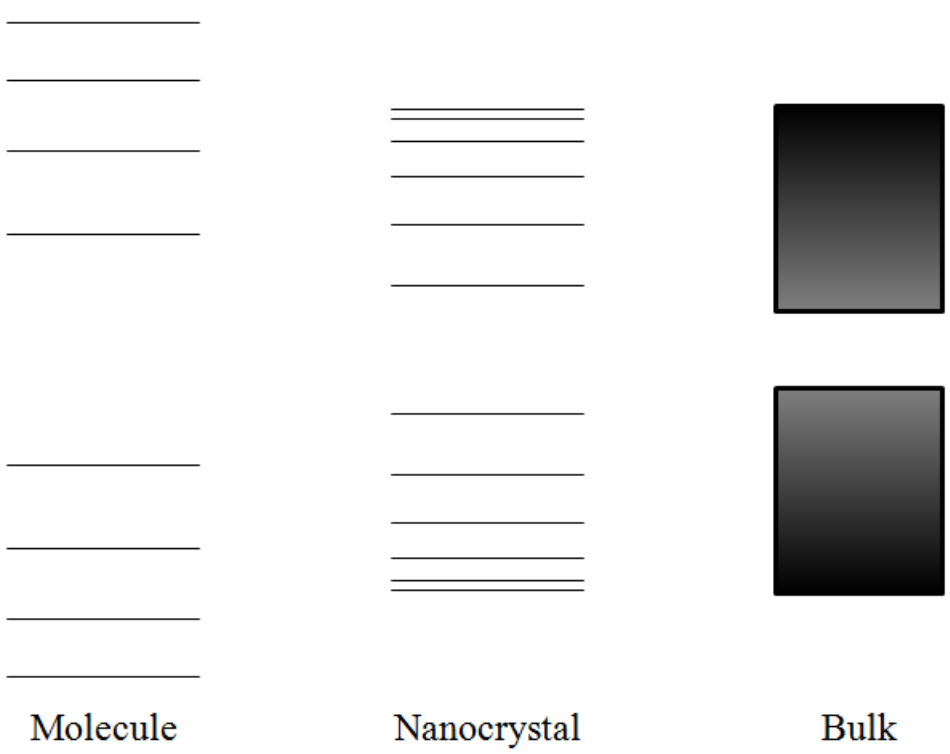

Figure 2.4: Semiconductor NCs have denser yet still discrete states similar to molecular states, whereas the states in bulk semiconductors form a continuum.

and higher energy levels, the energy of an exciton also increases when it is confined within a particle. The increase of the confinement energy of an exciton has been theoretically predicted for quantum wells [33] as well as spherical NCs [34]. Generally, this enhancement in the energy becomes noticeable when the particle size is comparable to or smaller than the exciton Bohr radius. The predicted quantum size effect was observed in the first examples of semiconductor nanocrystallites in 1980s, which were grown as embedded in glass matrices [35,36].

The studies on NCs took a drastic leap when Murray *et al* reported a generic, low-cost, nucleation-based colloidal synthesis technique for spherical NCs of CdSe, CdS and CdTe. Therein, they showed that the creation of highly monodisperse spherical NCs is possible through their synthesis route, with average sizes of the NCs in the ensemble ranging from 2 to 11 nm with a size dispersity of around 5%. They also demonstrated the tunability of absorbance spectra of these particles with their size [1]. An exemplary TEM image of an ensemble of CdZnS/ZnS

core/shell QDs (synthesized by Demir Group) is shown in Figure 2.5a. The crystallographic planes of the QDs are visible in the hi-resolution TEM image. Such NCs are commonly dispersed in organic, nonpolar solvents such as hexane, toluene and chloroform. The solubility of the NCs in such solvents are provided by their surface passivation with organic ligands such as oleic acid and oleylamine. These ligands are bound to the surfaces of the NCs at their functional group as seen in Figure 2.5b. Using different colloidal synthesis routes and surface ligands, it is also possible to disperse the NCs in polar solvents such as water [37]. Alternatively, ligand exchange procedures may be applied to replace the initial ligands with different ones [38]. Ligand exchange is commonly practiced to render the NCs soluble in certain polar solvents.

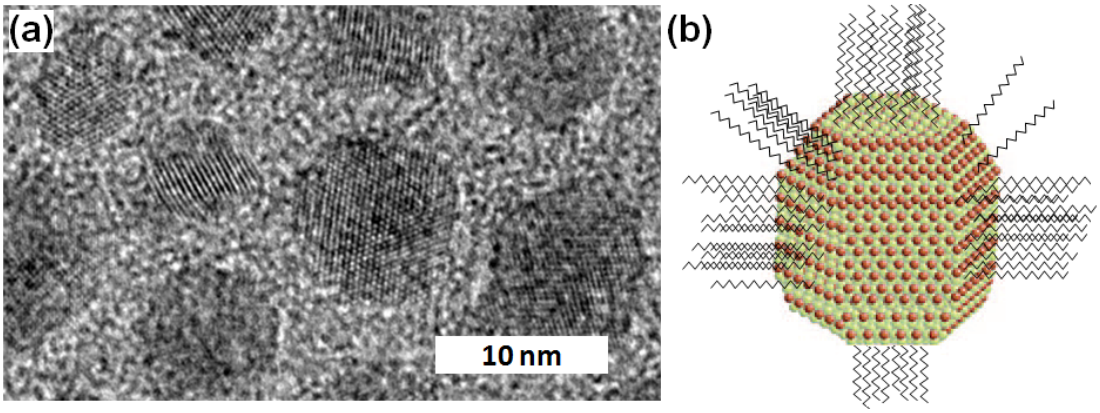

Figure 2.5: (a) Transmission electron micrograph of CdZnS/ZnS QDs synthesized and imaged by our group. (b) Schematic depiction of a quasi-spherical colloidal nanocrystal together with ligands on facets. Ligands on some facets are not drawn for clarity purposes. Adapted with permission from ref. [31]. Copyright 2008 American Chemical Society.

Surface passivation with ligands not only provides solubility, but also fills in the dangling bonds on the facets of these NCs. These bonds are associated with unsaturated atoms on the surface of the NC, which are highly energetic and therefore likely to cause trapping of electrons and holes. Such trapping mechanisms would reduce the photoluminescence efficiency of the NCs and is usually undesired for optoelectronic applications.

Another approach for the surface passivation is to deposit a lattice-compatible semiconductor material to the NC surface. The additional deposition can also be

carried out colloidally, which often results in increased stabilization and quantum efficiency of the materials. In the case of QDs, these hetero-NCs are known as core/shell QDs. Shell deposition leads to modification of the bandgap, as well as absorption and PL spectra as the extent of quantum confinement changes. The relative alignments of the valence and conduction band edges of the core and shell materials can also be used to confine the electron and hole to the different regions in the NC, thereby modifying and controlling the electron-hole and multiexcitonic interactions [39].

Depending on their electrical and optical properties and material composition, semiconductor NCs of different shapes and compositions are commonly being employed in applications including solar cells [40–42], LEDs [7, 8, 43], lasers [3, 44, 45], and displays [10]. The suitability of NCs for such a wide variety of applications stems from the many degrees of freedom, with which the excitonic properties can be controlled, including NC size, composition and heterostructuring.

To date, colloidal NCs with various dimensionalities have been synthesized and widely studied in terms of their optoelectronic properties. Some of the more common shapes, other than the spherical QDs, include nanocubes [46], tetrapods [47, 48] one-dimensional nanorods [49, 50], and quasi two-dimensional (2D) nanoplatelets [11,12,51,52], each with their own heterostructures. Quasi-2D nanoplatelets, also commonly referred to as colloidal quantum wells (CQWs), is the latest class of II-VI NCs. As they are relevant to and have been extensively studied throughout the rest of this thesis, we will give a brief review specifically on them.

2.1.1 Colloidal Quantum Wells

CQWs have quasi 2D shape with lateral sizes ranging from several to tens of nm, while their thickness is only a few nm. Since their lateral dimensions are generally larger than the exciton Bohr radius, the quantum confinement is effective only along vertical direction. The most striking property of the CQWs is

their atomically flat lateral surfaces, because of which they are sometimes referred to as "magic-sized" nanoplatelets. This atomic precision in thickness greatly reduces inhomogeneous broadening in the emission related to size dispersion. CQWs can therefore have emission linewidths as small as several nm's [12] at room temperature, which was not possible to observe with QDs even for their highly monodisperse ensembles.

The first report of the colloidally synthesized CdSe quantum wells came in 2008, where Ithurria *et al.* demonstrated zinc-blende CdSe CQWs of different thicknesses. The initial thicknesses they studied included 3.5, 4.5 and 5.5 lattice units (i.e. monolayers) formed by alternating Cd and Se atomic planes, starting and terminating planes being (100) Cd [11]. The TEM image for 4.5 monolayer (ML) CQWs (synthesized by Demir Group) as well as their schematic depiction is displayed in Figure 2.6a. In Figure 2.6b, the absorbance and PL spectra of the 3.5, 4.5 and 5.5 ML CQWs are shown. The electron-heavy hole peak is at around 460 nm for 3.5 ML CQWs and at around 550 nm for 5.5 CQWs, due to different extents of quantum confinement in different CQW thicknesses. The full-width-at-half-maximum (FWHM) of the emission is as low as 35 meV at room temperature [12], and down to 0.4 meV for a single particle at cryogenic temperatures [13]. Additionally, they display very small Stokes shift (2-3 nm) in their core structures, in comparison to QDs, where the Stokes shift is on the order of 10 nm.

It should be noted that, as opposed to spherical QDs, where continuous spectral tuning is possible by merely adjusting the QD radius, here the spectral peaks are discretized in that adding one additional monolayer induces a red shift on the bandgap on the order of 100 meV. Therefore, size tunability of CQWs suffers from the 1D quantum confinement. However, additional color tuning is possible through different means including using alloyed compositions in core CQWs [8, 53] and in the shell material [54–56] for CQW heterostructures.

Cd-based CQWs have already found use in applications including luminescence solar concentrators [57], LEDs [8, 9] and lasing [5, 17, 58]. Properties of CQWs such as step-like absorption profile, large absorption cross-section and spectrally

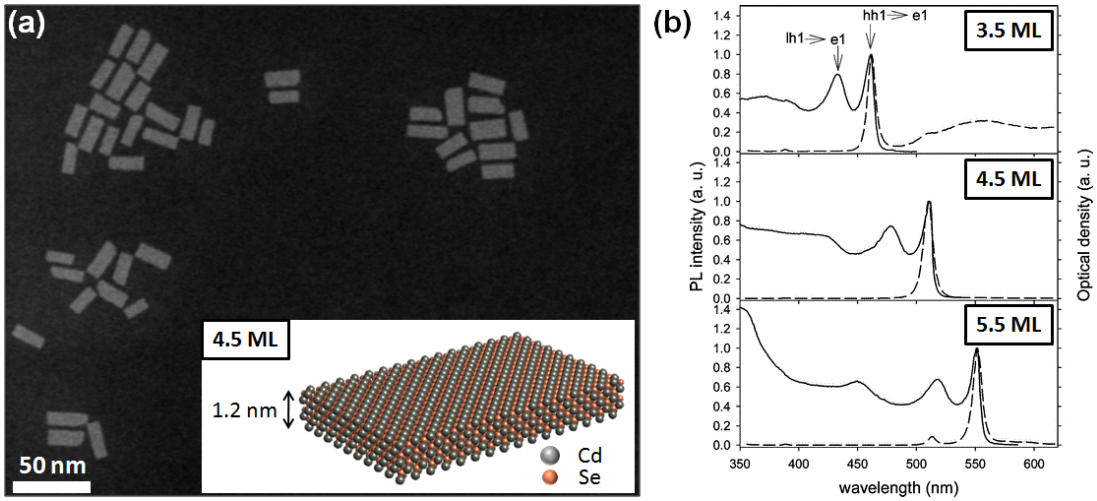

Figure 2.6: (a) Transmission electron micrographs of 4.5 monolayer thick CdSe CQWs taken by our group. Inset shows the schematic depiction of these CQWs having zinc blend crystal structure, where 5 layers of Cd atoms (grey) are alternating with 4 layers of Se atoms (orange). The atomically precise vertical thickness is 1.2 nm. (b) Absorbance (solid) and PL (dashed) spectra of 3.5 ML (top), 4.5 ML (middle) and 5.5 ML (bottom) CdSe CQWs. Adapted with permission from ref [11]. Copyright 2008 American Chemical Society

narrow emission render them favorable for such applications. Another remarkable property of the CQWs is their intrinsic anistropy stemming from their shape and the resulting 1D confinement of their excitonic state. This anisotropy has been determined by the out-of-plane emission pattern of the core CQWs [15]. CQWs can therefore be convenient for applications requiring directional emission [16]. To make use of this directional emission, however, one should make sure that the CQWs in a solid ensemble should have identically horizontal orientation so that they all emit in the same direction. One means to control the in-film orientation of the CQWs is to create their self-assembled films.

2.2 Nanocrystal Self-Assembly

Self-assembly, in general, refers to the spontaneous organization of individual components into ordered structures [59]. These individual components may be

atoms, molecules or nanoparticles. At the beginning of a self-assembly process, the particles are collectively in a mobile state, where they can move freely or under certain constraints, until the system "cools off" to an entropically favorable state where the particles come together in a sort of ordered structure. The properties of this structure is determined by the interactions of particles with each other and the environment as well as the ambient conditions under which the process takes place.

The term "self-assembly" is so broad that it extends over various scientific disciplines, each of which have their own interpretation of it. Therefore, the classes of assembled particles as well as the underlying mechanisms that govern the self-assembly kinetics are quite diverse. Among the building blocks that can be "self-assembled" are peptides [60, 61], hydrocarbon chains, DNA [62, 63], organic dyes [64, 65] and inorganic nanoparticles. Nevertheless, most phenomena regarded as self-assembly require a surface, onto which the individual particles attach themselves and form an ordered structure. We will be particularly focusing on the case where this surface is a flat liquid interface, and the particles to be deposited are colloidal inorganic NCs capped with hydrocarbon chains.

Although the tendency of tiny particles into forming superstructures had been known for many centuries, the first systematic attempts to describe and reproducably create self-organizing particles came in the late 19^{th} century. These attempts had commonly focused on assembling fatty acid molecules on water surfaces. One important step in understanding how the molecules assemble on liquid and solid surfaces was taken with Irving Langmuir's 1915 report on liquid adsorption. Through this paper he was able to explain how aliphatic molecules with hydrophilic end groups are oriented on water surfaces [66]. Later, making use of earlier ideas of Lord Rayleigh, who proposed that non-polar oil molecules spread over water surface as a single layer, and those of Agnes Pockels, who had constructed a rectangular trough to move the oil layer across the water surface, he came up with "Langmuir trough", with which he demonstrated deposition of fatty acid monolayers on solid substrates [67, 68]. In the basic procedure, the blank substrate is placed vertically, hanging on a string or rod, into water in the trough. After the oil is poured and spread and its solvent (if any) is evaporated,

the molecules on the water surface are compressed with the help of barriers until they form a close-packed monolayer. Then, the substrate is slowly rinsed while the barriers continue compressing the monolayer to maintain the surface pressure. As the substrate is being rinsed out of water, the molecules on the liquid surface are deposited onto the substrate. This process is demonstrated schematically in Figure 2.7b and 2.7c for an exemplary hydrocarbon molecule, stearic acid, which is formed by a saturated alkyl chain with a functional carboxyl group at one end (Figure 2.7a). The functional group is hydrophilic, whereas the alkyl chain is highly hydrophobic. As a result, in the compressed monolayer, the functional group of each molecule resides just below water surface and the radical group stands upright. This results in a "head-first" deposition of the monolayer onto the substrate.

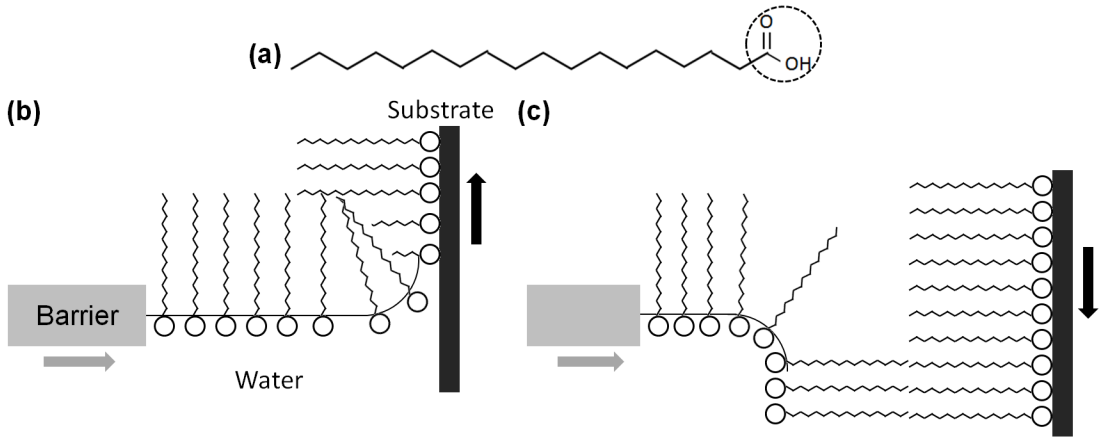

Figure 2.7: (a) Stearic acid molecule, which has a hydrophilic carboxyl group at one end (circled) of a hydrophobic alkyl group (b) Langmuir deposition of a stearic acid monolayer on a substrate. (c) Multilayered deposition of stearic acid with substrate immersion.

Langmuir had been working closely with Katharine Blodgett in carrying out these experiments, who in the following years generalized this technique for deposition of multiple layers of fatty acid molecules [69, 70]. Specifically, she demonstrated that these molecules could be deposited at each successive dipping and rinsing steps of the substrate (Figure 2.7c). Therefore, it is possible to create depositions having molecular level control and monolayer level precision over thickness. Deposition conditions can also be modified to dictate the out-of-plane orientation of the deposited molecules such that functional groups in a

monolayer can face away from or towards the substrate [71]. This multilayer deposition technique, now commonly referred to as Langmuir-Blodgett (LB) method, allowed for the deposition of multilayered molecules over the decades, which enabled detailed physical, chemical and optical investigations on the deposited molecules [72–75].

Colloidal NCs also benefited from the LB method, both for their thin film deposition and post-synthesis chemical and physical treatment [23,76]. Especially the NCs capped with hydrocarbon chains as ligands are quite relevant since the LB technique is directly applicable to them in most cases. However, methodologies for NC self-assembly extend beyond the LB technique. Common approaches include drying-mediated self-assembly, in which the NC solvent evaporation is controlled [77,78], solvent destabilization, for which an anti-solvent is added to create in-solution NC superstructures [79–81], doctor blade casting, where NC dispersion is distributed evenly across the substrate with the help of a "doctor blade" [82], and self-assembly assisted by liquid interfaces, where the NC solution is dropped onto an immiscible liquid to create a NC membrane on the liquid interface prior to deposition [25, 26, 83]. All these techniques have been proved to be capable of creating nicely ordered NC superlattices for highly monodisperse NC ensembles. Some examples for NC superlattices are shown in Figure 2.8. SEM image of a 2D QD film with hexagonal packing is displayed in Figure 2.8a. In Figure 2.8b are shown vertically oriented colloidal NRs [84]. NCs can also be ordered into long-range 3D superlattices having their own crystal structures [82, 85]. For instance, the TEM image of Figure 2.8c shows different regions of the TEM grid having different crystal structures, namely, face-centered cubic and hexagonal close packed. With QDs of two different sizes, it is even possible to create binary NC superlattices with long-range crystalline order and tight packing [25, 86, 87].

These earlier reports on QD self-assembly show that the QDs do live up to their nicknames of "artificial atoms". Not only do they have discrete energy states like atoms, but they are also capable of forming crystal structures idential to those of atomic and molecular crystals. Therefore, NC self-assembly has paved the way for exploration of light-matter interactions as well as crystal formation

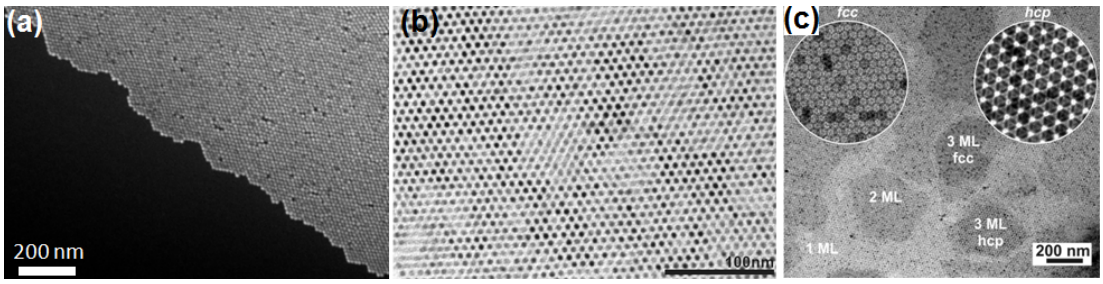

Figure 2.8: (a) Scanning electron micrograph of self-assembled monodisperse QDs forming a 2D hexagonal lattice. (b) Self-assembly of vertically oriented NRs. Adapted with permission from Ref. [84]. Copyright 2010 American Chemical Society. (c) Colloidal QD superlattices with face-centered cubic (fcc) and hexagonal close packed (hcp) crystal structures in different regions. Adapted with permission from Ref. [82]. Copyright 2010 American Chemical Society.

and structures on a whole new domain of giant atoms.

Liquid interface self-assembly, which is one of the NC self-assembly techniques briefly mentioned above, are among the more recent methods of NC self-organized film deposition. This technique is fundamentally similar to the LB technique as both of them rely on the concept of liquid interface as a host to the nanoparticles prior to the transfer to substrate. In the basic procedure, which is schematically demonstrated in Figure 2.9, NCs dispersed in an organic solvent are dropped onto a polar liquid denser than the NC solvent (e.g. water, diethylene glycol). Since these polar liquids do not dissolve the organic-capped NCs or their solvents, the NC solvent spreads across the surface of the polar liquid. After controlled evaporation of the solvent, the NCs are left as a thin membrane on the liquid interface. This NC membrane can then be transferred to solid substrates.

In one of the earliest demonstrations of this technique, Dong *et al.* used diethylene glycol (DEG) as the subphase to create binary NC superlattices of Fe_3O_4 and FePt NCs [25]. Min *et al.* used a variation of this technique, in which they placed the substrate before spreading the gold nanoparticles, and lifted the substrate in the end slowly with a stepper motor [88]. They used a toluene-acetonitrile mixture as the subphase, and tested the monolayer formation depending on different ratios of acetonitrile (ACN) and toluene. Furthermore, they used silicone oil to compress the gold nanoparticle monolayer, thereby to

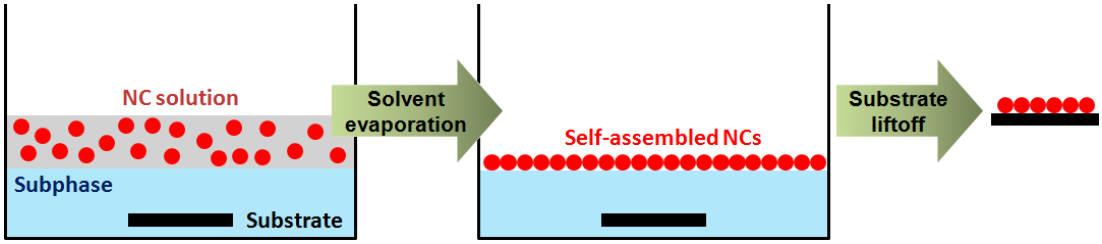

Figure 2.9: Basic procedure of liquid-air interface self-assembly: The organic NC solvent is dropped onto a polar subphase. After the solvent is evaporated, NCs form a thin membrane on the liquid interface. The substrate is lifted up, during which a part of the NC film is transferred to it.

obtain a close-packed film [88]. Liquid interface self-assembly is also commonly employed on NC annealing, where the NCs are chemically treated and fused together from their compatible facets to create ordered 2D NC arrays [89–91]. Therefore, liquid interface self-assembly not only helps creating NC superlattices, but also enables further processing of the NCs prior to deposition.

Liquid interface self-assembly gains additional dimension in the case of anisotropic NCs such as NRs and CQWs as it has recently been shown that the in-film orientation of such anisotropic NCs can be controlled via this technique. For instance, Paik *et al.* studied the orientation of self-assembled GdF_3 platelets with four different glycol-type subphases, namely mono- to tetraethylene glycol [83]. They observed that the most polar of the subphases studied, i.e. ethylene glycol (EG), leads to vertical ("lamellar") orientation of the platelets. As less and less polar subphases are used, on the other hand, the platelets start forming "columnar" (parallel to the substrate) assemblies in film. Diethylene glycol (DEG), for instance, causes mixed orientation whereas triethylene glycol and tetraethylene glycol lead to formation of fully columnar nanoplate assemblies [83].

A similar approach has been used for the self-assembly of various mono- and multi-layered NR superlattices by Diroll *et al.*, where the authors were able to tune the NR alignment and orientation by changing the subphase [26]. They studied several polar subphases including water, dimethyl sulfoxide, dimethyl formamide, EG and ACN to understand how each affects the NR orientation. They were able to create horizontal, orthogonal and smectic NR superlattices

by simply changing the subphase. They attributed the resulting change in the NR orientation to the different polarities, viscosities and surface tensions of the subphases used [26].

More recently, there have been multiple reports on the orientation control of Cd-based CQW assemblies. Gao *et al.* used a mixture of DEG and oleic acid as subphase to control the CQW orientation [15]. They concluded that the surface energy, thereby the resulting CQW orientation, can be controlled by using different oleic acid concentrations in DEG. Carrying out k-space spectroscopy measurements on the assemblies of "face-down" (horizontally oriented) and "edge-up" (vertically oriented) CQWs, this study demonstrated for the first time the out-of-plane emission from core CQWs, which is caused by the in-plane orientation of the excitonic dipole [15].

In this thesis work, we demonstrated that the orientation of CQWs can be controlled over cm^2-large areas by changing the subphase used [28]. Herein, we showed that ACN leads to "nonstacked" (horizontal) CQW assemblies, whereas EG leads to "stacked" (vertically oriented) chains of CQWs. These films, which we were able to deposit as a complete, single, close-packed monolayer, were utilized to control the rate of nonradiative energy transfer between donor QDs and oriented acceptor CQW monolayers. The results of this study will be presented in detail in Chapters 3 and 4.

A more recent report by Momper *et al.* shows that not only the subphase but also the evaporation speed of the NC solvent has a strong effect on the CQW orientation [92]. In their study, the authors showed that, using a single subphase, i.e., ACN, it is still possible to obtain both face-down and edge-up assemblies of CQWs by controlling the evaporation rate of the NC solvent. Accordingly, fast evaporation favors the face-down CQW assembly, whereas slow evaporation enforces edge-up assembly.

The studies above on anisotropic NCs clarify that there are a number of factors that affect their orientation during their self-assembly, including the choice of subphase, the evaporation rate, the type and density of the ligands that

passivate these NCs, and even the NC solvent. Fully understanding the effect of these factors, and how they alter the interparticle interactions is necessary to achieve full control over the resulting NC orientation, and is still under further investigation. Such an additional degree of freedom coming from the NC orientation makes liquid interface self-assembly more attractive for the case of anisotropic NCs such as CQWs.

Our efforts on orientation controlled mono- and multi-layered CQW assemblies will be discussed in detail in Chapter 3.

2.3 Förster Resonance Energy Transfer (FRET)

Förster (or fluorescence) resonance energy transfer (FRET) is the phenomenon of nonradiative energy migration from an excited fluorophore (donor) to another one (acceptor) nearby through dipole-dipole coupling. It is named after Theodor Förster, who is the first to propose an accurate theoretical description of the phenomenon [93]. The "resonance" part comes from the requirement of the states to take part in FRET being resonant. Since FRET occurs without the emission of a photon, the phenomenon is occasionally referred to as *nonradiative energy transfer* as well.

FRET is a dynamic process caused by the electric field induced by the excited donor on the acceptor site and the resulting interaction. It is best understood by considering the donor and acceptor as dipoles. The derivation of the rate of FRET is relatively straightforward when both the donor and acceptor are assumed to be point dipoles, which is an accurate approximation when their separation distance R is much larger than the physical dipole length. If the donor is modeled as an oscillating dipole with a frequency ω and a dipole moment $\vec{\mu}_d$, the electric field it generates is given by

$$\vec{E} = \frac{\mu_d}{\epsilon}\left(\left(\frac{1}{R^3} - \frac{ik}{R^2} - \frac{k^2}{R}\right)\sin\theta\hat{a}_\theta + 2\left(\frac{1}{R^3} - \frac{ik}{R^2}\right)\cos\theta\hat{a}_R\right)e^{i\omega\left(t-\frac{nR}{c}\right)} \quad (2.1)$$

Here, ϵ and n are the dielectric constant and refractive index of the medium,

respectively, θ is the angle between the dipole axis and $\vec{R}$, and $k = \omega/c$ is the wavenumber. The 1/R term, which dominates in the far field, is related to the radiation of energy. On the other hand, the $1/\mathrm{R}^3$ term, which dominates in the near field ($R \ll \lambda$), does not contribute to the radiation, and is the one responsible with the near-field dipole-dipole interactions. In the near field, the electric field converges to

$$\vec{E} = \frac{\mu_d}{\epsilon}\frac{1}{R^3}(\sin\theta\hat{a}_\theta + 2\cos\theta\hat{a}_R)e^{i\omega\left(t-\frac{nR}{c}\right)} \tag{2.2}$$

The near-field pattern of a point-dipole is drawn in Figure 2.10. It can be seen from Equation 2.2 that the near-field term has the same form as the static dipole field; consequently, the near field pattern of an oscillating dipole is the same as that of a static dipole.

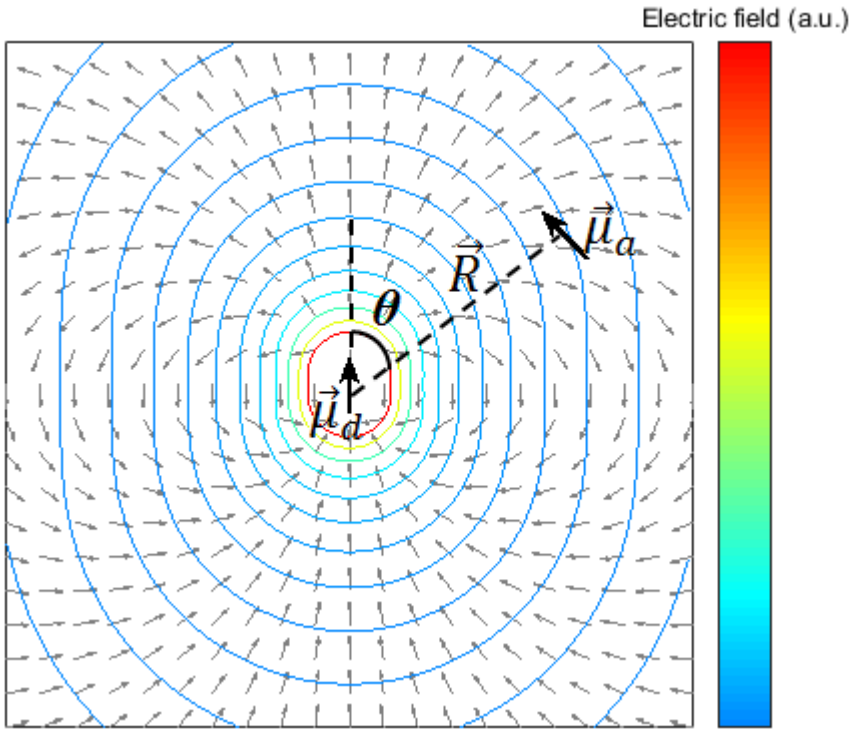

Figure 2.10: Electric field of a point dipole with dipole moment $\vec{\mu}_d$. Grey vectors indicate the direction of the electric field. Contours are drawn along points with a constant magnitude.

In Förster's semiclassical approach [93], the donor's electric field acting on the acceptor with a dipole moment $\vec{\mu}_a$ is taken as the transition matrix element between the initial (excited state donor and ground state acceptor) and final

states (ground state donor and excited state acceptor):

$$< f|H'|i >= \vec{E}\vec{\mu}_a = \frac{1}{\epsilon}\frac{\mu_d\mu_a}{R^3}\kappa \tag{2.3}$$

where

$$\kappa = \cos(\alpha_{da}) - 3\cos(\alpha_{dr})\cos(\alpha_{ar}) \tag{2.4}$$

is a factor accounting for the alignment of the dipoles. α_{da} is the angle between the donor and acceptor dipoles, α_{dr} is the angle between the distance vector $\vec{R}$ and the donor dipole (identical to θ in Figure 2.10), and α_{ar} is the angle between $\vec{R}$ and the acceptor dipole. Using Fermi's Golden Rule with resonant states,

$$\Gamma_i = \frac{2\pi}{\hbar}| < f|H'|i > |^2 = \frac{2\pi}{\hbar\epsilon^2}\frac{\mu_d^2\mu_a^2}{R^6}\kappa^2 \tag{2.5}$$

the rate of energy transfer is found to be proportional to $1/R^6$ as well as to κ^2, which is known as the dipole orientation factor. It should be noted that this factor might as well be zero depending on the relative orientations of the dipoles with respect to each other. In that case, FRET will not take place as the interaction energy will be zero. In general, κ^2 can take values between 0 and 4. Specifically, when the dipoles are perpendicularly oriented with respect to one another, κ^2 becomes zero. In the case of collinear orientation, κ^2 takes its maximum value, 4. However, in general, both fluorophores freely rotate in-solution, therefore κ^2 is not fixed. In case that these rotations are much faster than the energy transfer, κ^2 is averaged over all possible orientations. The orientation of a dipole $\vec{\mu}$ is determined by the polar and azimuthal angles θ and ϕ, respectively. The unit vector representing the donor (acceptor) dipole is then given by

$$\hat{\mu}_{d(a)} = \sin(\theta_{d(a)})\cos(\phi_{d(a)})\hat{a}_x + \sin(\theta_{d(a)})\sin(\phi_{d(a)})\hat{a}_y + \cos(\theta_{d(a)})\hat{a}_z \tag{2.6}$$

In the case of random orientation, the angular distribution of these angles is

$$f(\theta_{d(a)}, \phi_{d(a)}) = \frac{1}{4\pi}\sin(\theta_{d(a)}) \tag{2.7}$$

with $0 \leqslant \theta_{d(a)} < \pi$ and $0 \leqslant \phi_{d(a)} < 2\pi$. Choosing the coordinate system such

that the distance vector $\vec{R}$ is aligned with the z-axis, we obtain

$$\begin{aligned}\cos(\alpha_{da}) = \hat{\mu}_d \cdot \hat{\mu}_d &= \sin(\theta_d)\cos(\phi_d)\sin(\theta_a)\cos(\phi_a) + \sin(\theta_d)\sin(\phi_d)\sin(\theta_a)\sin(\phi_a) \\ &\quad + \cos(\theta_d)\cos(\theta_a) \\ \cos(\alpha_{dr}) = \hat{\mu}_d \cdot \hat{z} &= \cos(\theta_d) \\ \cos(\alpha_{ar}) = \hat{\mu}_a \cdot \hat{z} &= \cos(\theta_a)\end{aligned} \tag{2.8}$$

Inserting these expressions into Equation 2.4, and averaging κ^2 over all independent angles, the average dipole alignment factor can be calculated as

$$\langle\kappa^2\rangle = \int\limits_{\theta_d,\phi_d}\int\limits_{\theta_a,\phi_a} \kappa^2 f(\theta_d,\phi_d) f(\theta_a,\phi_a) d\theta_a d\phi_a d\theta_d d\phi_d = 2/3 \tag{2.9}$$

Förster set $\langle\kappa^2\rangle$ to 2/3 in his original derivation [93] as this is the case for the FRET within practically all non-viscous solvents. In more general formula of the energy transfer rate, however, this coefficient can be kept as it is.

The final formula for the rate of energy transfer is given by [94]

$$k_T = \frac{\langle\kappa^2\rangle}{R^6\tau_D}\frac{9\ln 10}{128\pi^5 N_A n^4} J \tag{2.10}$$

where τ_D is the radiative lifetime of the donor in the absence of the acceptor, N_A is the Avogadro's number, and J is the spectral overlap integral between the photoluminescence spectrum of the donor and the absorbance spectrum of the acceptor:

$$J = \int_0^\infty F_D(\lambda)\varepsilon_A(\lambda)\lambda^4 d\lambda \tag{2.11}$$

Here, $F_D(\lambda)$ is the normalized luminescence spectrum of the donor and $\varepsilon_A(\lambda)$ is the absorption spectrum of the acceptor. This integral accounts for the thermal fluctuations of the donor and acceptor energy states, because of which the resonance condition between them is satisfied within only a fraction of time [95]. Finally, the occurence τ_D comes from the fact that the spontaneous emission rate of a dipole is proportional to the square magnitude of its dipole moment:

$$k_D = 1/\tau_D \sim \mu_D^2/\epsilon\hbar\lambda^3 \tag{2.12}$$

This means that the rate of FRET is directly proportional to the radiative recombination rate $k_D = 1/\tau_D$. In the presence of additional nonradiative

processes in the excited state recombination of the donor, Equation 2.10 can be rewritten as

$$k_T = \frac{\langle\kappa^2\rangle QY}{R^6\tau}\frac{9\ln 10}{128\pi^5 N n^4}J \tag{2.13}$$

Here, QY is the quantum yield of the donor and τ is the excitation lifetime of the acceptor. QY of an emitter is the ratio of the number of emitted photons to the total number of excited particles. Quantitatively, if an emitter can decay through i radiative pathways with rates k_1, k_2... k_i and j nonradiative pathways with rates k_1', k_2'... and k_j', then the QY is given by

$$QY = \frac{\sum_{n=1}^{i} k_n}{\sum_{n=1}^{i} k_n + \sum_{n=1}^{j} k_n'} \tag{2.14}$$

QY is a measure of how efficiently an emitter can emit a photon after it absorbs one. Therefore, QY is occasionally referred to as *quantum efficiency* as well. In the case of a single radiative process with rate k_D and a single nonradiative process with rate k_D', $QY = k_D/(k_D + k_D')$ and $\tau = 1/(k_D + k_D')$. It can therefore be deduced that $\tau_D = QY \cdot \tau$.

Similar to the quantum efficiency, the FRET efficiency can be defined as

$$\eta_{FRET} = \frac{k_T}{k_T + 1/\tau} \tag{2.15}$$

In order to characterize the range of FRET, Förster defined the distance R_0, at which the rate of FRET is equal to the rate of excited state recombination in the absence of an acceptor. Using Equation 2.13, this distance can found as

$$R_0 = \left(QY\frac{\langle\kappa^2\rangle 9\ln 10}{128\pi^5 N n^4}J\right)^{1/6} \tag{2.16}$$

This length is commonly referred to as Förster radius, at which $k_T = 1/\tau$. From Equation 2.15, it is easily seen that the FRET efficiency at Förster radius is 50%. If Förster radius is known, the rate of FRET can also be calculated using

$$k_T = \frac{1}{\tau}\left(\frac{R_0}{R}\right)^6 \tag{2.17}$$

Inserting this expression into Equation 2.15, the FRET efficiency can be restated as

$$\eta_{FRET} = \frac{1}{1 + (R/R_0)^6} \tag{2.18}$$

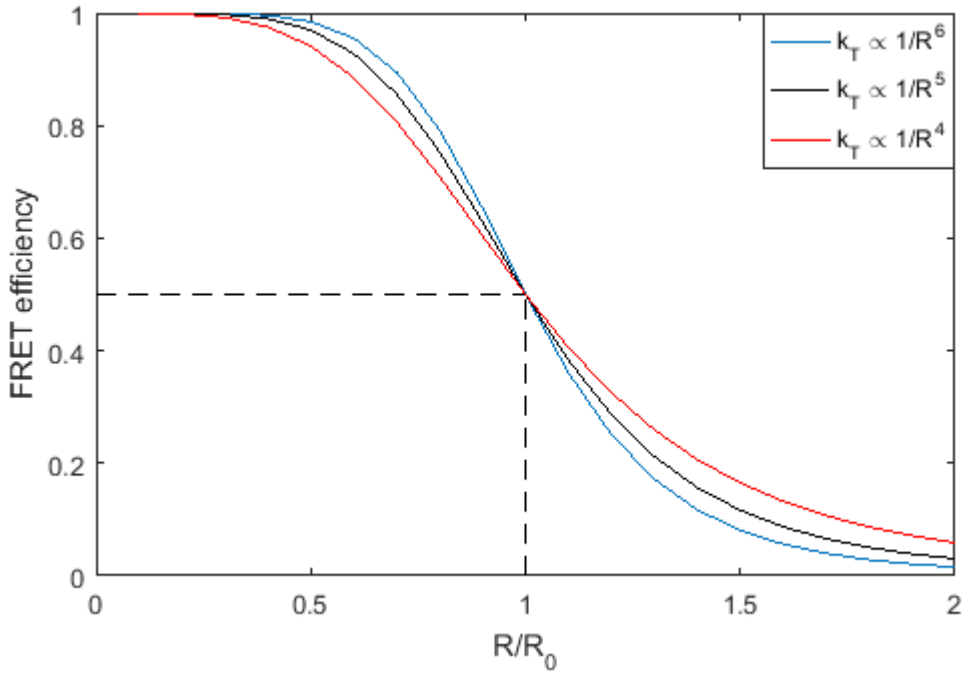

Figure 2.11: Plot of FRET efficiency as a function of donor-acceptor distance when the rate of FRET is proportional to $1/R^6$ (blue curve), $1/R^5$ (black curve) and $1/R^4$ (red curve).

The plot of FRET efficiency as a function of R is shown in Figure 2.11 (blue curve). It can be seen that the efficiency is 0.5 at $R = R_0$. It is also evident that the FRET efficiency is extremely sensitive to R at around $R = R_0$. This feature of FRET, caused by the R^{-6} distance dependence, can be used as a nanoruler in molecular-scale distances on the order of Förster radius.

It should be noted that the R^{-6} distance dependence holds in the case of a single pair of donor and acceptor. In general, the distance scaling depends hugely on the acceptor geometry [96]. Furthermore, when multiple acceptors are in the proximity of an acceptor, the total FRET rate can also have a different distance scaling. As an example, we will consider two hypothetical cases, where the acceptors form i) a one-dimensional (linear) or ii) a two-dimensional (planar)

array. These configurations are demonstrated in Figure 2.12. Assuming a continuous and uniform distribution of randomly oriented acceptors along the array, the rate of FRET to the acceptors around a point l (see Figure 2.12) is

$$k_T(l) = \frac{C}{r^6}\sigma_{1D}dl \tag{2.19}$$

where $r = \sqrt{R^2 + l^2}$, σ_{1D} is the 1D density of acceptors and

$$C = \frac{2}{3}\frac{QY}{\tau}\frac{9\ln 10}{128\pi^5 N n^4}J \tag{2.20}$$

is used in place of all the constant factors in Equation 2.13 ($\langle\kappa^2\rangle$ is replaced with 2/3 due to the assumption of random acceptor orientation). Then the total rate of FRET to anywhere on the array is found by

$$k_{T,1D} = \int_{l=-\infty}^{\infty} \frac{C}{(R^2 + l^2)^3}\sigma_{1D}dl = \frac{3\pi\sigma_{1D}}{8}\frac{C}{R^5} \tag{2.21}$$

Therefore, in the case of one-dimensional array of acceptors, the distance dependence of FRET is R^{-5}. Similarly, in the case where the acceptors are distributed across an infinite plane, the total FRET rate to the plane of acceptors is

$$k_{T,2D} = \int_0^{\infty}\int_0^{2\pi} \frac{C}{(R^2 + \rho^2)^3}\sigma_{2D}\rho d\rho d\phi = 2\pi\sigma_{2D}\frac{C}{R^4} \tag{2.22}$$

where σ_{2D} is the surface density of acceptors. This time, the distance dependence turns out to be R^{-4}. One can see that the increase in acceptor dimensionality results in the reduction of the distance dependence. Following this pattern, it can indeed be shown that in the case of a three-dimensional acceptor (i.e. bulk materials), the distance dependence is R^{-3} [97].

The additional plots in Figure 2.11 show the effect of the change of distance scaling of FRET. As the distance-dependence parameter gets smaller, the steepness of the FRET efficiency curve diminishes. As a result, the sensitivity of FRET to the distance is reduced while FRET at longer distances becomes more significant.

Since FRET is an additional nonradiative channel that competes with the other recombination channels of the donor, it alters the fluorescence decay rate.

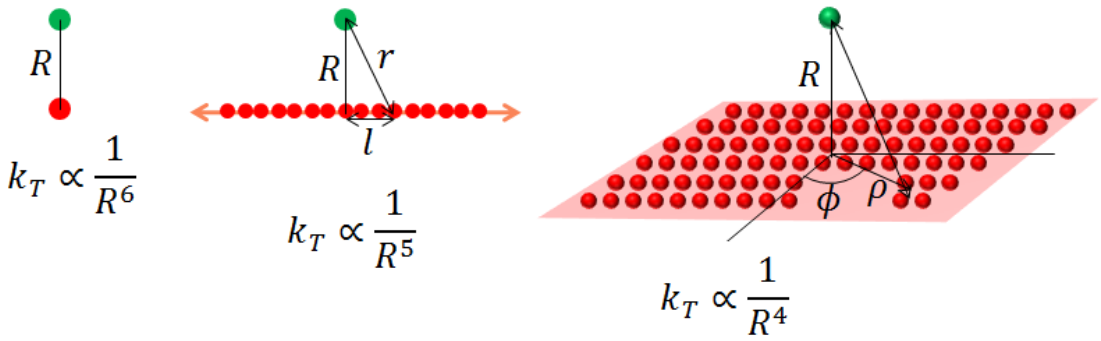

Figure 2.12: Distance dependence of FRET for different acceptor dimensionalities

In the presence of an acceptor, the modified decay rate, k_{DA}, becomes

$$k_{DA} = \frac{1}{\tau_{DA}} = \frac{1}{\tau_D} + k_T \tag{2.23}$$

where $\tau_{DA} = 1/k_{DA}$ is the fluorescence lifetime of the donor in the presence of the acceptor. Experimental measurement of the FRET rate is therefore possible through this relation. Specifically, if the fluorescence lifetime of the donor in the absence and in the presence of the acceptor is measured, one can extract

$$k_T = \frac{1}{\tau_{DA}} - \frac{1}{\tau_D} \tag{2.24}$$

It should be noted that the FRET rate calculated in this fashion for donor-acceptor ensembles will reveal merely average behavior since in such ensembles the donor-acceptor distance is typically not constant for different donor-acceptor pairs. Theoretical treatment accounting for the variations in donor-acceptor distance is possible for homogeneous solutions [93].

As FRET is observed in fluorescent peptides and proteins, it is commonly employed in biological applications including biosensing [98], fluorescence microscopy imaging [99], distance measurement [100, 101], and protein folding detection [102]. FRET is also present in the nature; for instance, the leaves in plants make use of a FRET mechanism to carry the solar excitation to the cells capable of processing it [103]. However, FRET gained further attraction after the introduction of inorganic NCs as not only are they highly emissive fluorophores, but they also have large absorption cross sections, allowing the opportunity for high-throughput FRET. Their bandgap tunability facilitates their incorporation with fluorophores of different classes.

2.3.1 FRET Using Colloidal Nanocrystals

The fundamental principles of FRET with NCs are similar to the molecular FRET process discussed above. Similar to other flurophores, FRET with NCs also takes place due to the near-field dipole-dipole interactions. Resonance in energy states and close proximity of emitters are still necessary conditions for FRET. The FRET with NCs as donor and acceptor is illustrated on the energy diagrams on Figure 2.13. Since the exciton relaxation is many orders of magnitude faster than FRET, the FRET is commonly from the band edge excitonic state of the donor.

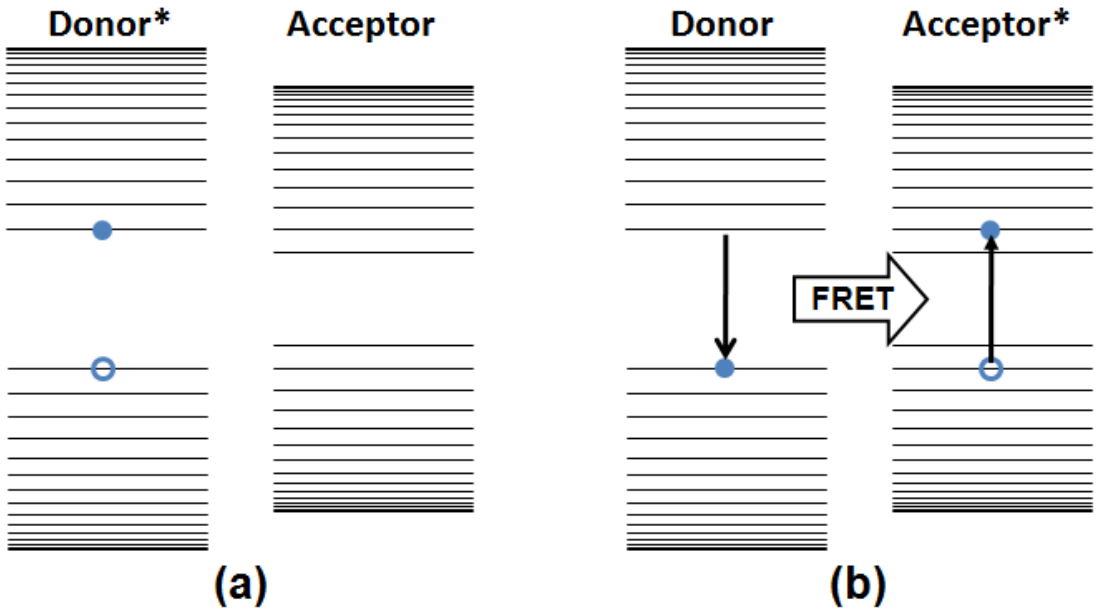

Figure 2.13: Band diagrams of a donor and acceptor NC (a) before and (b) after FRET. Asterisk indicates the particle in the excited state in both panels.

It should be noted that, since NCs are generally larger particles compared to the fluorescent molecules often encountered in biological research, their FRET rate does not always have R^{-6} dependence. This is mainly because the NC sizes are often comparable to the inter-particle separation, in which case the fluorophores cannot be treated as point particles. Even if they could be treated as point dipoles, it is sometimes necessary to account for the inhomogeneity in the medium such as the NC-ligand and NC-solvent interfaces, to obtain an accurate FRET theory of NCs. More often than not, numerical treatment is necessary [96, 97].

FRET with NCs is most frequently encountered in their close-packed thin films. In such a NC ensemble, FRET can even take place multiple times before exciton recombination. In the case of a size dispersion in the ensemble, the exciton energy will tend to flow from smaller-sized NCs having wider bandgap to larger-sized NCs having narrower bandgap. This has indeed been observed in one of the earliest reports on FRET with colloidal semiconductor QDs [104], a few years after the introduction of Cd-based colloidal NC synthesis. Therein, the authors studied the time-resolved fluorescence spectroscopy of the QD ensembles, and observed the acceleration of the fluorescence decay at the blue tail of the ensemble and the deceleration of the decay at the red tail, due to the additional excitation energy being fed into the larger size QDs through the FRET channel. In the case of QDs, due to a significant Stokes shift and the quick relaxation of acceptor exciton to its band edge, energy cannot undergo back-transfer in order to migrate back to the original donor. However, when the Stokes shift and the inhomogeneous broadening are low, bi-directional energy transfer is also possible. This kind of bi-directional FRET was demonstrated in stacks of CdSe CQWs [81]. The unusually low Stokes shift, together with the absence of inhomogeneous broadening, in the core CQWs leads to significant spectral overlap between two identical CQWs. As a result, CQW-to-CQW FRET rates as fast as $(3\ \text{ps})^{-1}$, near-unity FRET efficiency, and a remarkable Förster radius of 13.5 nm were observed [81].

The spectral tunability of NCs can be used for controlling the direction of FRET. Such an approach was proposed and demonstrated with differently sized CdTe QDs, deposited layer-by-layer on solid substrates, sorted by their bandgap [21]. As a result, the exciton could be "funneled" from the large-bandgap NCs to the small-bandgap ones. This cascaded FRET system was used to greatly enhance the exciton density in the layer of the lowest-bandgap, red-emitting QDs, which is the final destination of the excitonic energy in their layered QD structure, by "saving" the excitons trapped in the surface states of QDs at upper layers through FRET [21].

As much as FRET among NC ensembles gained attraction, studies where NCs were paired with many different types of particles, including carbon nanotubes [105, 106], proteins [107, 108], and 2D materials [109, 110] as well as

bulk semiconductors [111, 112] have also stimulated interest. This ability of NCs to electromagnetically couple to particles from distinct classes (*via* dipole-dipole interactions) enables FRET to be studied from many different perspectives and aspects in a broad range of areas, which, in return, can enjoy the favorable properties of NCs and their FRET for applications ranging from biosensing [106] to fluorescence imaging microscopy [113].

2.4 Optical Gain

The term "gain" in optics is related to the amplification of light within an optical mode by the light present in the same mode. It is an essential process in the operation of lasers. To review its basics, we shall begin with some fundamental processes related to light-matter interactions, namely, the processes of absorption, spontaneous emission, and stimulated emission.

Consider a two-level system as shown in Figure 2.14, where the energies are E_1 and E_2 for the ground and excited states, respectively. If the system is initially in the ground state, an incident photon with energy $\hbar\omega = E_2 - E_1$ can excite it to the second level (upward transition), being annihilated concomitantly. This is the process of optical absorption, which is briefly discussed in Section 2.1. The probability of absorption depends on the availability of the resonant states, the number of photons in the mode and absorption cross-section of the system, which is a measure of the magnitude of the transition matrix element between the two states.

If the system in the excited state decays spontaneously (downward transition), without being induced by any external stimuli, and emits a photon with energy $\hbar\omega$ in the process, this is called *spontaneous emission*. Spontaneous emission is a random process, where the duration of the excited state has an exponential distribution. Therefore, the rate of the spontaneous emission is characterized by the parameter of this distribution. In general, the rate of spontaneous emission is also related to the absorption cross-section, as well as the density of modes in

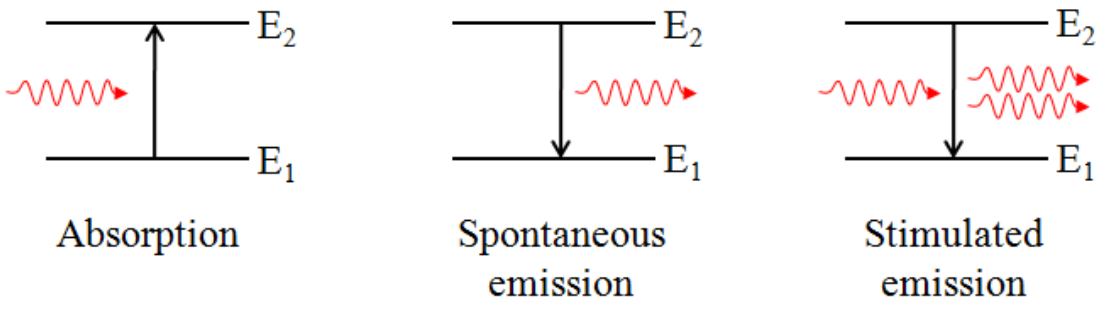

Figure 2.14: Fundamental processes related to the interaction of light and matter: Absorption (left), spontaneous emission (middle) and stimulated emission (right).

the cavity at energy $\hbar\omega$.

If the system is in the excited state and there are photons present in the mode, these photons might induce the emission of another photon into the same mode while the system decays back to the ground state (downward transition). This is called *stimulated emission*. Stimulated emission is the inverse of the absorption process; and just like absorption, its propability also increases with the number of photons in the mode. Indeed, for the same number of photons in a mode, the probability of transition from ground to the excited state is exactly equal to the probability of the transition from the excited state to the ground state.

Stimulated emission is the fundamental process in the phenomenon of optical gain because it increases the number of photons in an optical mode. At the same time, the process of absorption tends to decrease the number of photons, causing optical loss. Therefore, in a gain medium consisting of many identical emitters, the optical gain due to the stimulated emission must be larger than the optical loss due to absorption and additional loss mechanisms, if any. This necessitates that the number of emitters in the excited state to be larger than the number of emitters in the ground state. This condition is called *population inversion*. To achieve population inversion, the emitters in the gain medium must be sufficiently pumped so that a high fraction of them are in the excited state. We discuss the population inversion in hypothetical cases of two-level and three-level gain systems.

Let us first consider a two-level system similar to that in Figure 2.14,

with states 1 and 2, which have energies E_1 and E_2, respectively, as seen in Figure 2.15a. Let N_{tot} be the number of emitters per unit volume in the medium, and N_1 and N_2, the densities of the emitters in the ground and excited state, respectively, so that $N_1 + N_2 = N_{tot}$. The possible transitions in these two-level systems are spontaneous emission from the excited state (state 2) to the ground state (state 1), excitation from the ground state to the excited state by pumping with $\hbar\omega = E_2 - E_1$, and stimulated emission, which causes transition from the excited state to the ground state. The rate of change of the number of emitters in the excited state can be expressed by

$$\frac{dN_2}{dt} = W_i N_1 - W_i N_2 - \frac{N_2}{\tau_{21}} \tag{2.25}$$

where W_i is the probability density of the stimulated emission of an emitter, which also equals to its probability density of absorption in a two-level system, and τ_{21} is the spontaneous transition rate from the excited state to the ground state. The populations in the two states can be found by setting $dN_2/dt = 0$, which yields

$$(W_i + \frac{1}{\tau_{21}})N_2 = W_i N_1 \tag{2.26}$$

Therefore, in a two-level system, the population of the ground state emitters will always be greater than the excited emitters and population inversion cannot be achieved.

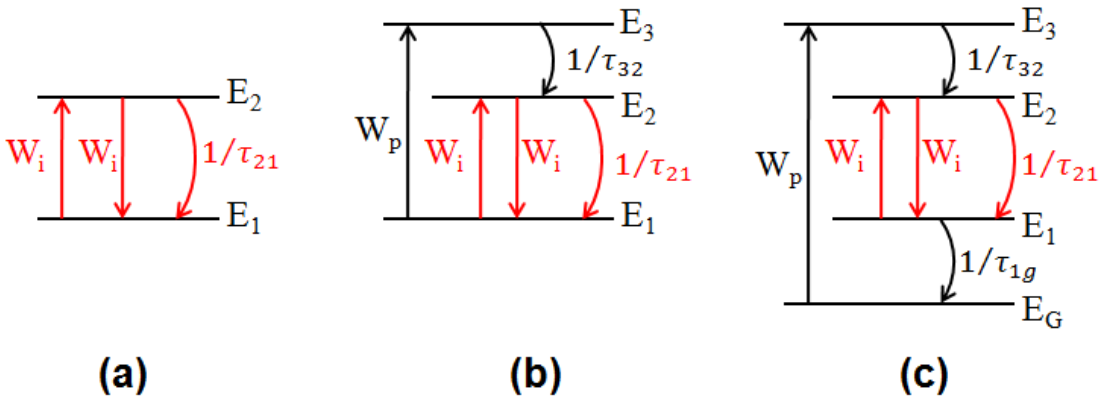

Figure 2.15: (a) Optical transitions on a (a) 2-level, (b) 3-level, and (c) 4-level system. Transitions related to the optical gain are marked red. Downward transitions between non-consecutive states are not shown in (b) and (c).

Adding a third state to the system makes it possible to observe population

inversion. Here, the transition of interest is still 2→1, but the pumping will be from the ground state (state 1) to a third state with energy E_3 this time, 1→3, as seen in Figure 2.15b. Considering the decay lifetimes for all three possible downward transitions, τ_{21}, τ_{31} and τ_{32}, the favorable condition for population inversion is $\tau_{31} \gg \tau_{21} \gg \tau_{32}$, since this condition makes it easier for electrons to "populate" in state 2. Following the diagram in Figure 2.15b, the rate equations are

$$\begin{aligned} \frac{dN_3}{dt} &= W_p N_1 - \frac{N_3}{\tau_{31}} - \frac{N_3}{\tau_{32}} \\ \frac{dN_2}{dt} &= W_i N_1 + \frac{N_3}{\tau_{32}} - W_i N_2 - \frac{N_2}{\tau_{21}} \end{aligned} \tag{2.27}$$

where W_p is the pumping rate from state 1 to state 3 and W_i is the rate of transition between states 1 and 2 due to stimulated emission, given by

$$W_i = \phi \sigma_{21} \tag{2.28}$$

Here, ϕ is the photon flux density and σ_{21} is the cross-section of the transition between states 1 and 2. Neglecting the 3→1 transition, the steady-state solution reveals the population different $N = N_2 - N_1$ to be

$$N = N_1 \frac{W_p - \frac{1}{\tau_{21}}}{W_p + \frac{1}{\tau_{21}}} \tag{2.29}$$

We see that, this time, population inversion is possible when $W_p > 1/\tau_{21}$. Therefore, the 3-level system is suitable for optical gain, given that the pumping intensity is sufficient.

Similarly, for a four-level system, such as the one drawn in Figure 2.15c, the rate equations can be written as follows:

$$\begin{aligned} \frac{dN_3}{dt} &= W_p N_g - \frac{N_3}{\tau_{32}} \\ \frac{dN_2}{dt} &= W_i N_1 + \frac{N_3}{\tau_{32}} - W_i N_2 - \frac{N_2}{\tau_{21}} \\ \frac{dN_1}{dt} &= W_i N_2 + \frac{N_2}{\tau_{21}} - W_i N_1 - \frac{N_1}{\tau_{1g}} \end{aligned} \tag{2.30}$$

Here, the ground state is labeled as g. 3→1, 3→g and 2→g transitions are neglected since they are assumed to be very slow. The stimulated emission arises

from 2→1 as it does in the 3-level system. When $\tau_{32} \ll \tau_{21}$ and $\tau_{1g} \ll \tau_{21}$, the steady-state solution reveals that

$$N = N_{tot}\frac{W_p\tau_{21}}{1 + W_p\tau_{21} + W_i\tau_{21}} \tag{2.31}$$

where $N_{tot} = N_g + N_1 + N_2 + N_3$ is the total number of emitters per unit volume. Therefore, in such a four-level system, N_2 is always greater than N_1 so a minimum pumping intensity for achieving population inversion is not required. Under small signal condition, where $W_i \sim 0$, Equation 2.31 reduces to

$$N = N_{tot}\frac{W_p\tau_{21}}{1 + W_p\tau_{21}} \tag{2.32}$$

Population inversion in optical gain media is achieved by continuously pumping the emitters in the gain medium into the excited state, as seen in Figure 2.16. In such an optical amplifier, the emitted photons stimulate further emission along the optical path. Therefore, the photon flux density increases exponentially. Specifically, the number of the photons gained per unit time per unit volume will be $(N_2 - N_1)W_i = NW_i$, where $N_1(N_2)$ is the density of emitters in state 1(2) as defined previously. If the difference between the photon flux densities entering and exiting a cylinder with incremental thickness dz in the gain medium, such as sketched in Figure 2.16, is $d\phi$, then [29]

$$d\phi = NW_i dz \tag{2.33}$$

Therefore,

$$\frac{d\phi}{dz} = NW_i = N\sigma\phi \tag{2.34}$$

It thus turns out that the photon flux density at a point z can be written as

$$\phi(z) = \phi(0)e^{\gamma z} \tag{2.35}$$

where $\gamma = N\sigma$ is the gain coefficient. It should be noted that this derivation still holds even when $N_1 > N_2$, i.e., when there is no population inversion. In that case, the exponent in Equation 2.35 will be negative, and γ will correspond to the loss coefficient. Instead of being amplified along the propagation direction, the photon flux density will decrease exponentially. When γ is zero, there is no

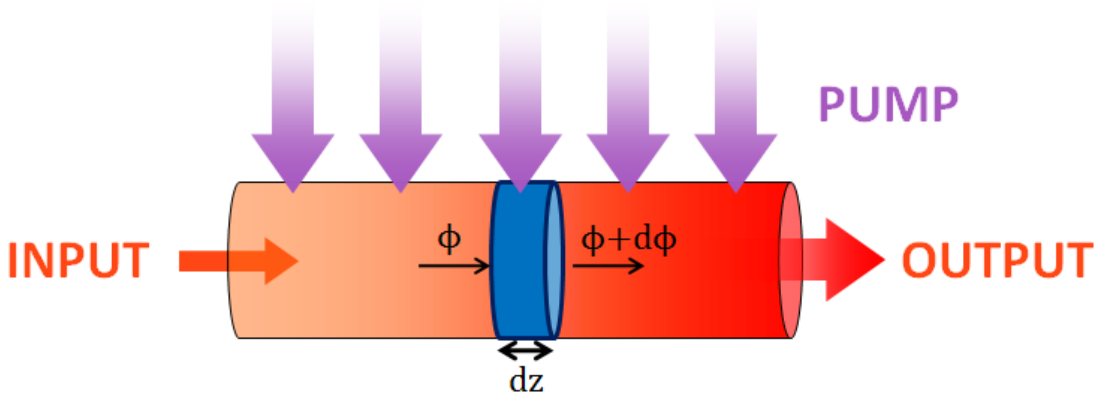

Figure 2.16: Schematic of optical amplification process.

net gain or loss, in which case the intensity of the input light will equal to that of the output light and the gain medium is therefore said to be transparent.

In lasers, optical amplification is combined with feedback, which is provided with mirrors (reflectors) that reflect the amplified stimulated emission back onto the gain medium. One of these mirrors are partially transmitting, which provides the laser output. The question remains, however, as to which material to use for the optically active medium, which would produce the emission to be amplified in the first place. Among the emitters that were commonly used in the lasers are solid crystals such as neodimium-doped yttrium aluminum garnet ($\lambda = 1.06$ µm), atomic gases such as He-Ne ($\lambda = 633$ nm), and organic dyes [29]. In addition to these materials, colloidal NCs have also been shown to be suitable as optical gain materials, especially because of their high emission tunability, high absorption cross-sections and solution processability.

2.4.1 Optical Gain of Nanocrystals

Prospects of colloidal NCs for lasing have been intensely studied for the last two decades. The first demonstration of the optical gain with NCs was in 2000 by Klimov *et al.*, who showed optical amplification in thin films of CdSe QDs using measurements of transient absorption and PL spectroscopy under pulsed excitation [3]. They figured that the optical gain in these QDs requires

multiexciton formation within a single QD due to the degeneracy of band-edge state. In the case of twofold degeneracy, for instance, a single excitonic state $|X>$ can either be excited to the biexciton state $|XX>$ or decay to the ground state $|0>$. Therefore, the presence of mere single excitons does not suffice for the optical gain. Assuming the transition cross-sections for $|X> \rightarrow |XX>$ and $|X> \rightarrow |0>$ are the same, this means that the biexcitons should outpopulate the unexcited QDs in the gain medium for population inversion.

Assuming each absorption process to be independent, the number of excitons in a QD will have a Poisson distribution with parameter $\langle n \rangle$, which is the average number of excitons per QD, given by

$$\langle n \rangle = \frac{W_p \sigma_p}{\hbar \omega} \tag{2.36}$$

where W_p is the pump fluence and σ_p is the absorption cross-section at the pumping frequency ω. When the population density of QDs with multiexcitons is equal to the population density of unexcited QDs,

$$P_{\langle n \rangle}(0) = \sum_{n>1} P_{\langle n \rangle}(n) \tag{2.37}$$

where

$$P_{\mu}(n) = \frac{e^{-\mu} \mu^n}{n!} \tag{2.38}$$

is the probability mass function of the number of excitons in a QD. Equation 2.37 can be restated as [114, 115]

$$P_{\langle n \rangle}(0) = 1 - P_{\langle n \rangle}(0) - P_{\langle n \rangle}(1) \tag{2.39}$$

or, equivalently,

$$e^{-\langle n \rangle}(2 + \langle n \rangle) = 1 \tag{2.40}$$

which holds for $\langle n \rangle \cong 1.15$. This number is therefore the minimum of the average excitons per QD that should be achieved for pumping.

The biexcitonic nature of the NC optical gain introduces additional complications due to Auger recombination, which is a nonradiative excitonic decay process where the excitonic energy is transferred to a third charge rather

than being emitted as a photon. This process is depicted schematically in Figure 2.17. While inefficient in bulk materials, Auger recombination is greatly enhanced with decreasing particle size due to increased Coulomb interactions between the excitons and the relaxation of the translational momentum conservation [116, 117]. The Auger recombination time in NCs can be as fast as a few ps, which is much faster than the radiative biexcitonic decay. Therefore, Auger recombination substantially limits the optical gain performance of colloidal NCs. Multiple approaches previously reported to overcome this problem include coating NCs with a graded shell to suppress Auger recombination [114], and charging the NCs to block the creation of a second exciton in the first excited state [115]. Also, inducing the gain in the single exciton regime by introducing huge Stark shift in the biexciton state energy is possible [118] and charging the NCs to block the creation of a second exciton in the first excited state [115]. Approaches that do not reduce Auger process as much may still enable gain but at limited levels much smaller compared to the cases where Auger recombination is slowed down or avoided.

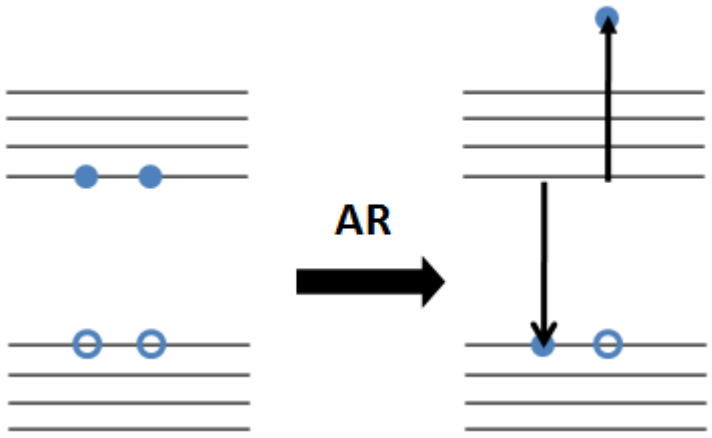

Figure 2.17: Auger recombination in NCs, where energy of one exciton can be transferred to a third charge; in this case, the electron of the other exciton. Excited electron will be highly energetic and might be therefore trapped, creating a charged particle.

Optical gain behaviour in colloidal NCs can be turned into lasing with the use of an optical cavity. Examples of these optical cavities include vertical cavities involving distributed Bragg reflectors [81, 119], distributed feedback grating [45, 120] and various whispering gallery mode structures [4, 121, 122].

In these approaches, the NCs are deposited onto various surfaces, which can vary from flat substrates to microspheres and cylindrical fibers, as thin solid films. Solutions of NCs can also be used as gain media within a Fabry-Perot resonator [123, 124].

NCs can be characterized in terms of their optical gain performance. These characterization techniques involve the detection of *amplified spontaneous emission* (ASE) in the gain medium. ASE is regarded as "amplifier noise" in a resonant gain medium [29] and is normally undesired. However, since ASE is a precursor of lasing, it can be used to study the potential lasing performance of the materials. To this end, a stripe-like region of the material in question is excited with a pump source, and the emission coming from this excited stripe is collected from the side. To account for the ASE, Equation 2.34 can be modified as [29]

$$\frac{d\phi}{dz} = \gamma\phi + \xi_{sp} \tag{2.41}$$

where ξ_{sp} is the photon flux per unit length due to spontaneous emission. Assuming unsaturated gain, the solution to this equation is

$$\phi(l) = \frac{\xi_{sp}}{\gamma}(e^{\gamma l} - 1) \tag{2.42}$$

By varying the length of the excited stripe, the intensity can be recorded as a function of the stripe length, which can then be used to calculate the material's net gain coefficient. This technique is commonly known as variable stripe length characterization.

A similar configuration can be used for the detection of the ASE onset. Herein, the stripe length is fixed whereas the pump intensity is varied. The ASE will be observed only beyond a certain threshold intensity. When the emission intensity is plotted as a function of the pump fluence, a piecewise linear behaviour will be observed. In the presence of ASE, the slope of the curve beyond the ASE threshold will be larger than the slope below the threshold due to the contribution of amplified incoherent light along the pumped stripe. The intersection of the two lines is at the ASE threshold. These techniques, which were originally developed for investigation of optical gain in bulk semiconductors [125, 126], can also be

used for the semiconductor NCs, and will be described in more detail in Chapter 5.

Chapter 3

Self-Assembly of CQWs for Mono- and Multi-layered CQW Superstructures

This chapter focuses on the preparation of large-area, orientation-controlled thin films of colloidal quantum wells (CQWs). These films are prepared using liquid-air interface self-assembly and used for the optical studies that will be discussed in detail in Chapters 4 and 5.

3.1 Orientation-Controlled Monolayers of Self-Assembled CQWs

This section is based on the publication "Orientation-Controlled Nonradiative Energy Transfer to Colloidal Nanoplatelets: Engineering Dipole Orientation Factor" by O. Erdem *et al.*, Nano Letters (2019). Adapted with permission from Ref. [28]. Copyright 2019 American Chemical Society.

CQWs are quasi two-dimensional (2D) semiconductors with atomically flat

lateral surfaces. CQWs have a very small thickness of a few nm's, whereas their lateral dimensions range from several to tens of nm's. Since the lateral dimensions are larger than the exciton Bohr radius, the quantum confinement is significant only along the vertical direction. Having narrow photoluminescence (PL) and large absorption cross-section, CQWs have been already being used as optical gain media with remarkably low gain thresholds [5, 17] and active emitting materials in LEDs [8, 127, 128].

Due to their anisotropic shape, CQWs can take up two different orientations in their solid films. In one of these orientations, the CQWs lie flat on the substrate with their lateral surface parallel to it. This orientation is regarded as *face-down* or *nonstacked*. In the latter orientation, the CQWs stand on their peripheral surfaces and face each other instead of facing down. In this orientation, CQWs stick to each other and form one-dimensional (1D) chains of CQWs. This phenomenon is called stacking, and the orientation is commonly referred to as *edge-up* or *stacked*. Previous reports on the CQW orientations undoubtedly showed that the orientation of the CQWs has a strong effect on the resulting optical properties of the CQW assemblies. Abecassis *et al.*, who reported micrometer-long CQW stacks, observed that the emission out of these 1D CQW chains has polarization [80]. Our group has shown that the stacking of CQWs diminishes their photoluminescence quantum yield (QY) and reduces the excitonic lifetime due to energy-transfer assisted charge trapping within stacks [81]. Later, it has been also shown that the emission pattern of the CQWs depends on their orientation because of the in-plane excitonic dipole of the core CQWs [15].

These previous reports confirm that stacking in CQWs must be controlled and accounted for in order to properly study and utilize the anisotropic optical properties of CQWs. However, conventional methods of sample preparation such as drop-casting and spin-coating lead to CQW ensembles with mixed orientation. To address this problem, liquid-air interface self-assembly technique, where the nanoplates dispersed in an organic solvent are spread over a polar subphase, has been employed, which enabled orientation control of platelet-shaped nanocrystals (NCs). For instance, Paik *et al.* reported the "columnar" and "lamellar"

stacking, which correspond to face-down and edge-up orientations, respectively, of GdF_3 nanoplates by utilizing the interaction of oleate-passivated surfaces of the nanoplates with different liquid interfaces [83]. More recently, Gao *et al.* has shown a similar approach, where the CQW-subphase interaction is modified by mixing oleic acid and diethylene glycol (DEG) in different ratios. Here, they were able to create domains of CQWs in a single orientation. The oleic acid:DEG ratio determined the resulting CQW orientation in these ensembles [15]. However, it was not possible with these approaches to obtain a single monolayer of platelet-shaped NCs with uniform orientation. Although the former study demonstrated orientation controlled film deposition over large areas with full surface coverage, the resulting nanoplate films were in multilayers. In the latter, on the other hand, the domains were reported to be only as long as several micrometers with huge gaps in between them, causing sub-monolayer surface coverage.

In our proposed technique in this thesis, where we also used liquid-air interface self-assembly, we were able to deposit CdSe core CQWs in a single desired orientation, i.e. either all face-down or all edge-up, as a single monolayer, over areas as large as 20 cm^2. To achieve this, we selected appropriate subphases that created uniformly spread CQW membranes with the desired orientation. In addition, we carefully controlled the concentration and amount of the CQW solution to make sure the CQWs are deposited as a single layer. We used square-shaped core CdSe CQWs having 4.5 ML vertical thickness (1.2 nm) and 14.4 $\pm$ 2.0 nm side length, which were synthesized in our group based on a previously reported recipe [14]. The transmission electron microscopy (TEM) image of these CQWs is displayed in Figure 3.1. Prepared by a simple drop-casting of a dilute CQW solution in hexane, we see a mixed CQW orientation with no particular order.

Our self-assembly deposition is illustrated in Figure 3.2: Silicon substrates of 1×1 cm^2 size, coated with 25 nm thick Al_2O_3, are immersed into the subphase contained in a Teflon well. The subphase should be denser than the solvent of CQWs (hexane), and have a high enough polarity to ensure its immiscibility with the CQW solution. Once dropped onto the subphase, the CQW solution spreads across the liquid interface. The CQW solution is then let dry, after which the

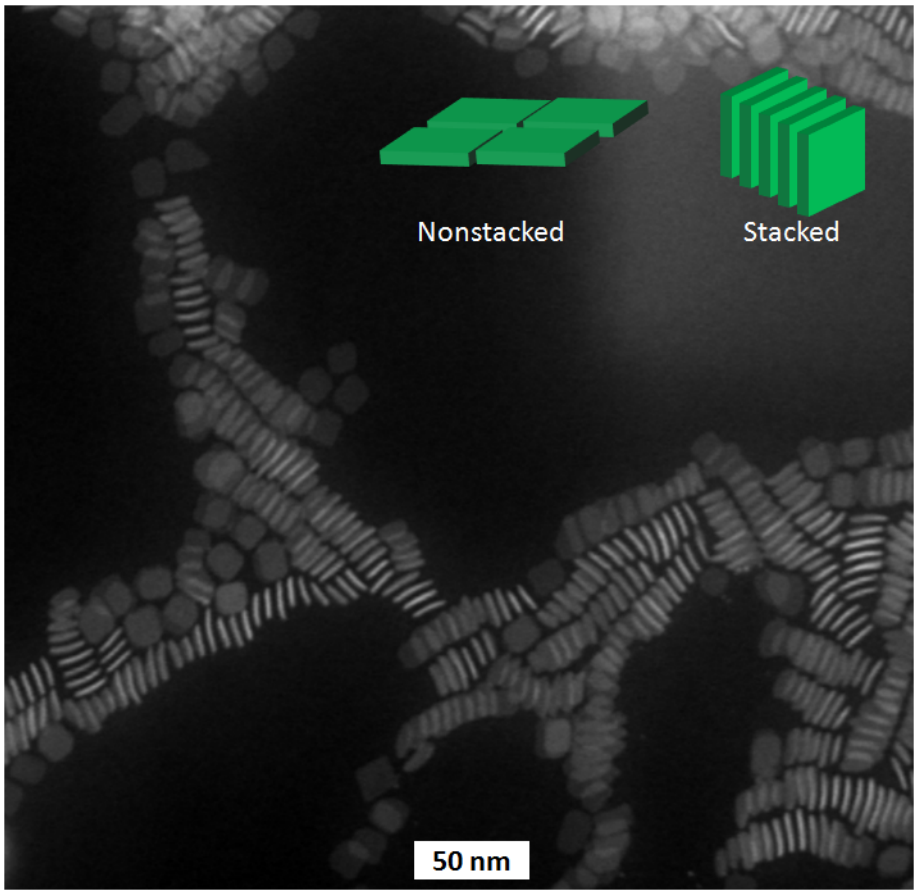

Figure 3.1: High-angle annular dark field scanning transmission electron microscopy (HAADF-STEM) image of 4.5 ML CdSe CQWs. Inset schematically shows the orientation of nonstacked (face-down) and stacked (edge-up) CQWs that co-exist in the shown image. Adapted with permission from Ref. [28]. Copyright 2019 American Chemical Society.

CQWs on the surface form a uniform membrane. This membrane is transferred onto the solid substrates by draining out the subphase slowly with the help of a needle. Finally, the residual subphase in between the substrate and the CQW membrane is evaporated to complete the transfer.

In our approach, we identified acetonitrile (ACN) as the subphase that results in a face-down CQW membrane and ethylene glycol (EG) that yields a stacked one (Figure 3.2). The scanning electron microscopy (SEM) images of the resulting CQW films are shown in Figure 3.3. It can be seen in Figure 3.3a that the self-assembled CQWs deposited using ACN are in fully nonstacked

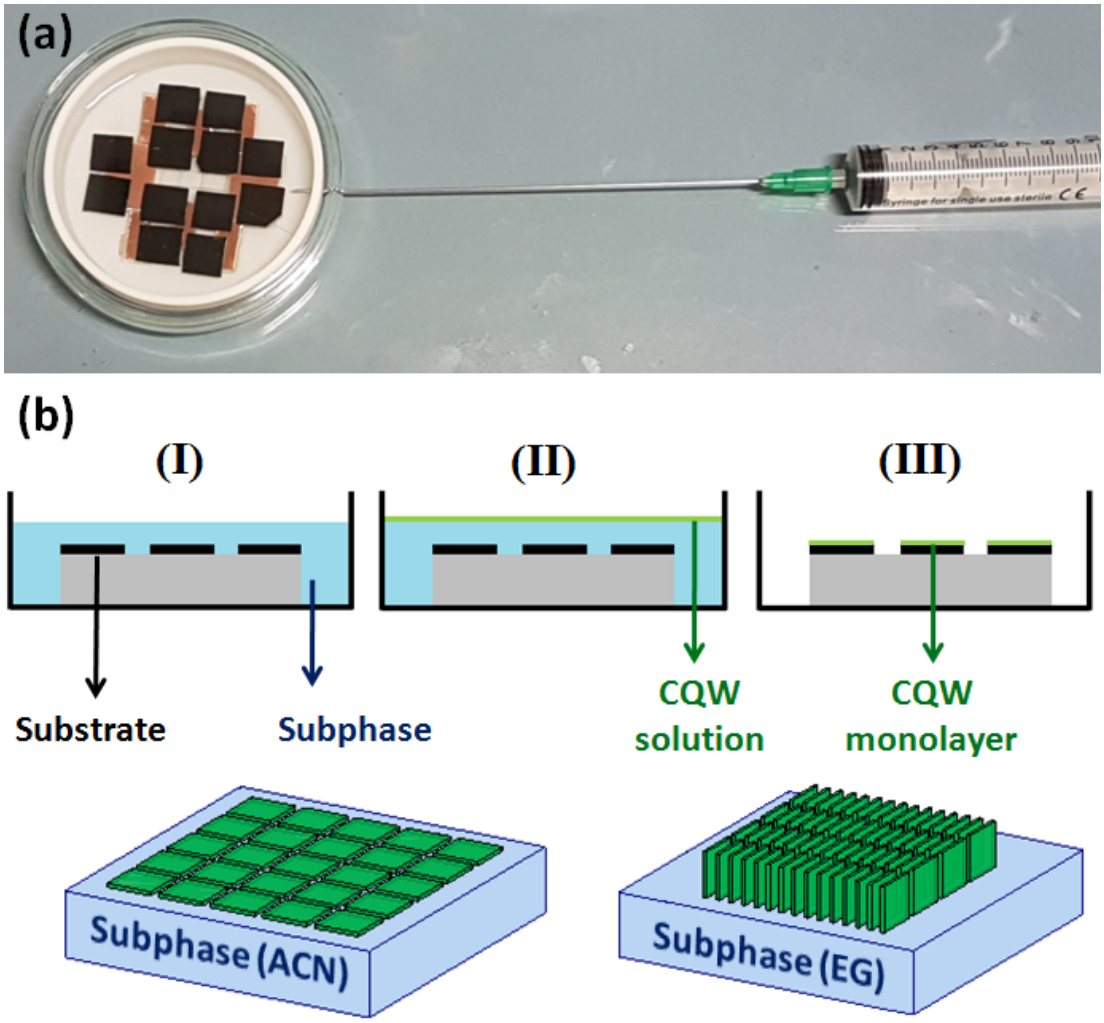

Figure 3.2: (a) Our home-built setup for the self-assembly of colloidal quantum wells and their deposition onto solid substrates. (b) Liquid-air interface self-assembly procedure: (I) Blank substrates are placed inside the subphase. (II) CQW solution is poured onto the subphase and is then allowed to dry. (III) The subphase is drained after the evaporation of the CQW solution. The resulting CQW orientation depends mainly on the subphase chosen. The CQW orientation in the monolayer is face-down for the acetonitrile (ACN) subphase and edge-up for the ethylene glycol (EG) subphase. Adapted with permission from Ref. [28]. Copyright 2019 American Chemical Society.

orientation. Furthermore, apart from minor irregularities, the deposited CQWs form a full monolayer and are as closely packed as possible in nonstacked configuration with little to no gaps between them in the film. The stacked CQWs, which were deposited using EG, are shown in Figure 3.3b. This stacked CQW monolayer displays excellent homogeneity throughout the surface with no apparent aggregation or multilayer formation. The near-unity surface coverage over several mm^2 areas is evident in the SEM images having smaller magnification (Figures 3.3c, d).

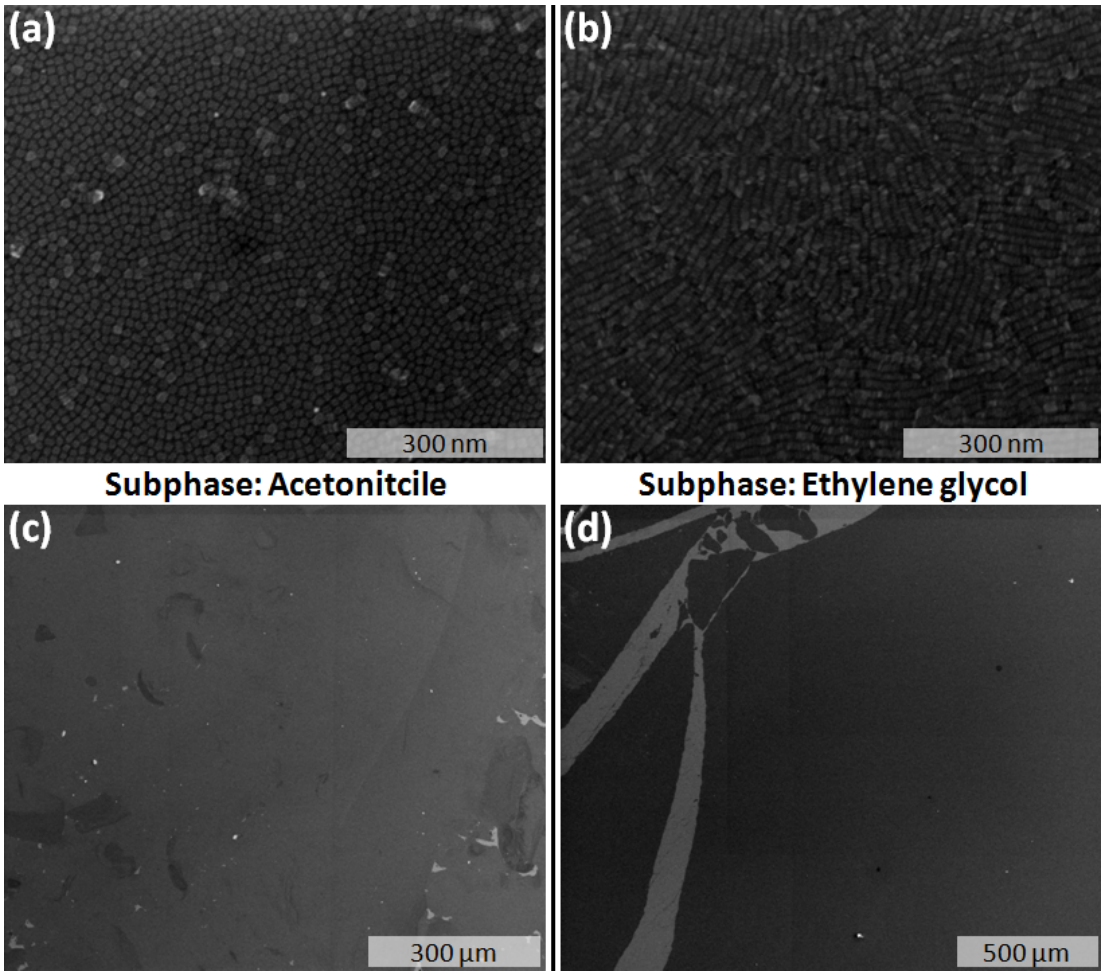

Figure 3.3: Scanning electron microscopy (SEM) images of (a, c) face-down and (b, d) edge-up CQWs deposited with our self-assembly technique. Images in (c) and (d) are taken with a lower magnification to observe the large-scale film deposition. Gaps and crack formation are visible in (c) and (d) (light grey areas), which are mostly formed during the transfer process. Adapted with permission from Ref. [28]. Copyright 2019 American Chemical Society.

In Figures 3.3c and 3.3d, which are large-scale, low-magnification SEM images of face-down and edge-up CQW assemblies, respectively, crack formation can be observed. These cracks form during the transfer of the membrane onto the substrate and create blank regions that might limit the near-unity surface coverage to areas of several mm^2. In order to prevent such crack formation, we make use of a suspension material on the liquid-air interface as previously demonstrated for deposition of close-packed gold nanoparticles [88]. In our case, we used silicone oil (silicone elastomer, Sylgard 184) dissolved in hexane with a concentration of 1.2 mg/mL. We added one drop of silicone oil solution from a blank spot on the edge of the liquid-air interface such that the membrane was compressed and pushed towards over the substrate. With this modified technique, we deposited 2-inch wafers of silicon with thermally grown oxide on their surface. We observed that compression with silicone oil reduces the crack formation and enables a uniform deposition over larger areas. The photographs of the deposited wafers under UV illumination are displayed in Figure 3.4. We have therefore managed to deposit a monolayer of close-packed CQW stacks onto a whole 2-inch wafer, which has an area of $\sim$20 cm^2, by compressing the membrane and choosing a right amount of CQW solution to drop. For this purpose, we made use of the empirical formula given by Yeltik *et al.* [129], which relates the CQW lateral area to its molar absorption cross-section and estimated the necessary CQW concentration and amount to roughly cover the whole liquid interface with a monolayer of CQWs.

It should be noted in the photos of edge-up CQW assembly in Figures 3.4b and 3.4d that the visible emission colour changes significantly with the viewing angle. This can be explained by the out-of-plane band-edge emission of the CQWs, which is dominant near the normal to the CQW lateral surface, and weak for smaller θ (see Equation 2.1). Therefore, when the CQWs lie face-down, their excitonic dipoles are virtually parallel to the substrate, because of which their emission is strong near the normal to the substrate plane (z direction). When they are standing edge-up, however, the dipole will have a component perpendicular to the substrate plane (x-y), forcing some of the emission toward the x-y plane. Therefore, the band edge emission of the edge-up CQWs are much

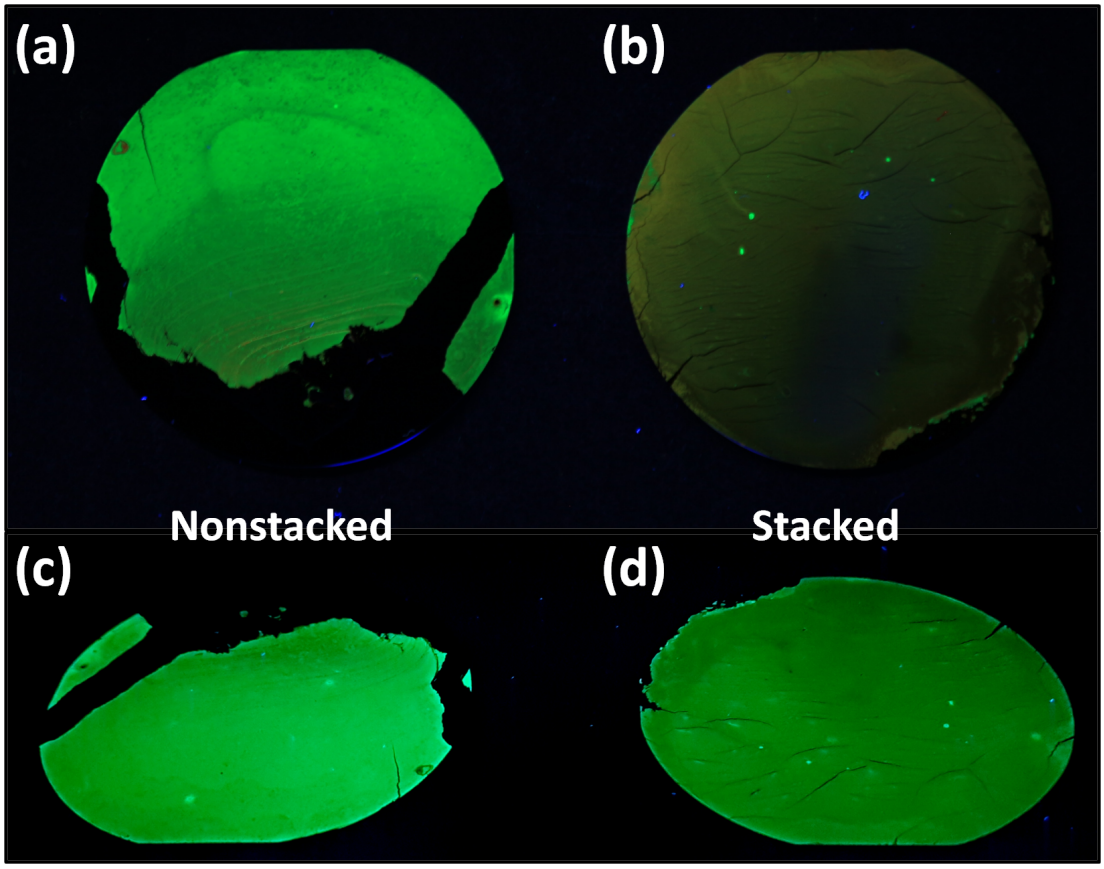

Figure 3.4: Photographs of (a) nonstacked and (b) stacked CQW monolayers deposited onto 2-inch wafers under UV illumination. These photographs were taken from the top. (c) and (d) the same wafers with their photos taken from the side. (c, d) adapted with permission from Ref. [28]. Copyright 2019 American Chemical Society.

stronger when viewed from the side (Figure 3.4d), compared to when viewed from the top (Figure 3.4b). Furthermore, the deep trap emission of the 4.5 ML core CQWs, which is a broad red emission feature [130], is enhanced with stacking [81, 130]. The red emission enhanced by the energy transfer assisted trapping mixed by the weakened band-edge emission might cause the yellowish colour observed from the top. These observations are in accordance with the seminal work of Gao *et al.*, who first demonstrated the out-of-plane band edge emission of core CQWs [15].

The effect of subphase on liquid-air interface self-assembly of GdF_3 nanoplates was previously studied by Paik *et al.* It has been observed that these nanoplates

tend to form a columnar (nonstacked) assembly, with subphases having relatively lower polarity and lamellar (stacked) assembly with more polar subphases. Similarly, Diroll *et al.* studied the effect of subphase on the orientation of CdSe/CdS dot-in-rod NCs. They observed that the spreading speed of the NC solution on the subphase changes with the viscosity and surface tension of the subphase, which in turn change both the orientation and in-plane alignment of the NRs [26]. The results of our self-assembly experiments agree with these previous reports in that, using ACN, which has a polarity of 0.46, results in nonstacked deposition of CQWs on film, whereas EG, whose polarity is 0.79, yields stacked CQW assemblies. We also observed that, when the CQW solution is dropped onto ACN, it quickly spreads across the liquid interface, whereas the drop of CQW solution onto EG, despite being larger in amount than the drop added for nonstacked self-assembly, spreads very slowly over EG interface. It is likely that the evaporation of hexane is faster on ACN compared to evaporation on EG, since quick spread on ACN creates a larger surface of hexane for evaporation. Therefore, a higher concentration of CQW solution over EG is formed while the hexane solution is evaporated. As a result, it is more likely for the CQWs to interact with each other due to a higher CQW concentration, which might induce stacking due to interparticle interactions such as van der Waals forces between ligands of CQWs in close proximity. On the other hand, since CQWs that quickly spread over ACN surface become sufficiently far away from each other before hexane is fully evaporated, they have a minimal interaction in between; hence they remain face-down at the liquid interface. This agrees with the observation of Diroll *et al.*, who reported that for subphases over which NR solution is quickly spread, the NRs are parallel to the planar interface and for slowly spreading NR solutions, the NRs in the superlattice are perpendicular to the substrate [26]. A concurrent observation has been made by Momper *et al.*, who demonstrated that slower evaporation of CQW solution leads to stack formation [92].

In summary, we deposited orientation-controlled CQWs as a single monolayer in a single desired orientation using liquid-air interface self-assembly. The resulting films are composed of CQWs that are either all face-down or all edge-up. Furthermore, these films have a high surface coverage over solid substrates across

areas that are as large as 20 cm^2. The CQW films prepared with this self-assembly technique enables us to study the anisotropic properties of these CQWs. These films have been utilized in studies of orientation-controlled nonradiative energy transfer from colloidal quantum dots to a monolayer of CQWs, which will be discussed in Chapter 4.

3.2 Multilayered Construction of Self-Assembled CQWs

This section is based on our work "Orientation-Controlled Construction of Superstructures of Atomically-Flat Nanocrystals: Pushing the Limits of Ultra-Thin Colloidal Gain Media" by O. Erdem *et al* (2020) [131].

3-dimensional (3D) colloidal NC superstructures have been attracting significant interest since the introduction of colloidal NCs. Monodisperse colloidal quantum dots (QDs) have been commonly employed in creating 3D NC superlattices. Shortly after the introduction of Cd-based QDs, Murray *et al.* demonstrated that monodisperse QDs tend to organize into 3D superlattices with their slow evaporation. More sophisticated approaches, including liquid-air interface assembly [25,88,132], dip coating [133,134] and Langmuir deposition [76, 135] have been utilized to create single-component or binary NC superlattices. However, employment of such techniques for creating superstructures out of non-spherical nanoparticles introduces additional challenges, mainly due to the additional degree of freedom stemming from the NC orientation. Specifically, NCs with an anisotropic shape can adopt different orientations in film, which may create nonuniform assemblies. It was shown that liquid interface assisted deposition techniques can actually help control and dictate a specific orientation of anisotropic NCs such as nanorods (NRs) [24, 26, 136]. More recent studies on self-assembly of CdSe CQWs revealed that liquid-air interface self-assembly can be used also to control the CQW orientation and deposit these CQWs in a single desired orientation [15, 28, 92]. However, these studies were limited to deposition

of only a single layer of CQWs. Multilayered CQW deposition was reported by Suarez *et al.*, employing layer-by-layer deposition via dip coating [27]. Although the monolayer-precision control in the thickness is successfully demonstrated, the challenges related to construction of densely-packed CQWs remain unsolved as this technique requires oppositely charged polymers in between the CQWs to be deposited, which in turn puts a limit to the number of CQWs per unit volume.

Here, we address these issues by proposing and demonstrating a method for construction of multilayered CQW films involving liquid-air interface self-assembly. To this end, we deposited our substrates with self-assembled CQW monolayers sequentially as many times as desired, thereby defining an exact thickness for our films while maintaining a specific orientation and excellent homogeneity throughout the film. This technique allows us to create large-area, orientation-controlled CQW films with monolayer-precise film thickness and unprecedentedly low surface roughness. It is in principle applicable for deposition of arbitrarily large areas. With the help of this technique, we therefore created large-area slabs of CQWs with tunable, precisely-controlled thickness, which can be used as optically active planar waveguides in on-chip optical applications.

For the multilayered CQW deposition, we used CdSe/$Cd_{0.25}Zn_{0.75}S$ core/shell CQWs synthesized according to the recipe previously reported by our group [55]. The CQWs we used have a square-shaped lateral surface with a side length of 17.8 $\pm$ 1.5 nm and a vertical thickness of 4.1 nm as determined from the TEM images (Figures 3.5a ,b). These CQWs have been deposited onto substrates of silicon or fused silica *via* our self-assembled deposition technique. To facilitate the repulsion of the substrate during the draining stage, we functionalized the surface of the substrates using a modification of a previously reported recipe [137]. Precleaned substrates of quartz and fused silica were treated with the vapor of 1H,1H,2H,2H-perfluorodecyltriethoxysilane at 200 °C under nitrogen environment for 30 min, which renders their surfaces hydrophobic. The treated substrates were rinsed in hexane, followed by rinsing in acetone and then in isopropanol. The substrates to be deposited were attached to tilted stages, and fully immersed altogether in DEG (Figures 3.6a,b), which functions as the subphase. Then, the hexane solution of CQWs was dropped onto DEG and quickly spread across the DEG interface as

it evaporated. After the hexane was completely evaporated, a small amount of silicone oil (silicone elastomer, Sylgard 184), which was also dissolved in hexane (with 1.2 mg/mL concentration), was added as a single drop from one edge of the DEG interface. The purpose of the silicone oil is to maintain a compact CQW membrane by compressing it [28, 88]. Then, the subphase was slowly drained with the help of a peristaltic pump at a rate of 50 µL/min, which amounts to 260 nm descent of liquid level per s in the teflon dish of 64 mm in diameter used for deposition. As the subphase was taken out, the CQW membrane eventually sank onto the subtrates, which repelled DEG due to their hydrophobic surface and the tilted placement (by ∼10°). After the draining is complete, the residual droplets of DEG, if any, on the substrates was evaporated under vacuum at room temperature.

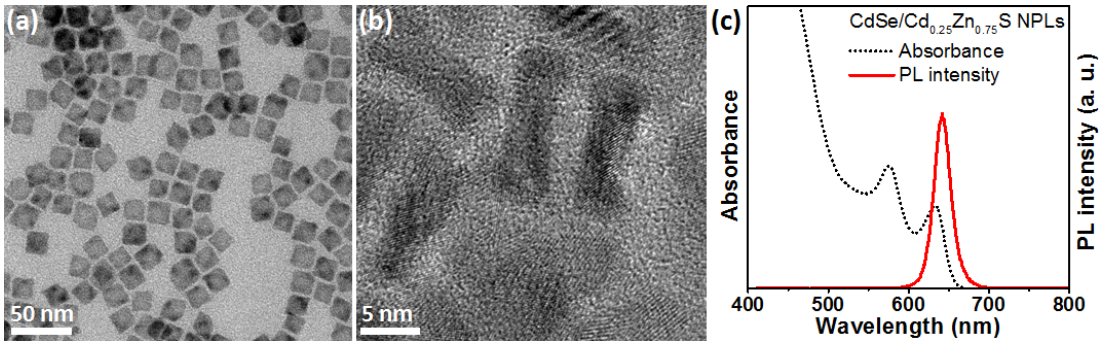

Figure 3.5: (a) Transmission electron micrograph of CdSe/$Cd_{0.25}Zn_{0.75}S$ CQWs used for their self-assembly. (b) TEM image of the same CQWs in vertical orientation. (c) Absorbance (dashed black line) and photoluminescence (solid red line) spectra of these CQWs. Adapted from Ref. [131]

.

At the end of this procedure, one full CQW monolayer was deposited onto the immersed substrates. The SEM image taken from one such substrate is given in Figure 3.6c. The CQWs are seen to be forming a compact monolayer with excellent uniformity and no visible multilayer formation or aggretation. Furthermore, owing to the compression by silicone oil, the deposited CQWs are densely packed, yielding near-unity surface coverage. Larger substrates can also be deposited with this technique, using beakers of appropriate size (Figure 3.6d). As an exemplary demonstration, a 4-inch wafer of fused silica was deposited with the same CQWs. The photographs of this full wafer, illuminated under UV light,

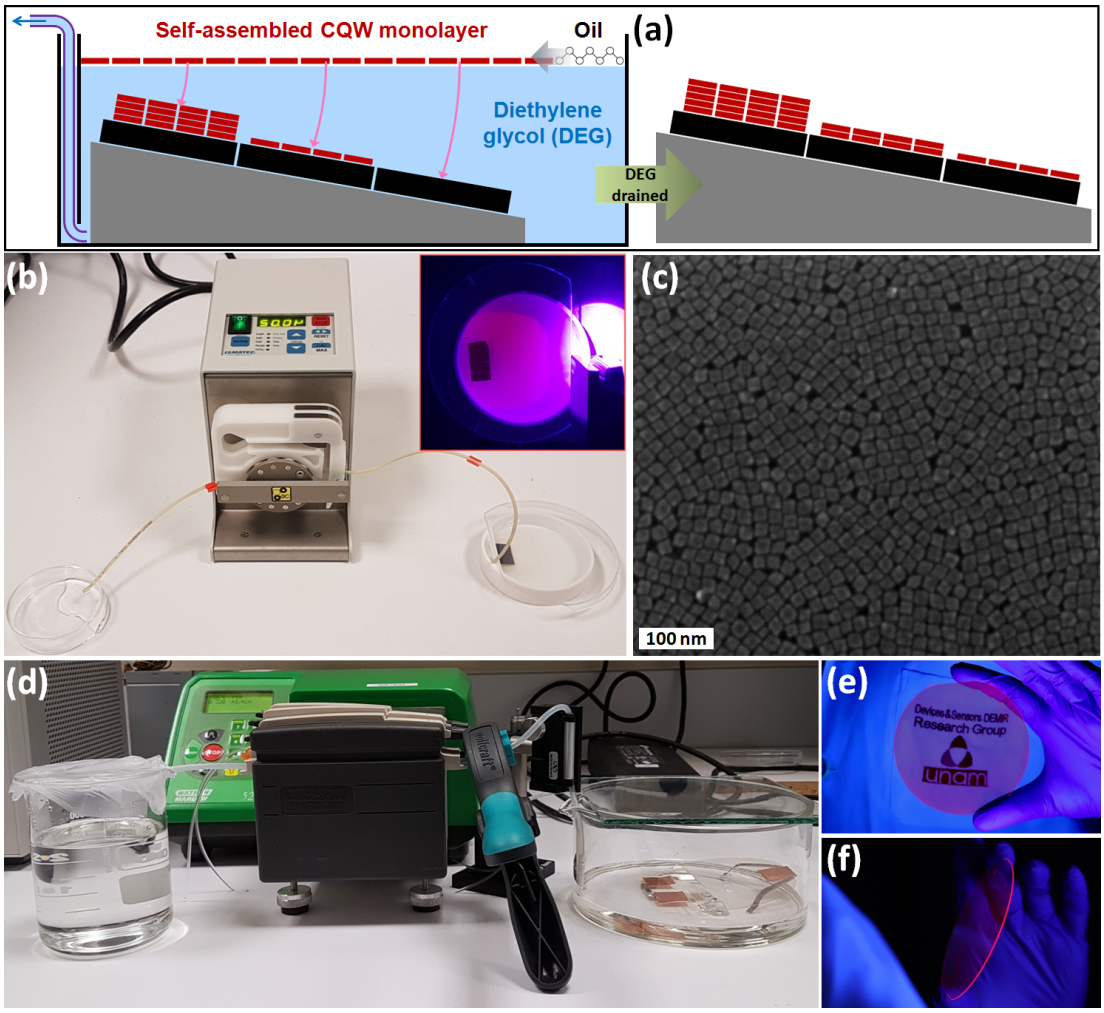

Figure 3.6: (a) Schematic demonstration of our self-assembled CQW deposition. Blank or predeposited substrates are inserted into a subphase of diethylene glycol (DEG). The CQW solution is dropped onto the subphase and quickly spreads across the liquid-air interface. Dropped silicone oil compresses the CQW membrane. After complete evaporation of the hexane, DEG is drained out with the help of a peristaltic pump. As a result, all the substrates are deposited with one additional monolayer of CQWs. (b) Photograph of our home-built setup for the self-assembly. Inset: In-situ photograph of the CQW membrane (red) in the teflon dish illuminated with blue light. The CQW membrane is pushed to the left, towards over the substrates, by the silicone oil solution dropped from the right side of the teflon dish. (c) Scanning electron micrograph of the resulting CQW monolayer deposited. (d) Our self-assembly setup used for the large area deposition. (e, f) Photographs of a 4-inch wafer of fused silica deposited with one monolayer of CQWs, illuminated with UV light, from the top and from the side, respectively. Adapted from Ref. [131].

are given in Figures 3.6e and 3.6f. Uniform emission throughout the wafer is seen in Figure 3.6e. The photo from the side in Figure 3.6f shows strong waveguiding of the PL emission within the wafer.

Owing to the compression of the membrane with silicone oil, the deposited CQWs are densely packed, yielding near-unity surface coverage. Without the assistance of silicone oil, only a fraction of the CQWs on the membrane sticks to the surface during the transfer process, yielding sub-monolayer coverage. The effect of silicone oil on the surface coverage is demonstrated in Figure 3.7, where various depositions with and without (or with insufficient) silicone oil are comparatively shown.Figures 3.7a and 3.7b display SEM images of a Si substrate deposited without any silicone oil-assisted compression. In contrast, when silicone oil is added to the DEG interface for the purpose of membrane compression, we observe a tightly-packed, uniform deposition of CQWs as seen in the SEM images in Figures 3.7c and 3.7d. The contribution of this compression to the surface coverage is also evident at larger scales, as demonstrated in Figure 3.7e with fluorescence images of 4-inch wafers deposited with one layer of CQWs. Here, the wafer on the left was deposited using an insufficient amount of silicone oil for compression, while a sufficient amount of silicone oil solution was used for the one on the right. Illumination of these wafers shows that the emission of the wafer on the left is much dimmer compared to the one on the right, which indicates a sparser deposition of CQWs on the wafer on the left. Furthermore, large-scale cracks and voids have formed on this wafer, which can be attritubed to the lack of membrane compression as well. These comparative results show that proper compression of the CQW membrane is a crucial step in obtaining a uniform, close-packed thin film with our deposition technique.

In order to construct thicker films with multiple CQW layers, we repeated this self-assembly procedure on the same previously deposited substrate as many times as we desired. The resulting films are robust and maintain their strong emission and high uniformity. A cross-sectional TEM image taken from an exemplary case sequentially deposited of 11 CQW layers, displayed in Figure 3.8a, reveals that the CQW layers remain intact and well separated by their surface ligands in between, and do not introduce roughness as they build up. The uniformity

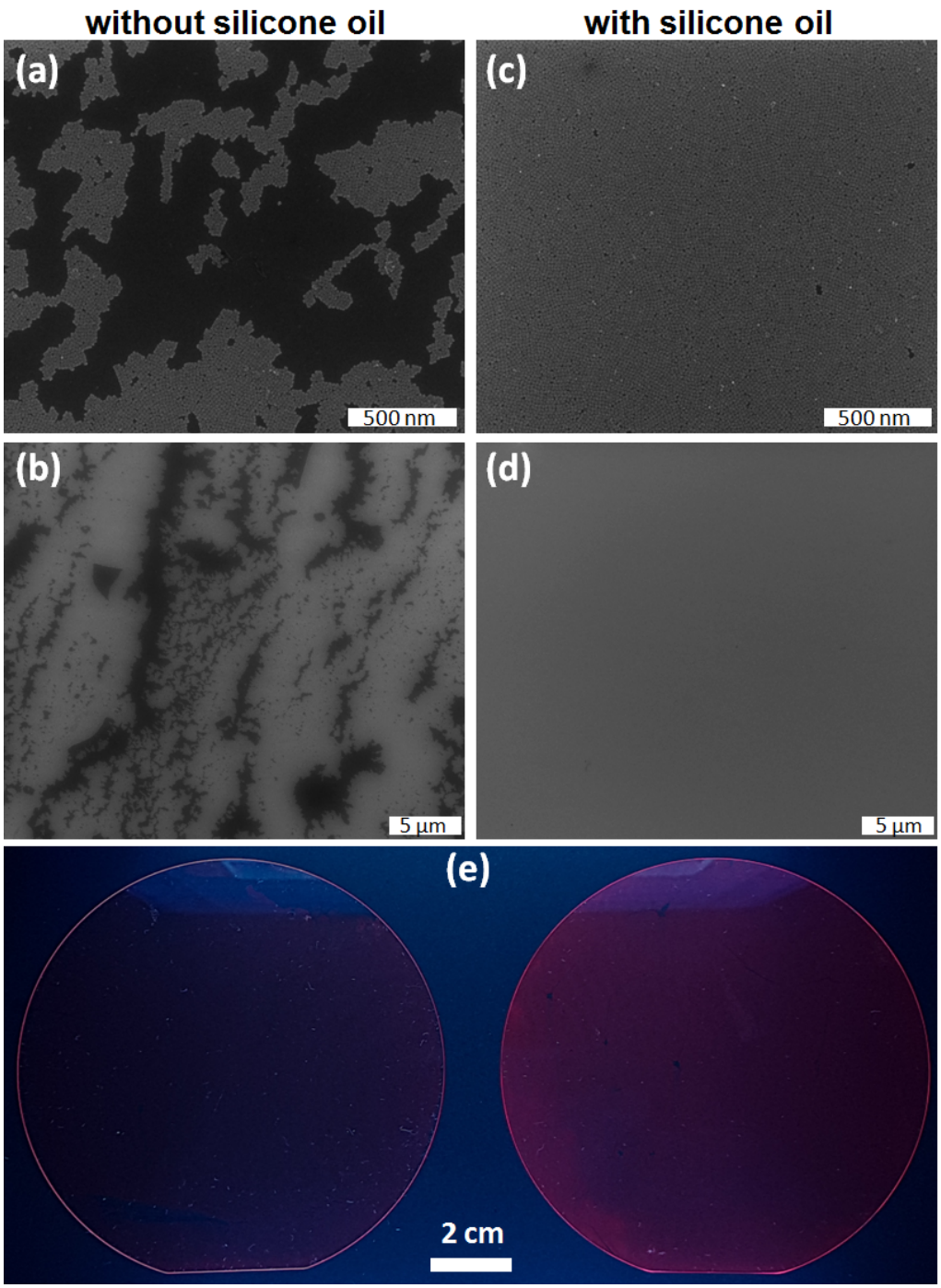

Figure 3.7: Self-assembled deposition of CQWs (a, b) without and (c, d) with membrane compression using silicone oil. In panels a through d, dark areas are void while light areas are covered with CQWs. (e) 4-inch wafers deposited by using insufficient (left) and sufficient (right) amount of silicone oil solution. Adapted from Ref. [131].

of the CQW multilayers continues to persist even over larger areas. Atomic force microscopy (AFM) measurements show that the surface roughness of these multilayered CQW films are unprecedentedly low (Figure 3.8c). Even for the thickest CQW films that were studied (15 layers), which have a thickness of 105 nm, the surface has a remarkably low rms roughness of ∼1.5 nm.

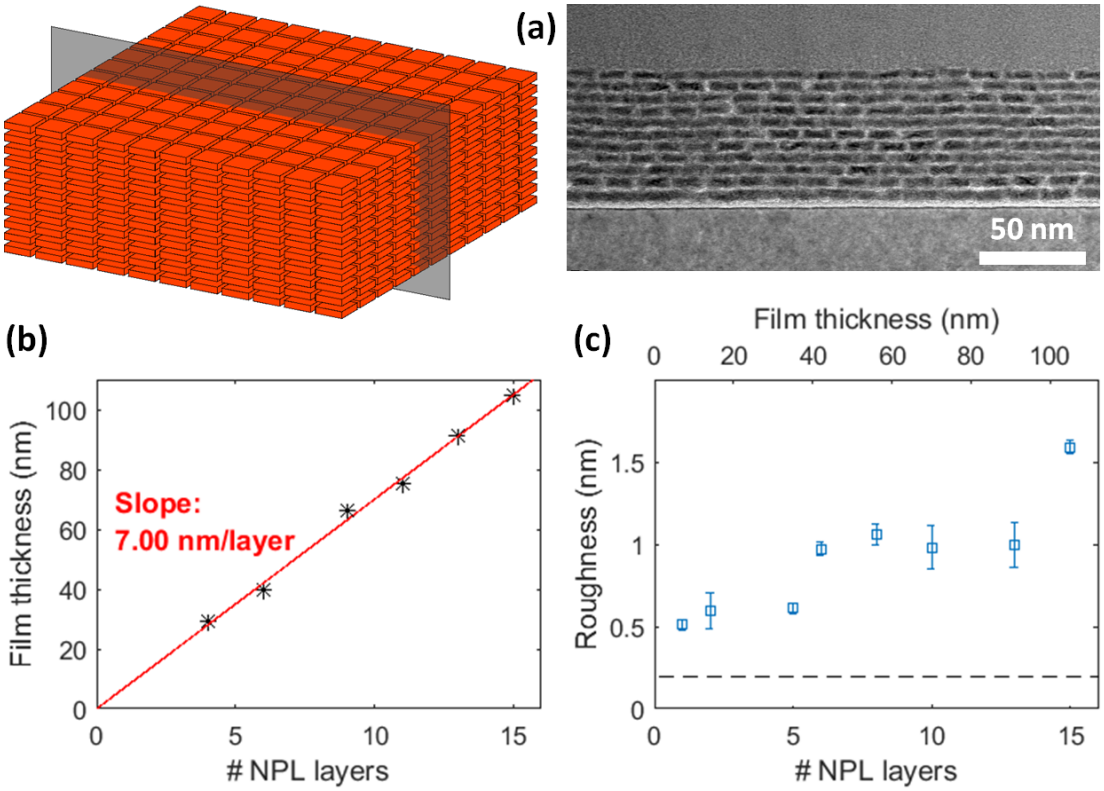

Figure 3.8: (a) Cross-sectional TEM image of 11 CQW monolayers sequentially deposited onto silicon. All the CQW layers are distinctly visible, separated by their surface ligands. (b) Measurement of film thickness for the multilayered CQW constructs having different numbers of layers. The linear fit confirms 7.0 nm of thickness per deposited CQW layer. (b) Surface roughness measurements of multilayer CQW films on fused silica taken with atomic force microscopy imaging over 5 different regions having an area of 2×2 μm^2. Dashed line shows the roughness of the bare fused silica subtrate (∼0.2 nm). Adapted from Ref. [131].

Ellipsometric measurements on the thickness of multilayered CQW films having different numbers of layers verify the linear trend between the film thickness and the number of CQW layers as seen in Figure 3.8b. We extracted from the linear fitting of the experimental data that each deposited CQW

monolayer adds up 7.0 nm to the film thickness. Since the thickness of the core/shell CQW structure is 4.1 nm, the ligand brush between the CQW layers is deduced to be 2.9 nm thick, indicating a minor inderdigitation between the ligand brushes of oleic acid/oleylamine. This interdigitation might help the CQWs stick together stronger *via* van der Waals interaction between the ligand molecules of CQWs in successive layers. One advantage of this technique is therefore that deposition of oppositely charged linker molecules between the monolayers, which is commonly employed for layer-by-layer NC deposition [22, 27, 133, 138], is not needed here. Not having to rely on the deposition of oppositely charged particles adds up to the versatility of our multilayered deposition technique as the thickness of such constructs built of oppositely charged bilayers might be altered by ambient conditions [139] or by unintentional diffusion of charged particles into the previously deposited inner layers during dipping steps, which leads to superlinear thickness growth [140]. Our self-assembly method thus presents a robust approach alternative to the existing methods of NC self-assembly at liquid interface [25,83,132], while maintaining large-area uniformity and precision in film thickness.

This self-assembly technique equips us with the ability to deposit CdSe/CdZnS core/shell CQWs in desired thickness as a continuous, uniform film with over areas as large as 80 cm^2. Enabling precise control of the film thickness, this approach can find use in large-scale device engineering and fabrication in optoelectronics. Our approach can in principle be used to control the CQW orientation in each individual layer, adding an extra degree of freedom to create new possibilities in constructing CQW superstructures. These films that we constructed here have been demonstrated to act as optically active waveguides, whose optical gain performances were studied and characterized depending on their thicknesses. The results of this study will be presented in Chapter 5.

3.3 Summary and Discussion

In this chapter, we demonstrated two different approaches that utilize liquid-air interface self-assembly technique to deposit uniform, orientation-controlled films of CQW over large areas. In the former, CdSe core CQWs were deposited as a single layer, in a single desired orientation (all face-down or all edge-up) of our choice. The orientation control was achieved using different subphases (ACN for face-down and EG for edge-up), while the near-unity surface coverage across cm^2 large areas was managed thanks to the compression of the membrane on the liquid-air interface with silicone oil.

In the latter approach, we deposited CdSe/CdZnS core/shell CQWs sequentially, one monolayer at a time, while controlling the orientation of CQWs (all face-down only). The sequential deposition of CQW monolayers enabled precise control on the film thickness while preserving the excellent film homogeneity and keeping the roughness of the film surface to a minimum. Similar to the former approach, we made use of silicone oil to obtain a tightly-packed CQW film. The differences of this multilayer deposition technique with the former approach include the use of a different subphase (DEG), silane-treatment of the substrates prior to deposition, and tilting of the substrates (by about 10°). The last two of these changes ensure the subphase slides away from the substrates easily while it is being drained, leaving very few droplets on the substrates for evaporation. DEG was found to yield the most uniform films of CdSe/CdZnS CQWs, given that these CQWs are properly precipitated beforehand. The other subphases studied (ACN, EG and water) have led to unintentional lamellar or columnar stacking in a single deposition.

It should be noted that the former approach could not be extended to build face-down multilayers of core CQWs since prolonged exposure of the deposited CQW films to ACN led to the deposited films being partially ripped off, as well as to strong quenching in the emission of the CQWs remaining on the substrate. Furthermore, the latter approach, through which we could deposit multilayered CdSe/CdZnS CQW films with excellent homogeneity, is not directly

applicable to the core-only CQWs because DEG, which results in face-down deposition of core/shell CQWs that we used, resulted in a mixed CQW orientation or occasionally, a fully edge-up ensemble. Similarly, the self-assembly of our CdSe/CdZnS CQWs on EG led to mostly face-down orientation, in contrast to the self-assembly of core CQWs on EG, where the CQWs were all edge-up.

These experimental observations indicate that the interaction of the CQWs with the subphase, and the resulting CQW orientation, might depend on the CQW size. These differences observed with various CQWs might be related to the difference in the interparticle interaction required to bring the CQWs face to face. Paik *et al.* argued that the tendency of hydrophobic ligands to repel the subphase increases with subphase polarity [83]. This is in accordance with our self-assembly experiments, where we observed a stronger tendency for CQW stacking when more polar subphases are used. This tendency holds for both core and core/shell CQWs. However, in the case of our core/shell CQWs, even though the degree of stacking increased with polarity, the ensemble was still only partially stacked even with the most polar subphase used (i.e., water). This might be an indication that the core/shell CQWs we used were too "massive" to stand up and stick to each other, even when the subphase is strongly repellent. In this case, working with CQWs having thinner shells might help achieving better control over the CQW orientation.

Although our results signify an important step in utilization of liquid-air interface self-assembly for controlled CQW film deposition, it is clear from the above discussion that some challenges remain to be addressed. The nonstacked deposition of core CQWs have slight nonuniformities as seen in Figures 3.3a and 3.3c. Furthermore, fully edge-up orientation of the core/shell CQW ensembles, or multilayered deposition of face-down core CQWs have not yet been achieved with our technique, as discussed earlier. These observations imply that additional means to enforce all the CQWs in an ensemble into a particular orientation, such as controlling the evaporation rate [92] or the initial CQW concentration, might be necessary. A combination of the choice of proper subphase, as well as other experimental parameters such as CQW solvent and its evaporation rate might enable full control over the orientation of CQWs of different compositions

and sizes. This can enable deposition CQW multilayers with alternating CQW orientations at each layer, thereby adding the CQW orientation as a degree of freedom in the design and construction of CQW superstructures.

In Chapters 4 and 5, the two- and three-dimensional self-assembled CQW films, whose preparation is explained here, will be next used for the investigation of nonradiative energy transfer and optical gain with CQWs, respectively.

Chapter 4

Orientation-Controlled FRET with Self-Assembled Monolayers of CQWs

This chapter is based on our publication "Orientation-Controlled Nonradiative Energy Transfer to Colloidal Nanoplatelets: Engineering Dipole Orientation Factor" by O. Erdem *et al*, *Nano Letters*, 2019. Adapted with permission from Ref. [28]. Copyright 2019 American Chemical Society.

Förster resonance energy transfer (FRET) is the nonradiative transfer of excitation energy from a donor fluorophore to an acceptor one. FRET is induced by near-field interaction of oscillating dipoles [93, 141]. Although initial studies on FRET focused on fluorescent organic molecules including dyes and proteins, FRET has gained further attraction after the introduction of inorganic colloidal nanocrystals (NCs) [97, 104, 107, 142–146]. Being an extremely distance-sensitive process, FRET involving NCs is used in a variety of applications including light-harvesting [21], optoelectronics [147] and biosensing [148, 149].

Apart from the donor-acceptor distance, the strength of FRET depends on a number of parameters including the spectral overlap of the donor and acceptor

and the radiative emission rate of the donor as well as the relative orientation factor of donor and acceptor dipoles. The last parameter, commonly denoted as κ^2, is especially important when either the donor or acceptor fluorophore has an anisotropic dipole state. In the case that the dipole states of both fluorophores rotate freely in three dimensions in an ensemble, the average of κ^2, which is denoted as $\langle\kappa^2\rangle$, equals 2/3, as discussed in Section 2.3 [93]. However, for dipoles confined along one or two dimensions, or whose rotation is limited by any other means, this factor is expected to be different [95]. Therefore, if the orientation of all of the anisotropic donor or acceptor species in an ensemble is controlled, the strength of FRET in semiconductor NC ensembles can in principle be modified via tuning the average dipole-dipole interaction coefficient, $\langle\kappa^2\rangle$, which would serve as another degree of freedom to control FRET. However, the control of $\langle\kappa^2\rangle$ in a FRET system of NCs over macroscopic areas has remained elusive to date.

In this thesis work, to control the dipole interaction and investigate its effect on FRET, we employed quantum dots as donors, whose dipoles are isotropic, together with colloidal quantum wells (CQWs) as acceptors, which have quasi two-dimensional (2D) dipoles confined within the CQW plane. Having atomically flat surfaces, a vertical thickness of only a few nm and lateral dimensions of several nm's to several tens of nm's, CQWs feature intrinsic anisotropy, because of which their transition dipole state near the band edge is almost fully confined within the CQW plane [15]. Furthermore, unlike other 2D materials such as epitaxially grown quantum wells and transition metal dichalcogenides, the processability of CQWs in solution enables control of their in-film orientation. This feature of CQWs, along with their unusually large extinction coefficient [12, 17, 129], makes them attractive materials as FRET acceptors with the capability of dipole interaction control. However, the role and effect of different CQW orientations on the strength and distance-dependence of FRET are yet to be revealed.

In this study, we created 2D arrays of CQWs in a desired orientation to investigate the dependence of FRET from isotropic QD donors to anisotropic CQW acceptors on the CQW orientation. For this purpose, we utilized the liquid-air interface self-assembly, through which all face-down or all edge-up CQWs were deposited onto substrates as a single monolayer. Subsequently, the FRET rate

from QDs to CQWs was measured as a function of both the CQW orientation and the distance between QDs and CQWs. Our results show that the FRET rate from QDs to CQWs is enhanced in the case of using edge-up CQWs, due to the increased CQW packing density, as well as the enhanced dipole alignment factor. Furthermore, our systematic studies on the distance (d) dependence of FRET from QDs to orientation-controlled CQW monolayers revealed that the FRET rate exhibits a d^{-4}-dependence, as would be expected for a plane of acceptors [97]. To calculate the FRET rate in the cases of face-down *vs.* edge-up CQWs acceptors, we employed Förster's original theory of nonradiative energy transfer. In doing so, we took into account the delocalization of the excitonic state in CQWs, as well as the average dipole orientation factor $\langle\kappa^2\rangle$ being a function of both the position and orientation of the acceptor dipole. Our computations in both cases show excellent agreement with the FRET rates extracted from our experiments. This work demonstrates the large-area control of CQW orientation for the first time, and its use for tuning the strength of energy transfer by changing the alignment of the acceptor dipole.

4.1 Experimental Observation of Orientation-Controlled FRET to CQWs

For the study of orientation-controlled FRET, CdSe CQWs having 4.5 ML of atomic thickness and monodisperse CdZnS/ZnS QDs were synthesized with recipes based on previous reports [7,14]. We used liquid-air interface self-assembly technique for depositing one monolayer of CQWs in a single desired orientation onto silicon substrates, which were predeposited with 25 nm of Al_2O_3 via atomic layer deposition (ALD). The details of the self-assembled deposition of CQWs are given in Section 3.1. A set of substrates, such as those shown in the photo of Figure 3.2a, were deposited with a monolayer of CQWs that are all face-down, and another set was deposited with a monolayer of edge-up CQWs. The monolayer of CQWs, which has been deposited without the assistance of silicone oil, displays good uniformity throughout the substrates. The surface coverage in these films

is near-unity across domains that are at least a few mm^2 (see Figure 3.3), which is sufficiently large for ensemble optical measurements.

In order to study how the orientation of the CQWs affects their excitonic properties, we employed these self-assembled CQWs as acceptors in an energy transfer model system, pairing with blue-emitting QDs as donor with the monolayer of CQWs as the acceptor. Specifically, our hypothesis is that the FRET rate from isotropic QDs to anisotropic CQWs should be modified with the orientation of the CQWs due to the changing dipole-dipole coupling strength between a QD-CQW pair for different CQW orientations. To test this hypothesis, blue-emitting QDs dispersed in toluene were spin-coated directly onto the self-assembled CQW films. The SEM images of the QD films deposited on face-down and edge-up CQW monolayers are displayed in Figures 4.1a and 4.1b, respectively. QDs are seen to be reasonably sparse and have sub-monolayer coverage on top of the CQW monolayer, which ensures that all of the deposited QDs are equally distant to the CQW plane, and hence are coupled to the CQW film to the same extent. This is essential for proper characterization of FRET in our case, otherwise since with a QD film thicker than one monolayer, some of the QDs would remain slightly further away to the CQWs, resulting in weaker FRET from these farther QDs.

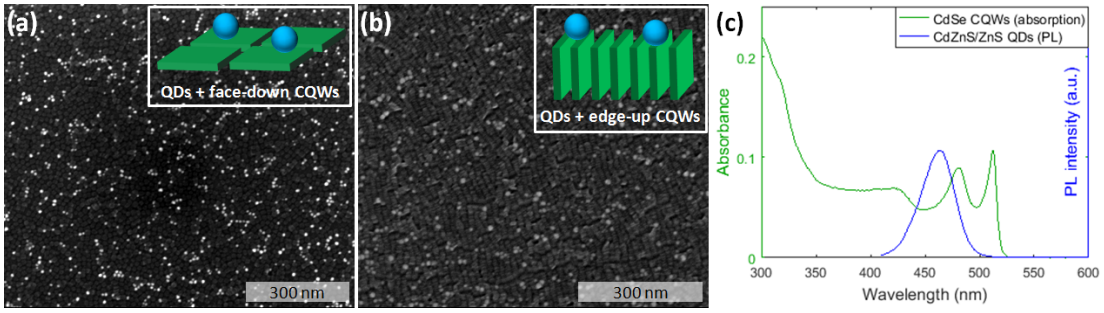

Figure 4.1: SEM images of CdZnS/ZnS QDs on a (a) face-down and (b) edge-up CQW monolayer. (c) Absorbance spectrum of the CQWs (green) and photoluminescence (PL) spectrum of the QDs (blue). Adapted with permission from Ref. [28]. Copyright 2019 American Chemical Society.

The emission spectrum of the donor QDs and absorption spectrum of the acceptor CQWs are plotted in Figure 4.1c. The overlap between these two

spectra shows that FRET from QDs to CQWs is possible when they are in close proximity. In order to calculate the rate of the energy transfer, we collected the photoluminescence (PL) decays of the QDs when deposited on top of the CQW monolayers, as well as with no acceptor CQWs in place, using a time-resolved spectrometer system, pictured in Figure 4.2a. The excitation laser has a wavelength of 375 nm, a pulse width of ∼200 ps and a repetition rate of 2.5 MHz. The excitation was focused onto a spot of ∼100 µm size on the sample. The collection wavelength was set to 460 nm, which is the spectral emission peak of the QDs. The collected PL decays of the QDs alone, QDs on top of the face-down CQWs and the QDs on top of the edge-up CQWs are shown in Figure 4.2b. These data were fit to multiexponential decays convolved with the instrument response function:

$$I(t) = \left(\sum_i A_i e^{-t/\tau_i} \right) * IRF(t) \tag{4.1}$$

where A_i and τ_i are the amplitude and lifetime of the i^{th} decay component, respectively, and $IRF(t)$ is the instrument response function. All the three decays were best with four exponential components. In the case of such a multiexponential decay, it is convenient to use the amplitude-averaged lifetime in FRET-related calculations [150], which is given as

$$\tau_{avg} = \frac{\sum_i A_i \tau_i}{\sum_i A_i} \tag{4.2}$$

The amplitude averaged lifetime of the QDs alone, QDs on top of a monolayer of face-down CQWs and QDs on top of a monolayer of edge-up CQWs is 4.72, 1.08 and 0.79 ns, respectively. The decay time of the donor QDs in the presence of acceptors is modified according to Equation 2.23:

$$\frac{1}{\tau_{DA}} = \frac{1}{\tau_D} + k_T \tag{4.3}$$

where τ_D (τ_{DA}) is the PL lifetime of donor QDs in the absence (presence) of the acceptor CQWs and k_T is the rate of FRET from the donor to the acceptor. In our case, $\tau_D = 4.72$ ns, and $\tau_{DA} = 1.08$ ns (0.79 ns) when the QDs are on top of face-down (edge-up) CQWs. Therefore, from the experimental data, these lifetimes yield the FRET rate k_T to be 0.71 ns^{-1} from QDs to face-down CQWs and 1.05

ns^{-1} to edge-up CQWs. Hence, the rate of FRET is accelerated by ∼50% when the orientation of the CQWs change from face-down to edge-up (Figure 4.2c). Since the domain sizes in the self-assembled CQW films are much larger than the spot size of the excitation laser (∼100 µm), we can assert that all the excited QDs are coupled to the nearby CQWs, and that there is no noticeable contribution of uncoupled QDs to the PL decay.

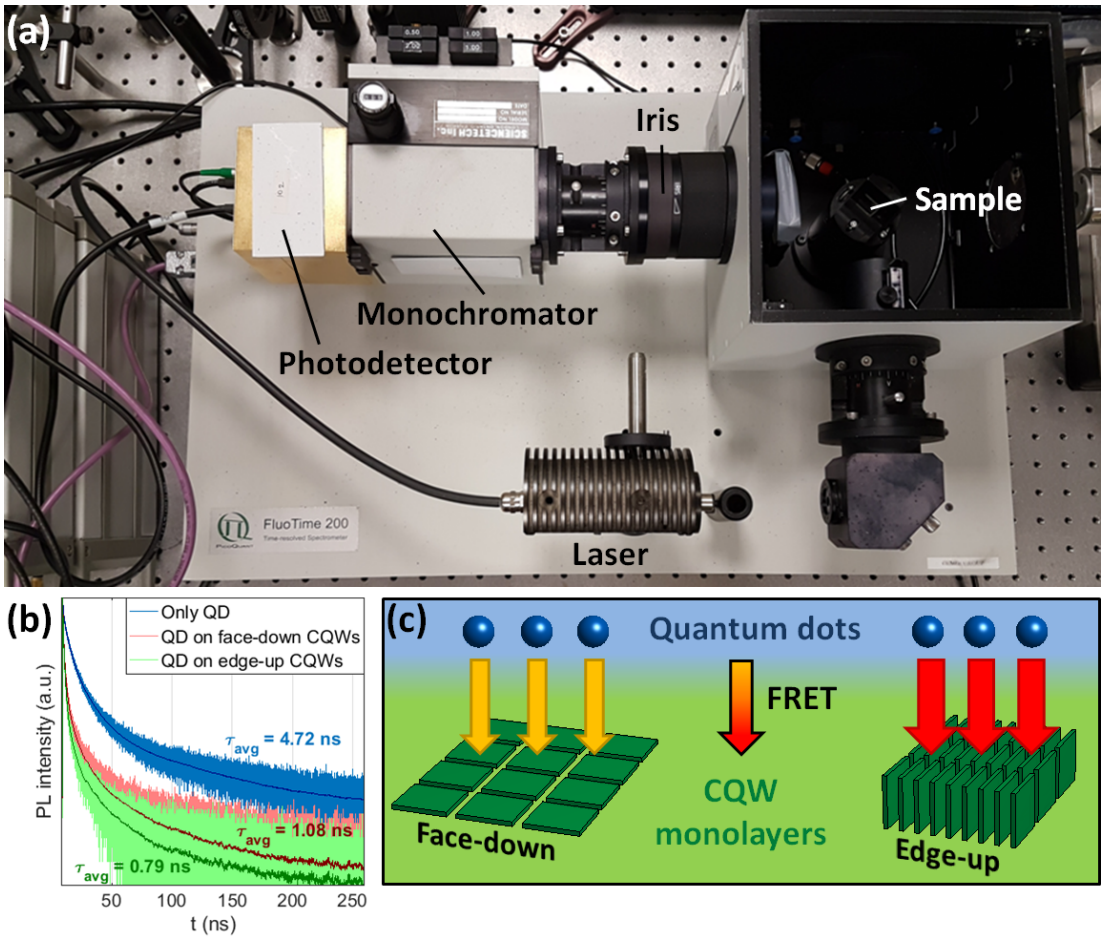

Figure 4.2: (a) Photograph of the time-resolved spectrometer. (b) Photoluminescence decay of the QDs in the absence of CQWs (blue), on top of the face-down CQWs (red) and on top of the edge-up CQWs (green). (c) Schematic demonstration of the enhancement of FRET from QDs to a CQW monolayer in the case of edge-up CQWs. b, c adapted with permission from Ref. [28]. Copyright 2019 American Chemical Society.

For a better understanding of how FRET is affected by the CQW orientation as well as the distance between QDs and CQWs, we also investigated the

strength of FRET by varying the separation of the QDs and the CQW monolayer systematically. For this purpose, we added a spacer of Al_2O_3 *via* ALD, whose film thickness was swept from 1 to 15 nm, between the QDs and the self-assembled CQW monolayer. The overall structure is schematically depicted in Figures 4.3a and 4.3b for QDs over face-down and edge-up CQWs, respectively. There is also a 25 nm thick Al_2O_3 film between the CQW monolayer and the substrate, which is deposited to prevent the energy transfer from the QDs to the silicon [111,112,151]. The CQWs on top of this bottom Al_2O_3 layer were deposited via our self-assembly procedure described in Section 3.1. After the spacer Al_2O_3 was deposited, a diluted solution of QDs was spin-coated onto the substrates.

The PL decays are presented in Figures 4.3c and 4.3d for the QDs over the face-down and edge-up CQW monolayer, respectively. The decays of the QD films without any spacer, displayed in Figure 4.2b, are also added here, labeled as "0 nm Al_2O_3" in the legend. It can be seen that as the spacer thickness decreases, the decays are progressively accelerated, indicating FRET growing increasingly stronger. Similar to the PL decays of QDs in the no spacer case, the decays here were also fit well with four exponentials. The best fit parameters are given in Tables 4.1 and 4.2 for the films with face-down and edge-up CQWs, respectively, along with the amplitude-averaged lifetimes calculated using Equation 4.2. These average decay times of the QDs are plotted as a function of the spacer thickness in Figure 4.3e. Here, the decay lifetimes of QDs on top of CQWs are observed to converge to that of the QD only case with increasing spacer thickness, as expected. The corresponding rates of FRET, calculated using Equation 2.24, are presented in Figure 4.3f. For all the spacer thicknesses, FRET is stronger in the case of using edge-up CQWs.

Finally, Figure 4.3g shows the efficiency of FRET from the QDs to the face-down and edge-up CQWs. In the general case, the FRET efficiency is given by

$$\eta = \frac{1}{1 + (d/d_0)^p} \tag{4.4}$$

where d is the distance from the center of the QD to the top surface of the CQW monolayer, d_0 is the Förster distance, at which the efficiency is 50%, and p is the

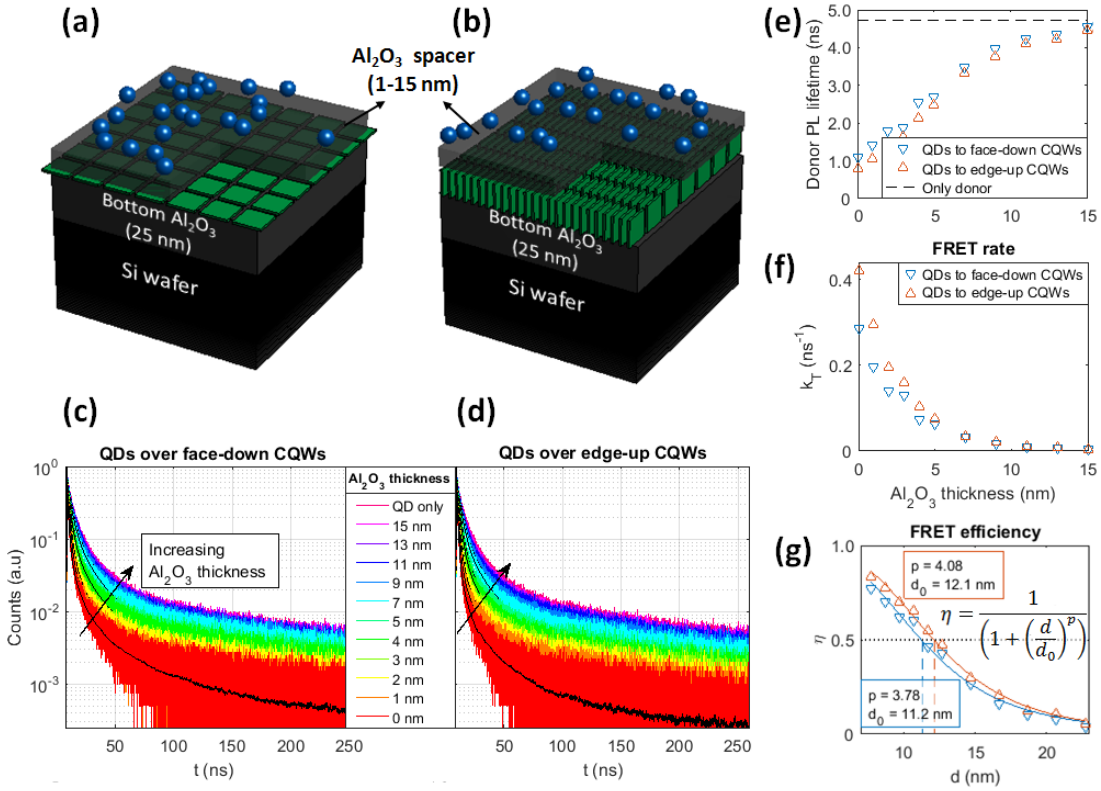

Figure 4.3: Overall structure of the FRET working model system between donor QDs and acceptor CQW monolayer for (a) face-down and (b) edge-up CQWs. PL decays of QDs over (c) face-down (nonstacked) and (d) edge-up (stacked) CQWs. The black curves are fits to multiexponential decays convolved with the instrument response function. (e) Average decay lifetimes of QDs and (f) extracted rates of FRET to the face-down (blue down triangles) and edge-up CQWs (orange up triangles). (g) FRET efficiencies as a function of the donor-acceptor distance along with their numerical fits to the FRET efficiency formula in the inset (Equation 4.4). The data captures the d^{-4} behaviour for both CQW orientations. The vertical dashed lines indicate the Förster distances for FRET to the face-down (blue) and edge-up (orange) CQW monolayers. Adapted with permission from Ref. [28]. Copyright 2019 American Chemical Society.

Table 4.1: Multiexponential fitting parameters for PL decays of QDs over face-down CQWs. PL decay of only QDs are also added for reference. Reprinted with permission from Ref. [28]. Copyright 2019 American Chemical Society.

	A_1	τ_1 (ns)	A_2	τ_2 (ns)	A_3	τ_3 (ns)	A_4	τ_4 (ns)	$\boldsymbol{\tau_{avg}}$ **(ns)**
Only QD	134	56.9	969	11.4	1898	3.71	2690	0.424	**4.72**
15 nm spacer	137	54.9	1085	10.4	1912	3.31	2637	0.387	**4.53**
13 nm spacer	143	52.5	1152	9.84	1844	3.07	2707	0.367	**4.36**
11 nm spacer	117	55,6	923	10.7	2062	3.43	2678	0.388	**4.24**
9 nm spacer	116	54.0	899	10.2	1974	3.22	2788	0.381	**3.96**
7 nm spacer	104	52.9	792	9.88	2131	3.01	2999	0.368	**3.46**
5 nm spacer	75.5	51.8	574	9.17	2261	2.65	3133	0.368	**2.70**
4 nm spacer	69.4	49.8	541	9.01	2330	2.42	2979	0.385	**2.55**
3 nm spacer	47.4	46.5	371	8.09	2543	2.07	3216	0.368	**1.89**
2 nm spacer	47.1	44.5	365	7.84	2426	1.97	3267	0.365	**1.79**
1 nm spacer	42.6	39.1	332	6.74	2426	1.64	3629	0.351	**1.42**
No spacer	38.5	37.1	256	6.84	1552	1.47	4877	0.369	**1.08**

Table 4.2: Multiexponential fitting parameters for PL decays of QDs over edge-up CQWs. PL decay of only QDs are also added for reference. Reprinted with permission from Ref. [28]. Copyright 2019 American Chemical Society.

	A_1	τ_1 (ns)	A_2	τ_2 (ns)	A_3	τ_3 (ns)	A_4	τ_4 (ns)	$\boldsymbol{\tau_{avg}}$ **(ns)**
Only QD	134	56.9	969	11.4	1898	3.71	2690	0.424	**4.72**
15 nm spacer	120	56.9	911	11.1	2028	3.59	2615	0.419	**4.46**
13 nm spacer	116	55.9	920	10.7	2033	3.41	2684	0.388	**4.22**
11 nm spacer	106	56.1	827	10.8	2126	3.45	2601	0.416	**4.12**
9 nm spacer	96.4	54.5	744	10.4	2239	3.30	2652	0.414	**3.75**
7 nm spacer	79.5	55.0	611	10.2	2384	3.10	2687	0.416	**3.32**
5 nm spacer	57.5	51.5	437	9.31	2475	2.56	2903	0.413	**2.48**
4 nm spacer	50.6	48.6	384	8.67	2500	2.29	3043	0.397	**2.13**
3 nm spacer	43.0	43.5	330	7.50	2497	1.81	3325	0.365	**1.63**
2 nm spacer	42.3	38.5	338	6.71	2413	1.58	3457	0.345	**1.42**
1 nm spacer	37.1	34.6	290	5.86	2498	1.27	4121	0.276	**1.05**
No spacer	28.8	30.4	231	5.08	2481	1.04	4535	0.252	**0.79**

exponent indicating the dependence of the FRET on the distance. As discussed in Section 2.3, p is 6 for a pair of point-like donor and acceptor, and it is lower for higher acceptor dimensionalities. Using Equations 2.15 and 2.24, it can be shown that the experimentally measured decay time of the donor in the absence and presence of the acceptor can be used to calculate the FRET efficiency as

$$\eta = 1 - \frac{\tau_{DA}}{\tau_D} \tag{4.5}$$

The experimental FRET efficiencies calculated with Equation 4.5 are plotted in Figure 4.3g and fitted to Equation 4.4 to estimate the Förster distance as well as the distance dependence of FRET. Here, the distance d is defined as that between the center of the QD and the top surface of the CQW monolayer. For the monolayer of face-down CQWs, the best fit parameters are found as $d_0 =$ 11.2 nm and $p = 3.78$, whereas for the edge-up CQW monolayer they are $d_0 =$ 12.1 nm and $p = 4.08$. It can therefore be seen that the distance dependence in both cases is close to d^{-4}, as expected for FRET to 2D materials [96, 152, 153] or to a plane of acceptors [97, 154].

4.2 Theoretical Modeling of Orientation-Controlled FRET to CQWs

To account for the difference in the rate of FRET to the nonstacked (face-down) and stacked (edge-up) CQW monolayers, we make use of Förster's theory of nonradiative energy transfer. Accordingly, the rate of energy transfer from a donor to an acceptor is given by Equation 2.13:

$$k_T = \frac{\langle \kappa^2 \rangle QY}{R^6 \tau} \frac{9 \ln 10}{128 \pi^5 N n^4} J \tag{4.6}$$

where QY is the PL quantum yield of the donor species in the absence of acceptors, R is the distance between the donor and acceptor, N is the Avogadro's number, n is the refractive index of the medium and J is the spectral overlap between the emission of the donor and and the absorbance of the acceptor, given

by Equation 2.11. The in-film QY of our QDs were measured to be 65%, and n = 1.72 is used as the refractive index of the medium.

Equation 4.6 applies to an ensemble of point-like donor-acceptor pairs with a fixed separation in between them. In our case, however, the acceptor CQWs are planar rather than point-like and the donor QDs are coupled to multiple acceptors. Furthermore, R and $\langle\kappa^2\rangle$ are also different for each CQW on a 2D array. The variation of donor-acceptor distance for different CQWs is evident in Figure 4.4. Understanding how $\langle\kappa^2\rangle$ changes with the location and orientation of a CQW, on the other hand, requires a more thorough investigation on dipole pairs visualised in Figures 4.4a and 4.4b. For donor and acceptor dipoles $\vec{\mu}_d$ and $\vec{\mu}_a$ and the distance vector $\vec{R}$ from one to the other, the dipole orientation factor is given by [94]

$$\kappa^2 = (\cos(\alpha_{da}) - 3\cos(\alpha_{dR})\cos(\alpha_{aR}))^2 \tag{4.7}$$

where α_{da} is the angle between the donor and acceptor dipoles, α_{dR} is the angle between the donor dipole and the distance vector and α_{dR} is the angle between the donor dipole and the distance vector, with $\cos(\alpha_{da}) = \hat{\mu_d}\cdot\hat{\mu_a}$, $\cos(\alpha_{dR}) = \hat{\mu_d}\cdot\hat{R}$ and $\cos(\alpha_{aR}) = \hat{\mu_a}\cdot\hat{R}$. For randomly oriented dipoles, κ^2 should be averaged over different dipole orientations.

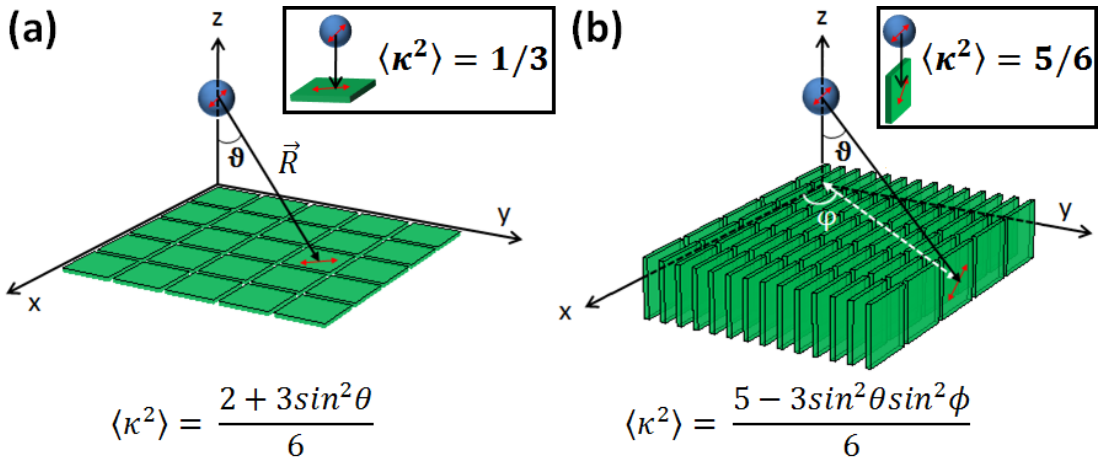

Figure 4.4: Average dipole orientation coefficient $\langle\kappa^2\rangle$ of a QD and a CQW when the CQWs are (a) face-down and (b) edge-up. Insets show that for the face-down CQW that is closest to the QD, (i.e. $\theta = 0$), $\langle\kappa^2\rangle$ becomes 1/3. For $\theta = 0$ in the edge-up array, $\langle\kappa^2\rangle$ is 5/6. Adapted with permission from Ref. [28]. Copyright 2019 American Chemical Society.

To calculate the average of κ^2, we begin by noting that the QD dipole freely rotates in 3D, while the CQW dipole is assumed to be fully confined within the CQW plane [15]. For a QD dipole that is freely rotating in 3D, the unit vector of the dipole moment is given by Equation 2.6:

$$\hat{\mu}_d = \sin(\theta_d)\cos(\phi_d)\hat{x} + \sin(\theta_d)\sin(\phi_d)\hat{y} + \cos(\theta_d)\hat{z} \tag{4.8}$$

where θ_d and ϕ_d are the polar and azimuthal angles, respectively. The probability density function for these angles is

$$f(\theta_d, \phi_d) = \frac{1}{4\pi}\sin(\theta_d) \tag{4.9}$$

with $0 \leq \theta_d \leq \pi$ and $0 \leq \phi_d \leq 2\pi$.

Using the configuration in Figure 4.4a, the CQW dipole confined within the CQW plane will have a unit vector

$$\hat{\mu}_a = \cos(\phi_a)\hat{x} + \sin(\phi_a)\hat{y} \tag{4.10}$$

where ϕ_a has a uniform probability density from 0 to 2π:

$$f(\phi_a) = \frac{1}{2\pi}, 0 \leq \phi_a \leq 2\pi \tag{4.11}$$

Rotating the coordinate axes such that the z-axis is aligned with $\vec{R}$ slightly simplifies the calculations that will follow. With the rotated axes,

$$\hat{\mu}_a = \cos(\phi_a)\hat{x} + \cos\theta\sin(\theta_a)\hat{y}' - \sin\theta\sin(\phi_a)\hat{z}' \tag{4.12}$$

where $\hat{y}' = \cos\theta\hat{y} + \sin\theta\hat{z}$ and $\hat{z}' = \hat{R} = -\sin\theta\hat{y}' + \cos\theta\hat{z}$. At this point, we can also redefine the angles θ_d and ϕ_d such that they now represent the polar and azimuthal angles with respect to the new coordinate system, i.e.,

$$\hat{\mu}_d = \sin(\theta_d)\cos(\phi_d)\hat{x} + \sin(\theta_d)\sin(\phi_d)\hat{y}' + \cos(\theta_d)\hat{z}' \tag{4.13}$$

We therefore have

$$\begin{aligned}
\cos(\alpha_{da}) = \hat{\mu}_d \cdot \hat{\mu}_a &= \sin(\theta_d)\cos(\phi_d)\cos(\phi_a) + \cos\theta\sin(\theta_d)\sin(\phi_d)\sin(\phi_a) \\
&\quad - \sin\theta\cos(\theta_d)\sin(\phi_a) \\
\cos(\alpha_{dR}) = \hat{\mu}_d \cdot \hat{z}' &= \cos(\theta_d) \\
\cos(\alpha_{aR}) = \hat{\mu}_a \cdot \hat{z}' &= -\sin\theta\sin(\phi_a)
\end{aligned} \tag{4.14}$$

Using Equations 4.7 and 4.14, we obtain

$$\begin{aligned}\kappa^2 = &\sin(\theta_d)\cos(\phi_d)\cos(\phi_a) + \cos\theta\sin(\theta_d)\sin(\phi_d)\sin(\phi_a) \\ &+ 2\sin\theta\cos(\theta_d)\sin(\phi_a)\end{aligned} \tag{4.15}$$

The average of κ^2 can then be calculated by evaluating

$$\langle\kappa^2\rangle = \iiint \kappa^2 f(\theta_d, \phi_d) f(\phi_a) d\theta_d d\phi_d d\phi_a \tag{4.16}$$

Inserting expressions from Equations 4.9, 4.11 and 4.15 into Equation 4.16:

$$\begin{aligned}\langle\kappa^2\rangle = \int_0^{2\pi}\int_0^{2\pi}\int_0^{\pi} &(\sin(\theta_d)\cos(\phi_d)\cos(\phi_a) + \cos\theta\sin(\theta_d)sin(\phi_d)sin(\phi_a) \\ &+ 2\sin\theta\cos(\theta_d)\sin(\phi_a))^2 \frac{1}{8\pi^2}\sin(\theta_d) d\theta_d d\phi_d d\phi_a\end{aligned} \tag{4.17}$$

which, after evaluation, yields

$$\langle\kappa^2\rangle = \frac{2 + 3\cos^2\theta}{6} \tag{4.18}$$

Equation 4.18 therefore gives us the average dipole-dipole orientation coefficient for a QD dipole randomly oriented in 3D and the dipole of a face-down CQW confined within the CQW plane, depending on the position of the dipole, i.e., θ (see Figure 4.4a)

To calculate $\langle\kappa^2\rangle$ for an edge-up CQW array, we use the configuration in Figure 4.4b. Here, the coordinate axes are chosen such that the CQW chains are along the y-axis. In this case, the unit vector of the acceptor dipole is

$$\hat{\mu}_a = \cos(\theta_a)\hat{x} + \sin(\theta_a)\hat{z} \tag{4.19}$$

where θ_a has the probability density function

$$f(\theta_a) = \frac{1}{2\pi}, 0 \leq \theta_a \leq 2\pi \tag{4.20}$$

To align $\vec{R}$ with the z-axis again, we have to make two coordinate transformations: We first rotate the coordinate axes by ϕ around the z-axis to create (x'y'z) coordinate system. Then we rotate the new coordinate axes by θ around the

y'-axis and end up with the (x"y"z") coordinate system. The transformation matrix that corresponds to these two variations is

$$\overline{\overline{T}} = \begin{bmatrix} \cos\theta\cos\phi & \cos\theta\sin\phi & \sin\theta \\ -\sin\phi & \cos\phi & 0 \\ -\sin\theta\cos\phi & -\sin\theta\sin\phi & \cos\theta \end{bmatrix} \tag{4.21}$$

Accordingly,

$$\begin{aligned} \hat{\mu}_a = {} & (\cos\theta\cos\phi\cos(\theta_a) + \sin\theta\sin(\theta_a))\hat{x}'' - \sin\phi\cos(\theta_a)\hat{y}'' \\ & + (\cos\theta\sin(\theta_a) - \sin\theta\cos\phi\cos(\theta_a))\hat{z}'' \end{aligned} \tag{4.22}$$

with $\hat{i} = \overline{\overline{T}}\hat{i}''$, where i = x, y or z, and $\hat{R} = \hat{z}''$. Similar to the face-down CQW case, we redefine θ_d and ϕ_d such that

$$\hat{\mu}_d = \sin(\theta_d)\cos(\phi_d)\hat{x}'' + \sin(\theta_d)\sin(\phi_d)\hat{y}'' + \cos(\theta_d)\hat{z}'' \tag{4.23}$$

Putting the expressions for $\hat{\mu}_d$ from Equation 4.23 and $\hat{\mu}_a$ from Equation 4.22 into Equation 4.7 leads to

$$\begin{aligned} \kappa^2 = {} & (\cos\theta\cos\phi\cos(\theta_a)\sin(\theta_d)\cos(\phi_d) + \sin\theta\sin(\theta_a)\sin(\theta_d)\cos(\phi_d) \\ & - \sin\phi\cos(\theta_a)\sin(\theta_d)\sin(\phi_d) + 2\sin\theta\cos\phi\cos(\theta_d)\cos(\theta_a) \\ & - 2\cos\theta\sin(\theta_a)\cos(\theta_d))^2 \end{aligned} \tag{4.24}$$

which, when inserted into Equation 4.16 together with Equations 4.9 and 4.20, yields

$$\langle\kappa^2\rangle = \frac{5 - 3\cos^2\theta\sin^2\phi}{6} \tag{4.25}$$

We see that $\langle\kappa^2\rangle$ depends not only on the location of the CQWs in the array, given by θ, but also the direction of the CQW alignment, given by ϕ (see Figure 4.4b).

Equations 4.18 and 4.25 reveal that the dipole alignment factor of a QD and a CQW changes significantly with CQW orientation. Although we were able to derive the generic formulas that are valid across the whole acceptor plane, the value of $\langle\kappa^2\rangle$ is of most significant interest only for the CQWs that are in close proximity of the donor QD because the dipole-dipole coupling strength (i.e., FRET) will quickly diminish far away from the QD, regardless of the dipole-dipole alignment. In the case of face-down orientation, Equation 4.18 reveals that for

a CQW dipole right below the QD dipole, i.e. at $\theta = 0$, $\langle\kappa^2\rangle$ will be 1/3. On the other hand, Equation 4.25 indicates that for the edge-up case, a CQW dipole located at $\theta = 0$ will have $\langle\kappa^2\rangle = 5/6$. We therefore see the dipole alignment factor between a QD and the nearby CQWs is significantly enhanced in the case of edge-up orientation, which is in agreement with the experimental observation of stronger FRET to edge-up CQW monolayer than to the face-down one.

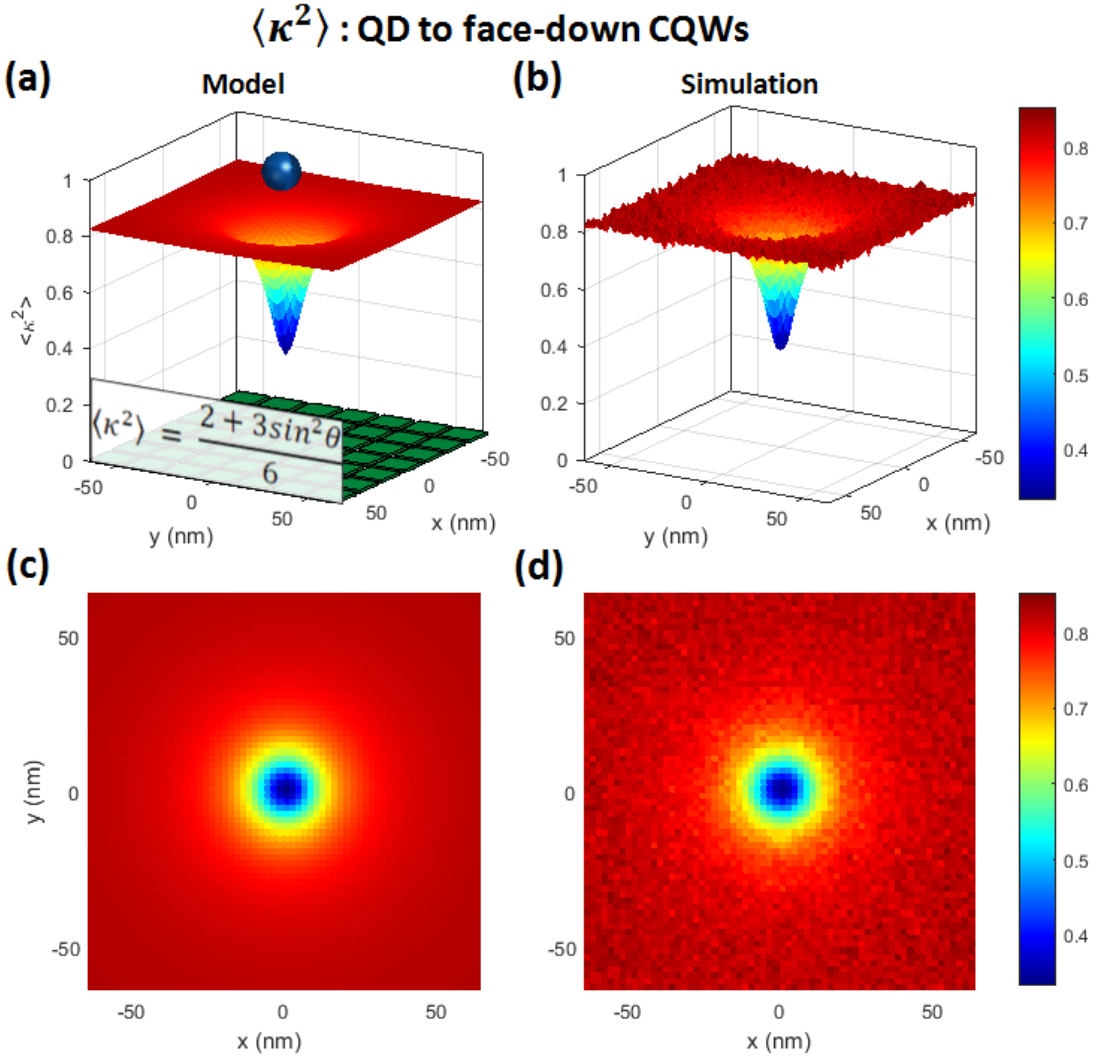

Figure 4.5: Variation of the average dipole-dipole orientation factor $\langle\kappa^2\rangle$ as a function of the coordinates of the dipole of a face-down CQW (a) calculated by the formula (Equation 4.18) and (b) estimated by the Monte-Carlo simulations. The QD and the CQWs are drawn out of scale for clarity purposes. (c), (d) Top-view of the surfaces in (a), (b), respectively.

To further verify the validity of Equations 4.18 and 4.25, we compare the values of $\langle\kappa^2\rangle$ at different coordinates on the acceptor plane calculated using these formulas to those estimated *via* Monte-Carlo simulations. In these simulations, randomly oriented point dipoles were generated and κ^2 is calculated using Equation 4.7 for this pair of dipoles at each repetition. $\langle\kappa^2\rangle$ is estimated by averaging the calculated values of κ^2 in 8,000 repetitions. The random orientation of the acceptor dipoles are constrained to within the CQW plane, according to the configurations in Figure 4.4, i.e., Equations 4.10 and 4.11 for the face-down orientation and Equations 4.19 and 4.20 for the edge-up orientation. Figures 4.5 and 4.6 depict this comparison for 2D arrays of the face-down and edge-up CQWs, respectively. The agreement between the formula and the Monte-Carlo simulations is evident in both cases.

Having addressed the variation of $\langle\kappa^2\rangle$ for both orientations, we move on to accounting for the variation of distance between a QD and the CQWs in the 2D array. As discussed earlier in calculation of the FRET rate, Equation 4.6 holds for point-like donor and acceptor. It can still be used when the sizes of the donor and acceptor fluorophores are much smaller than their interparticle separation. In this case, the excitation dipole states of these particles can be assumed to be located at their center. In our case, however, although QDs can be approximated as point particles, this approximation cannot be made for the CQWs, whose lateral dimensions are comparable to the separation distances used in this study. Instead, we use an approach similar to the one that has previously been carried out by Shafran *et al.*, who studied FRET from QDs to carbon nanotubes. These authors modeled FRET to a point dipole localized in the carbon nanotube as a stochastic process. Accordingly, the FRET rate to anywhere on the carbon nanotube is calculated as a weighted average [155]. In our model, we approximate the CQWs as infinitesimally thin quantum wells with lateral dimensions much larger than the exciton Bohr radius, in which case the density of states in the CQW available for the energy transfer would be uniformly distributed across the CQW cross-sectional area. Then, the rate of energy transfer to a single CQW is

$$k_{T,CQW} = \frac{1}{A}\iint_{A} k_{T|\vec{r}'}\, dA' \tag{4.26}$$

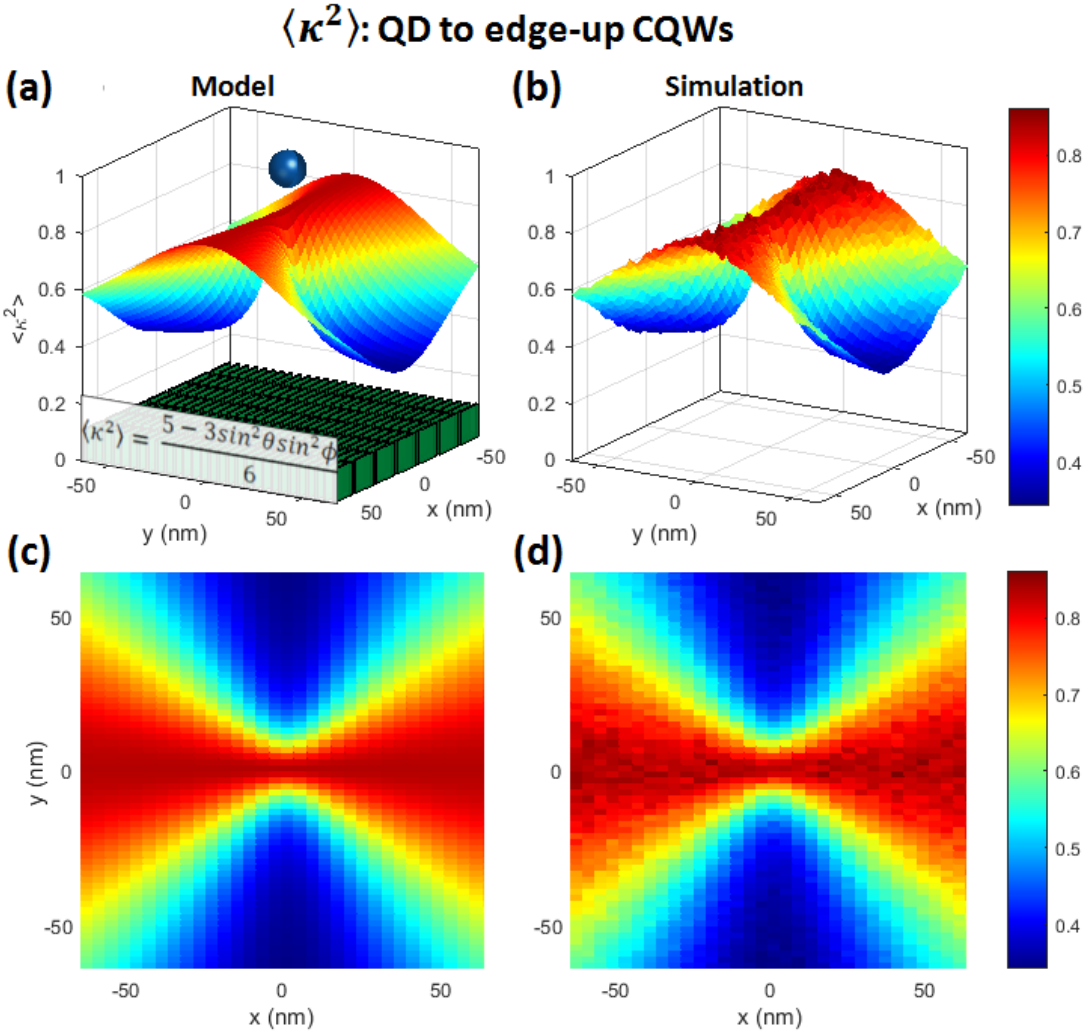

Figure 4.6: Variation of the average dipole-dipole orientation factor $\langle\kappa^2\rangle$ as a function of the coordinates of the dipole of a edge-up CQW (a) calculated by the formula (Equation 4.25) and (b) estimated by the Monte-Carlo simulations. The QD and the CQWs are drawn out of scale for clarity purposes. (c), (d) Top-view of the surfaces in (a), (b), respectively.

where A denotes the area of the CQW and $k_{T|\vec{r}'}$ is the FRET rate for an acceptor dipole localized at $\vec{r}'$ within the CQW, which is calculated using Equation 4.6. The dipole-dipole distance for a particular position $\vec{r}'$ in the CQW is $r = |\vec{R}_0 + \vec{r}'|$, where $\vec{R}_0$ is the center-to-center distance between the donor QD and the acceptor CQW (see Figures 4.7a, b). Similarly, $\langle \kappa^2 \rangle$ will depend on $\vec{r}'$ through Equation 4.18 and Equation 4.25 for the face-down and edge-up CQW monolayers, respectively. For a particular CQW, the integral in Equation 4.26 is taken over the CQW cross-sectional area. The total FRET rate to the CQW monolayer is then found by adding up the FRET rates from a QD to all the CQWs in the 2D array. The FRET rates to the face-down and edge-up CQW monolayers esimated with this approach are plotted in Figures 4.7c and 4.7d, respectively, together with the rates calculated from the lifetime data. In both cases, we observe an excellent agreement between the delocalized dipole approach and the experimental data.

To compare the predictions of this model with those of a conventional center-to-center distance approach, we also plotted the estimated FRET rates assuming the dipole states in the CQW are centered in each CQW (Figures 4.7c and 4.7d; black dots). It is clearly seen that the FRET rates calculated using the centered dipole assumption do not agree with the experiment for small spacer thicknesses. The experimentally measured FRET rates for the nonstacked CQW monolayer are overshot for the face-down case and underestimated for the edge-up one. It is, however, worth noting that, as the donor-acceptor separation increases, the estimations of both models converge to and agree well with the experimental FRET rates. This is the expected behavior since, for large enough separations, the donor and acceptor can be approximated as point dipoles located at the donor and acceptor centers.

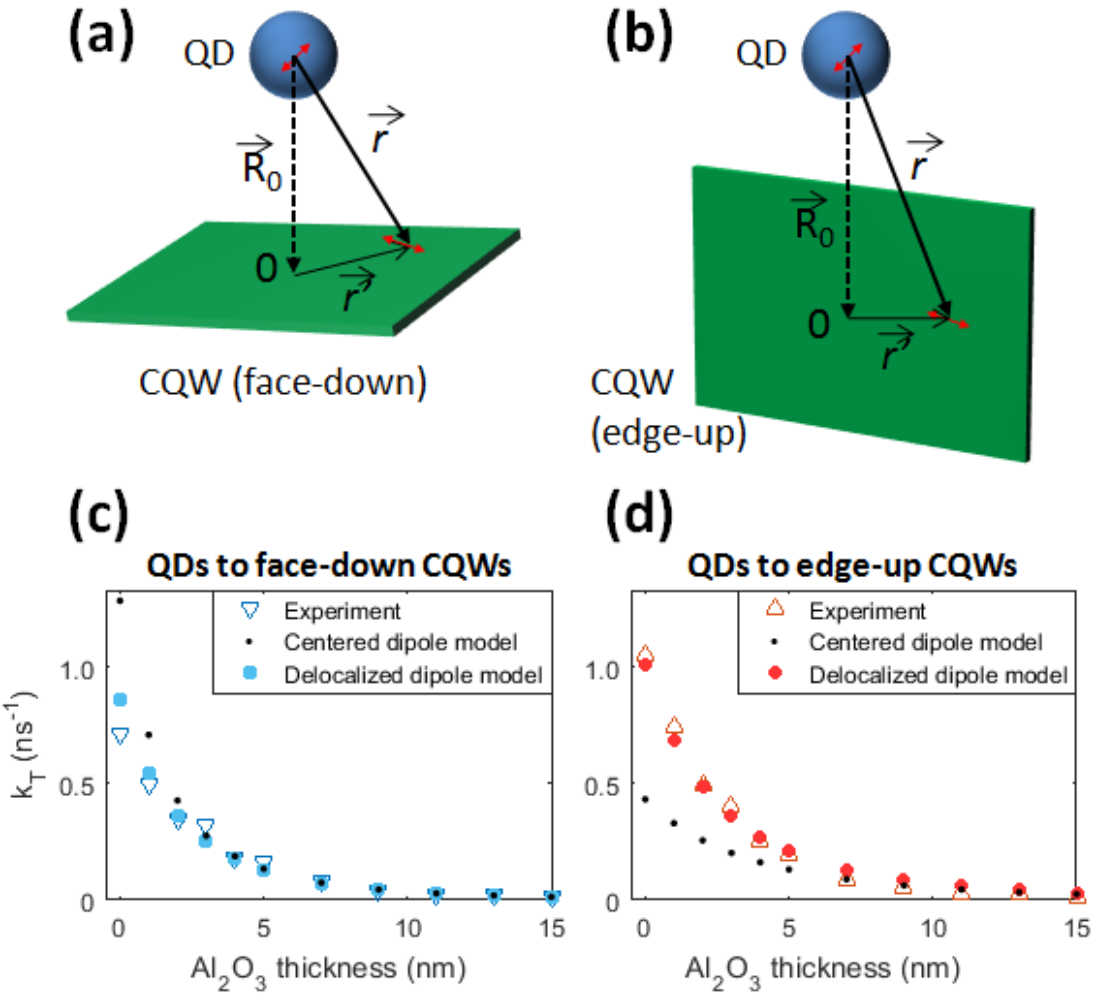

Figure 4.7: Variation of the distance between a QD dipole and a delocalized CQW dipole for (a) face-down and (b) edge-up CQW orientation, depending on the position $\vec{r}'$ of the CQW dipole. (c) Experimental rates of FRET to the face-down CQW monolayer (blue down triangle) compared to those esimated by two different models based on Förster's theory: center-to-center distance approach (small black dots) and delocalized dipole approach (large blue dots). (d) Center-to-center distance approach (black dots) and delocalized dipole approach (large red dots) applied to the edge-up CQW monolayer case to estimate the FRET rates and compare them with the experimentally measured ones. Adapted with permission from Ref. [28]. Copyright 2019 American Chemical Society.

4.3 Accounting for the Purcell Effect in FRET to CQWs

In the previous section, we demonstrated that the acceleration in the decay of the QDs in the proximity of a CQW monolayer can be explained by FRET from QDs to CQWs. This phenomenon can also be interpreted as the enhancement of the nonradiatively dissipated power through near-field interactions, as has been considered previously for metal nanoparticles [156] and semiconductors [157]. In the work of Nguyen *et al.*, the authors employed the normalized power dissipation of a dipole near a stratified medium [158] to find the rate of the total energy transfer into acceptors of silicon slabs. Therein, they showed that the Purcell enhancement of the spontaneous PL decay accounts for the nonradiative as well as radiative energy transfer to the waveguiding modes and the decay into the electromagnetic modes in free space. These results support the idea that the energy transfer could also be explained using Purcell effect.

To elaborate on this idea, here we calculate the Purcell factor F for each of our samples and then estimate the QD lifetimes based on the spontaneous emission rate enhancement due to Purcell effect. Our film structure can be approximated as a stratified medium consisting of a CQW monolayer and thin Al_2O_3 layers on a silicon substrate. We predict the Purcell factor by calculating the normalized power dissipation of an emitting dipole near this planar interface. For this purpose, we use the thin film structure whose cross-section is shown in Figure 4.8. From bottom to top, the complete structure consists of the Si wafer, bottom Al_2O_3 layer, nonstacked or stacked CQW monolayer, spacer Al_2O_3 (if any) and the QD dipole. The only-donor film is composed of a QD dipole over the bottom Al_2O_3 layer and Si substrate, while the FRET system without a spacer is only missing the Al_2O_3 spacer layer. The bottom Al_2O_3 layer has a fixed film thickness of 25 nm and a refractive index of 1.74. The real part of the refractive index of the CQW layer, which is composed of both the CQWs and their surrounding ligands, is taken as 1.7 [17]. The imaginary part of the refractive index of the CQW slab is taken as $\bar{k} = 0.065$ and $\bar{k} = 0.080$ for the

face-down and edge-up CQW monolayer, respectively, with the difference being caused by the different filling factors in both CQW orientations. The thickness of this layer is taken as 5 nm (18 nm) for the face-down (edge-up) CQW monolayer. The thickness of the spacer layer varies between 0 and 15 nm (0 nm thickness corresponding to the case of no spacer). The QD dipole is placed $z_0 = 6$ nm above the nearest surface (to account for the QD radius of 4.1 nm and the ligand length of ∼1.8 nm).

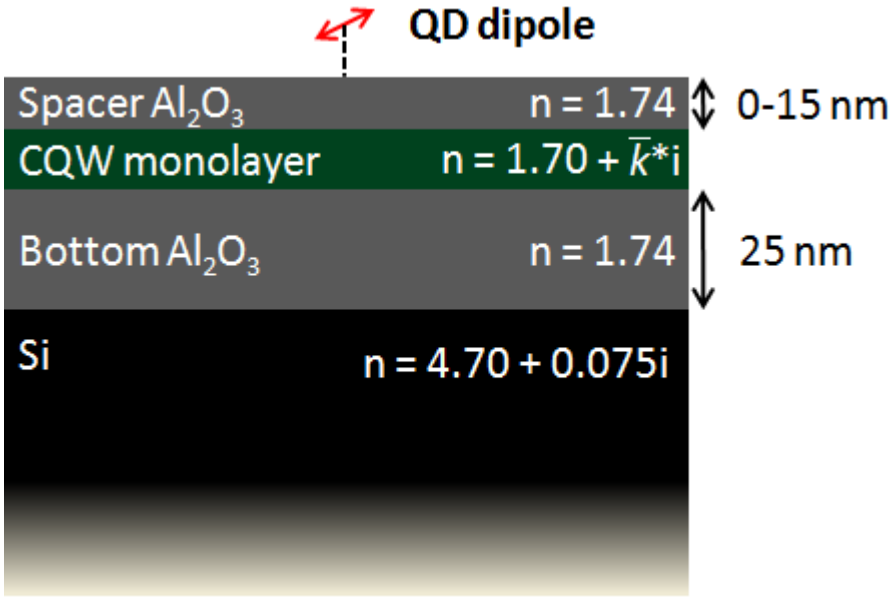

Figure 4.8: Schematic cross-section of the layered media below an isotropic QD dipole. For the only-donor system, there are no CQW or spacer layers. For the FRET system without a spacer, there is no Al_2O_3 layer on top. $\bar{k}$ is 0.065 for the face-down CQW monolayer and 0.080 for the edge-up one.

The normalized power dissipation near a planar interface is given by [158]

$$F = \frac{P}{P_0} = 1 + \frac{3}{4}\frac{\mu_x^2 + \mu_y^2}{\mu^2}\int_0^\infty Re\left\{\frac{s}{s_z}(r^{(s)} - s_z^2 r^{(p)})e^{i2kz_0 s_z}\right\} ds + \frac{3}{2}\frac{\mu_z^2}{\mu^2}\int_0^\infty Re\left\{\frac{s^3}{s_z}r^{(p)}e^{i2kz_0 s_z}\right\} ds \tag{4.27}$$

Here, $\vec{\mu}$ is the dipole moment, $k = 2\pi/\lambda$ is the wavenumber for $\lambda = 460$ nm, $s = k_\rho/k$ with k_ρ being the radial component of the wavevector $\vec{k}$, and $s_z = \sqrt{1 - s^2}$. $r^{(s)}$ and $r^{(p)}$ are the reflection coefficients for the transverse electric (TE) and the

transverse magnetic (TM) radiation, respectively, and are calculated for each s using the transfer matrix formalism [29]. Accordingly, the wave transfer matrix for a multilayered system is given by

$$M = \frac{1}{t'} \begin{bmatrix} tt' - rr' & r' \\ -r & 1 \end{bmatrix} \tag{4.28}$$

where t (t') and r (r') are the polarization-dependent forward (backward) transmission and reflection coefficients, respectively, at the top interface. The transfer matrix for the cascaded system, which is different for s- and p-polarizations, is calculated by multiplying the transfer matrices $M_{i\to j}$ for the interface between media i and j and the transfer matrices U for the propagation along the medium i. For the i-j interface,

$$M_{i\to j} = \frac{1}{t_{ji}} \begin{bmatrix} t_{ij}t_{ji} - r_{ij}r_{ji} & r_{ji} \\ -r_{ij} & 1 \end{bmatrix} \tag{4.29}$$

where r_{ij} and t_{ij} are, respectively, the transmission and reflection coefficients from medium i to medium j. These coefficients are polarization- and wavevector-dependent and calculated by

$$r_{ij}^{(s)} = \frac{k_{zi} - k_{zj}}{k_{zi} + k_{zj}} \tag{4.30}$$

$$t_{ij}^{(s)} = \frac{2k_{zi}}{k_{zi} + k_{zj}} \tag{4.31}$$

$$r_{ij}^{(p)} = \frac{n_j^2 k_{zi} - n_i^2 k_{zj}}{n_j^2 k_{zi} + n_i^2 k_{zj}} \tag{4.32}$$

$$t_{ij}^{(p)} = \frac{2n_i n_j k_{zj}}{n_j^2 k_{zi} + n_i^2 k_{zj}} \tag{4.33}$$

where the superscript s (p) indicates the TE (TM) polarization, and k_{zi} (k_{zj}) are the z-component of the wavevector in the medium i (j) normal to the planar interfaces. The transfer matrix of propagation is

$$U = \begin{bmatrix} e^{ik_z d} & 0 \\ 0 & e^{-ik_z d} \end{bmatrix} \tag{4.34}$$

where d is the layer thickness.

For the donor-only sample, there is only the bottom Al_2O_3 on top of Si substrate; the overall transfer matrix in this case is therefore

$$M^{(p)} = M^{(p)}_{Al_2O_3 \to Si} U_{Al_2O_3} M^{(p)}_{air \to CQW} \tag{4.35}$$

where $d = 25$ nm for the bottom Al_2O_3.

For the FRET system with no spacer,

$$M^{(p)} = M^{(p)}_{Al_2O_3 \to Si} U_{Al_2O_3} M^{(p)}_{CQW \to Al_2O_3} U_{CQW} M^{(p)}_{air \to CQW} \tag{4.36}$$

Here the thickness of the CQW layer is taken as 5 nm for the nonstacked CQW monolayer and 18 nm for the stacked one.

For the FRET system with a spacer,

$$M^{(p)} = M^{(p)}_{Al_2O_3 \to Si} U_{Al_2O_3} M^{(p)}_{CQW \to Al_2O_3} U_{CQW} M^{(p)}_{Al_2O_3 \to CQW} U_{spacer} M^{(p)}_{air \to CQW} \tag{4.37}$$

Finally, $r^{(s)}$ and $r^{(p)}$ are calculated using Equation 4.28 as

$$r = \frac{-m_{2,1}}{m_{2,2}} \tag{4.38}$$

Here, $m_{r,c}$ is the entry of the overall transfer matrix M in the r^{th} row and c^{th} column. The reflection coefficient is calculated for both polarizations and for every s. The calculated parameters are then inserted into Equation 4.27 for each k in order to compute the normalized power dissipation rate for an isotropic dipole with $\mu_x = \mu_y = \mu_z$.

The calculated power dissipation ratio, F, also corresponds to the radio of the Purcell-enhanced radiative rate, k_r, to the radiative rate in free space, k_{r0}, i.e., $F = k_r/k_{r0}$. For simplicity, we will assume that there is one radiative and one nonradiative channel in the emitter QD with the rates of k_{r0} and k_{nr} in free space, respectively. The radiative decay rate is affected by the medium through Purcell effect. The experimentally measured PL lifetime can be expressed as $\tau = 1/(Fk_{r0} + k_{nr})$ where k_{nr} is not modified by the Purcell enhancement.

Knowing the Purcell-mediated experimental lifetime, the Purcell factor and the quantum yield $QY = k_{r0}/(k_{r0} + k_{nr})$, one can find

$$k_{r0} = \frac{1}{\tau\left(F + \frac{1-QY}{QY}\right)} \tag{4.39}$$

from which the decay time of QDs in free space can be estimated as

$$\tau_0 = \frac{1}{k_{r0} + k_{nr}} = \frac{QY}{k_{r0}} = QY \cdot \tau\left(F + \frac{1-QY}{QY}\right) \tag{4.40}$$

Also, the free space rates can be expressed as $k_{r0} = QY/\tau_0$ and $k_{nr} = (1-QY)/\tau_0$. The total emission rate in the presence of Purcell effect is then

$$k = \frac{1}{\tau} = k_{nr} + Fk_{r0} = \frac{1}{\tau_0}(1 + (F-1)QY) \tag{4.41}$$

Therefore, the lifetime of a QD sample is given by

$$\tau = \frac{1}{k} = \frac{\tau_0}{1 + QY(F-1)} \tag{4.42}$$

The free-space lifetime τ_0 can be estimated using Equation 4.40 with the measured lifetime $\tau = 4.72$ ns, and the calculated Purcell factor of the donor-only sample, $F = 2.63$. The lifetimes of all the other samples were estimated by inserting their Purcell factors into Equation 4.42. The Purcell factor calculated using Equations 4.27-4.38, as well as the QD decay times estimated using Equations 4.40-4.42 are plotted in Figure 4.9. We see here that the QD decay times can be estimated fairly well *via* this approach. In Figure 4.9d is plotted the FRET efficiency calculated with the estimated QD decay times in Figures 4.9b and 4.9c for the samples having the face-down and edge-up CQWs monolayer, respectively. From the fittings to Equation 4.4, we obtain the Förster distance of $d_0 = 10.3$ nm (11.7 mn) and $p = 4.58$ (4.03), which are also close to the experimentally calculated values (see Figure 4.3g). The slight deviation in the estimations for the nonstacked CQW monolayer can be attributed to the omission of the anisotropic absorption characteristics of CQWs and the approximation of the CQW-ligand complex as a homogeneous slab.

Our results agree with those of Nguyen *et al.* in that the phenomenon of FRET can be interpreted as energy dissipation at hetero-interfaces. To further support

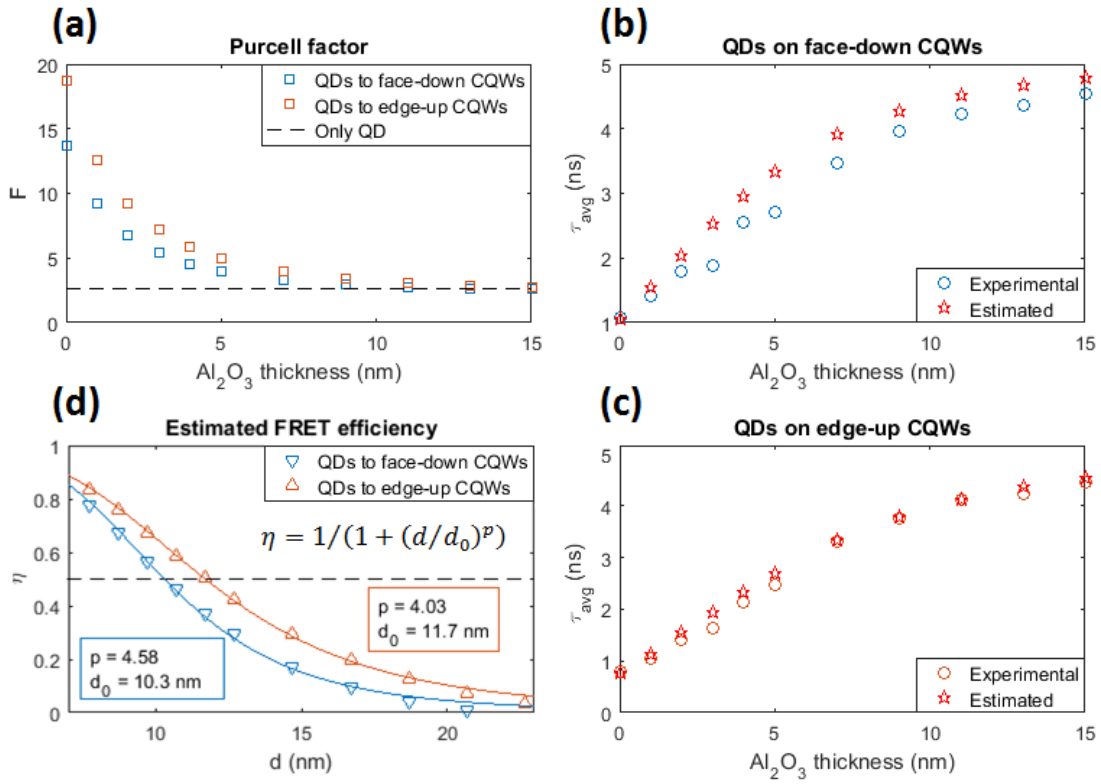

Figure 4.9: Purcell factor analysis on our FRET model system. (a) Calculated Purcell factors F as a function of the spacer thickness for all samples via Equation 4.27. Blue (orange) squares are Purcell factors of QDs over a monolayer of face-down (edge-up) CQWs. Black dashed line is the Purcell factor of the only-QD film. Estimated QD decay lifetimes by incorporating Purcell factor for (b) nonstacked and (c) stacked CQW films. (d) Calculation of FRET efficiency using the estimated lifetimes in (b) and (c). Solid lines show the fits using the FRET efficiency formula given in the inset. With the estimated QD lifetimes, the distance-dependence, as well as the Förster distance of FRET, is estimated and compared to the experimental lifetimes.

this point, we calculate the Purcell factors by assuming the CQWs are lossless, and plotted them in Figure 4.10. It is seen here that this time the Purcell factor is always about 2.5, regardless of the orientation of the CQWs, or the thickness of the spacer, unlike the dissipative CQW case. We therefore conclude that the difference in the Purcell factors in the dissipative and non-dissipative cases is caused by the power absorption, i.e., FRET, into the CQWs.

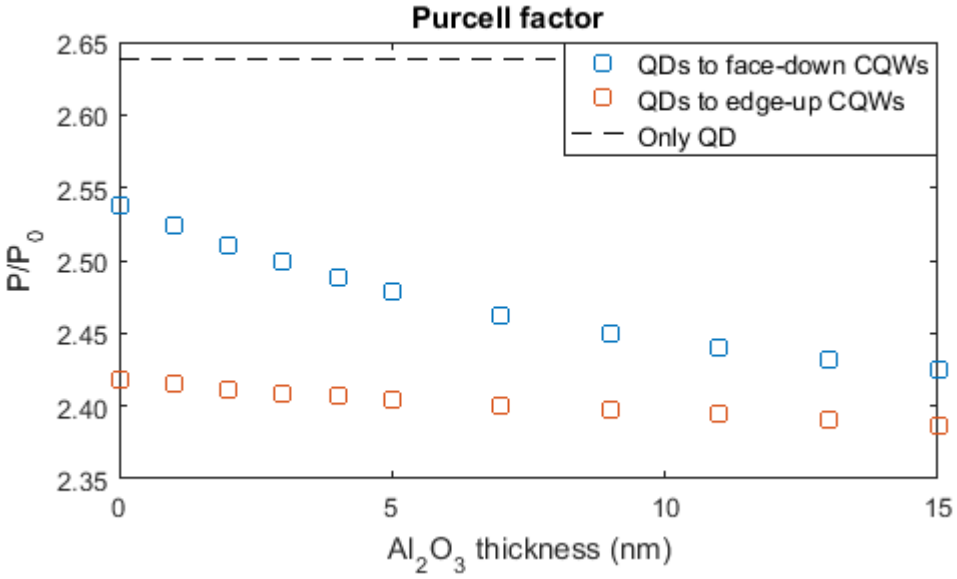

Figure 4.10: Purcell factor for QD-CQW films when the CQW layer is assumed to be lossless.

4.4 Summary

In this study, we demonstrated that tuning the strength of nonradiative energy transfer from QDs to CQWs is possible through controlling the CQW orientation via self-assembly, which in turn changes the dipole alignment factor between the QDs and the CQWs. We showed that the FRET performance of the films substantially differ in each orientation. FRET from QDs to a monolayer of edge-up CQWs is about 50% stronger than to the face-down ones, whereas the distance dependence of their FRET rates is very similar and goes by $\sim d^{-4}$ in both cases as expected for a plane of acceptors. The enhancement of FRET with stacking can

be explained by the stronger dipole-dipole coupling and higher packing density in the vertical orientation. Our approach utilizing Förster theory and taking dipole state delocalization as well as the changing dipole alignment of QDs with differently oriented CQWs into account can successfully estimate the FRET rates from the QDs to monolayers of CQWs in either orientation. While a second approach, by means of which the acceleration in the QD decay is accounted for by the Purcell enhancement near a planar interface has also been utilized, the former model employing FRET theory helped explaining the experimental results more accurately as it accounts for the intrinsic anisotropy of the CQWs. Our study demonstrates a new tool to use dipole interaction of CQWs with other NCs as an additional degree of freedom for tuning the strength of FRET and sheds further light into the orientation-dependent optical properties of anisotropic colloidal semiconductor CQWs.

Chapter 5

Optically Active Planar Waveguides of Multilayered, Self-Assembled CQW Constructs

This chapter is based on our manuscript "Orientation-Controlled Construction of Superstructures of Atomically-Flat Nanocrystals: Pushing the Limits of Ultra-Thin Collidal Gain Media" by O. Erdem *et al.*, submitted (2020).

Colloidal semiconductor nanocrystals (NCs) have been widely utilized for the past two decades as lasing material, largely owing to their favorable properties including color tunability, high quantum yield and stability. NCs of different dimensionalities, including quasi 0-dimensional quantum dots, quasi 1-dimensional quantum wires and quasi 2-dimensional colloidal quantum wells each have thus far have been characterized in terms of their optical gain performance and utilized as optical gain media for NC lasers [3,17,115,119,159,160]. Colloidal quantum wells (CQWs) are the most recent class of these colloical semiconductor NCs, which have attractive properties for lasing, including narrow emission linewidth thanks to their atomically flat lateral surfaces and enhanced oscillator strength thanks to their very tight vertical confinement [12]. Soon after their introduction, CQWs have been shown to be an excellent class of nanoemitters for

lasing applications as they displayed suppressed inhomogeneous broadening [12, 13], reduced gain thresholds [17, 55, 161] and escalated gain coefficients [162]. Up to date, different compositions and size of CQWs [17, 58, 81, 122] have been evaluated for their optical gain performance.

In order to test the optical gain performance of NCs or create NC lasing devices on solids, films of NC emitters typically require a certain thickness to display optical gain. The films are commonly prepared via spin-coating of a concentrated NC solution or drop-casting onto the film to make sure that there is a sufficient amount of nanoemitters, as well as a sufficient film thickness. However, using these standard procedures renders it challenging to control the film thickness, as well as occasionally introducing inhomogeneity into the film and variation of thickness that is usually undesirable as they contribute to optical losses. As a result, studying and understanding the NC optical gain by taking the film thickness into account is cumbersome. To overcome these issues, we propose and develop a new NC thin film deposition technique based on liquid-air interface self-assembly [25], through which we were able to create large-scale orientation- and thickness-controlled films of CQWs. For this, we deposit our CQWs essentially on any arbitrary substrate *via* this unique self-assembly technique sequentially as many times as desired, thereby defining an exact thickness for our CQW films while maintaining the excellent homogeneity throughout the film. We therefore create large-area slabs of CQWs with desired thickness, which can also be utilized as optically active waveguides.

Using CQWs with superior optical gain properties in this work, we have been able to create ultra-thin CQW films that can display gain. By systematically studying the optical gain properties of these thickness-controlled CQW superstructures, we observed that optical gain can be obtained from a CQW film having only 6 layers of CQWs, corresponding to a mere 42 nm film thickness. This thickness is much smaller than the previously reported thicknesses typically of few 100s nm for the NC films displaying optical gain [45,119,162,163], and to the best of our knowledge, the thinnest ever reported optical gain media without using any optical feedback on a bare substrate or any additional means of optical mode confinement. Through numerical mode analysis, we find that

the observation of optical gain from thin films is limited by the critical thickness, below which no waveguiding mode within the CQW slab exists. Below this critical thickness, which is thus a cut-off thickness for optical waveguiding in the CQW slab, the resulting confinement factor is practically zero. Right above the critical thickness, however, there is a sudden major jump of 4 orders of magnitude in the confinement factor. By increasing the number of CQW layers in the film further beyond the critical thickness, we were able to observe gradual decrease in the gain threshold, which can be explained by progressively increasing field confinement factor within the CQW slab.

Thanks to the precise control of film thickness granted by our deposition technique, we were able to study the optical gain properties of CQW as a function of the film thickness at monolayer precision. Our results show that CQWs as well as other types of NCs can benefit from this sequential liquid-air interface deposition technique for creation of two- or three-dimensional optical gain media across device-scale areas.

5.1 Optical Gain in Thickness-Controlled CQW Self-Assemblies

In this thesis work, CdSe/$Cd_{0.25}Zn_{0.75}S$ core/alloyed-shell CQWs were used for multilayered CQW deposition. The synthesis of the CQWs as well as their multilayered self-assembly is described in Chapter 4. In order to characterize the CQW slabs in terms of their optical gain performance, we deposited the CQW multilayers through our self-assembly procedure with a varying number (n) of CQW layers up to $n = 15$. We use a stripe excitation configuration for the ASE measurements, where the optical pump is normally incident on the specimen and the PL emission is collected from the side [126]. The overall experimental setup is displayed in Figure 5.1. The incident pump has a wavelength of 800 nm with a 1 KHz pulse rate and a $\sim$110 fs pulse width. This incident beam is attenuated with a neutral density filter, and passed through a frequency-doubling barium

borate crystal, which converts some of the input beam to 400 nm pump. The rest of the 800 nm light is filtered out with the help of a short-pass filter. The 400 nm beam is divided into two by a 50:50 beam splitter. The beam that passes through is focused onto our sample with a cylindrical lens so that a stripe-like portion of the sample is excited. The PL emission of the CQWs deposited on the sample is collected from the side of the substrate with the help of an optical fiber while the pump fluence is varied. At each measurement, the power of the incident beam is measured simultaneously with a powermeter. The pump fluence is estimated by dividing the pulse energy by the beam area, which is measured by a beam profiler.

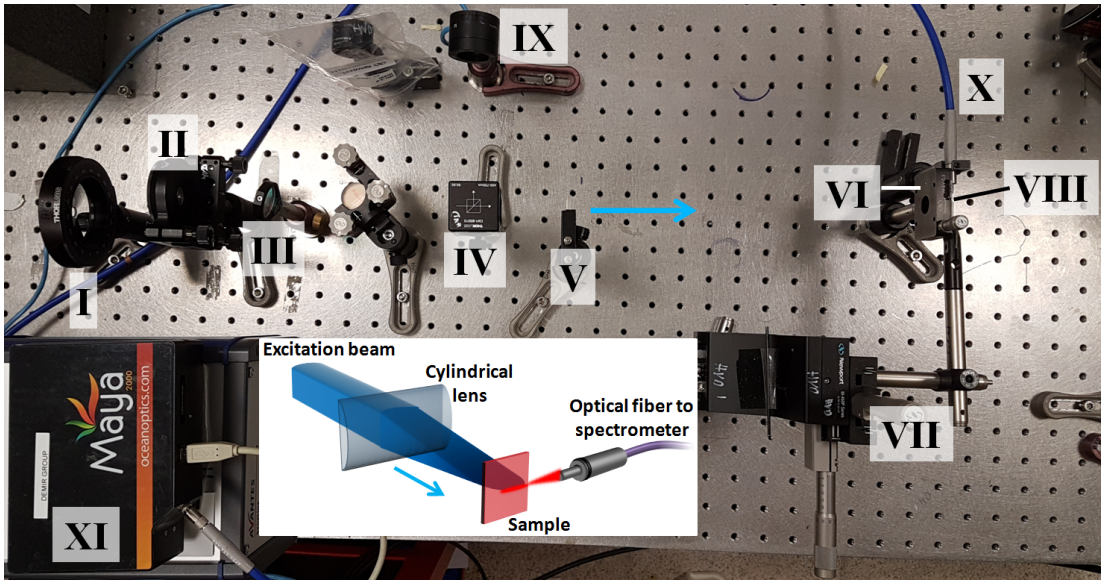

Figure 5.1: Photograph of the optical gain characterization setup. I: attenuator, II: barium boreate crystal, III: short-pass filter, IV: beam splitter, V: cylindrical lens, VI: tunable slit, VII: xyz stage, VIII: sample, IX: powermeter, X: optical fiber, and XI: optical spectrometer. The inset depicts the optical setup schematically. Blue arrows in the photo and the inset show the direction of propagation of the excitation pump.

Multilayered CQW superstructures having different numbers of layers from $n = 1$ to $n = 15$ have been examined in terms of their optical gain performance using this setup. We have been able to observe amplified spontaneous emission (ASE) from these films with $n = 6$ or above, whereas no ASE has been observed for $n \leq 5$. We therefore present our results for the films ranging from $n = 6$ (42

nm thick) to $n = 15$ (105 nm thick). The PL spectra collected at various pump intensities for $n = 6$, 9 and 15 are plotted in Figure 5.2a. ASE is evident in these three cases from the emergence of the second emission feature beyond a threshold intensity, as well as the superlinear increase of the integrated emission intensity (Figure 5.2b). The per-pulse gain thresholds for these three cases have been determined to be 31.3, 12.8 and 7.5 µJ/cm^2 for $n = 6$, 9 and 15, respectively. The tendency of the gain threshold to drop with increasing n is also seen in Figure 5.2c, where the thresholds for the films of all the thicknesses from $n =$ 6 to 15 are plotted. The gradual drop of the gain threshold continues up to n = 15, for which it is 7.5 µJ/cm^2. This value is also on par with the reported gain thresholds of CdSe-based core/shell CQWs synthesized with hot-injection technique [55, 56, 164, 165].

Another notable observation is the evolution of the spectral position of the ASE peak with respect to the spontaneous emission for varied n. In Figure 5.2d, one PL spectrum for each n is plotted at a pump intensity that is slightly above the respective gain thresholds. The spectra are fitted to double Gaussian function, whose parameters are presented in Table 5.1. For the thinnest slabs, the ASE peak displays a little or no shift with respect to the spontaneous emission peak. As n keeps increasing beyond 9, however, a gradual increase in the red-shift of this peak is observed until $n = 15$ (see Figure 5.2d), where the ASE peak saturates at around 664 nm (see Figure 5.2d and Table 5.1) and its red shift is determined to be 18.2 nm. A similar change in the shift of ASE peak with film thickness has previously been observed with the thin films composed of other types of emitters, and was attributed to the change in the critical wavelength of propagation in the planar waveguides as the film thickness is varied [166, 167]. In our case, this shift of the ASE peak allows for fine tuning of the optical gain wavelength across a 17 nm wide spectral band (see Table 5.1) simply by precisely adjusting the CQW waveguide thickness, which is controlled by the sequential CQW deposition.

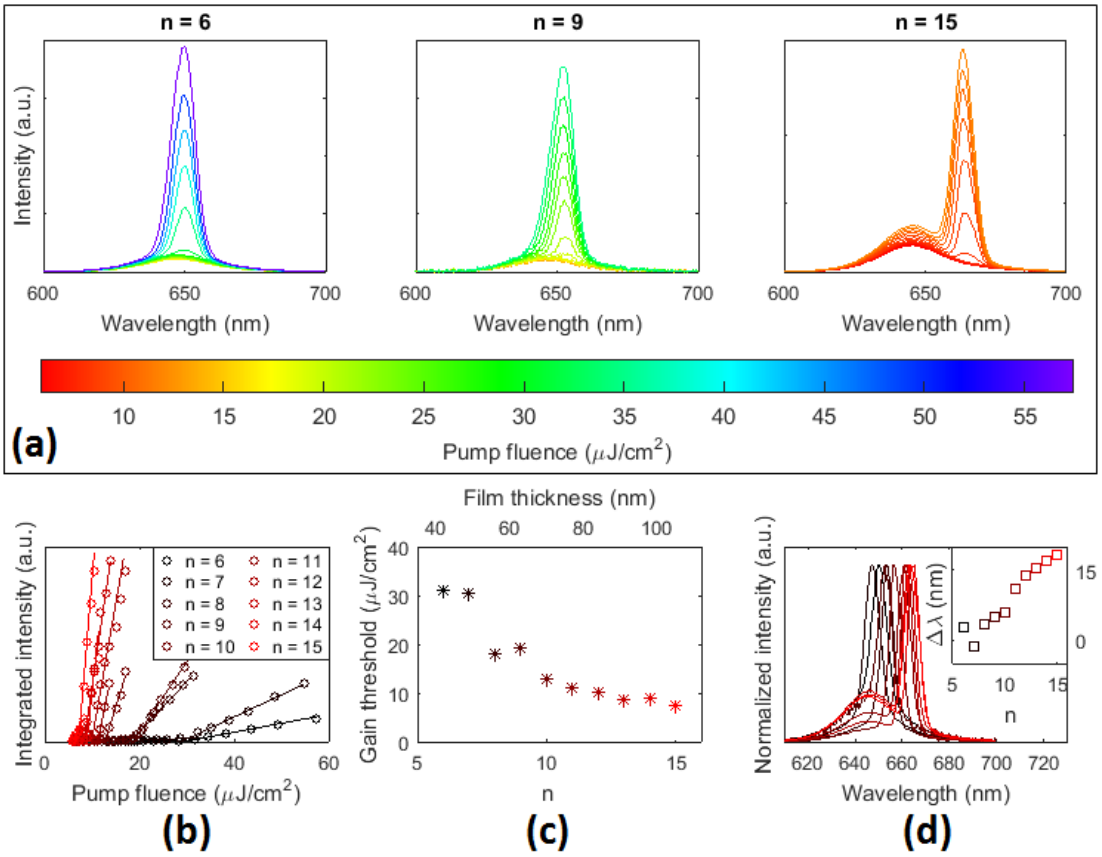

Figure 5.2: (a) Emission spectra of the CQW films having a different number (n) of layers excited with a pulsed laser at 400 nm: left, $n = 6$, center, $n = 9$ and right, $n = 15$. Colorbar at the bottom is common for all three plots. (b) Integrated intensity as a function of the pump fluence for all the CQW films from $n = 6$ to $n = 15$. (c) Evolution of the optical gain threshold with the number of layers n as deduced from the data in panel b. (d) Shifting of the ASE peak with respect to the spontaneous emission for different n. Inset shows the difference between the ASE and spontaneous emission peaks. The color coding is identical in panels b-d. Reprinted from Ref. [131]

.

Table 5.1: Gaussian fitting parameters for the ASE spectra presented in Figure 5.2d. Peak and full-width-at-half maximum (FWHM) values for spontaneous emission (SE) and ASE features. Adapted from Ref. [131].

	SE		ASE	
# layers	Peak (nm)	FWHM (nm)	Peak (nm)	FWHM (nm)
6	647.6	31.8	650.2	7.18
7	648.8	32.6	647.4	7.41
8	650.3	29.1	653.7	5.94
9	647.8	30.3	652.7	6.53
10	651.3	35.0	657.1	6.16
11	649.7	35.5	660.8	5.94
12	648.0	34.0	661.9	5.71
13	647.7	32.3	663.0	5.53
14	647.7	33.0	664.8	5.49
15	645.9	31.1	664.1	7.21

5.2 Tuning the Modal Confinement and Amplified Spontaneous Emission Wavelength

To elaborate on the observed gain characteristics of the CQW slabs, we employed a numerical analysis of guided modes within the CQW layer. To this end, we approximate the CQW multilayer as an optically active homogeneous planar medium. Our overall structure can then be modeled as an asymmetric planar waveguide, where a thin CQW slab is sandwiched between two semi-infinite media, i.e., fused silica and air. This structure is depicted in Figure 5.3, where three media of air, CQW slab and fused silica have refractive indices of $n_1 = 1.00$, $n_2 = 2.10$ and $n_3 = 1.45$, respectively. Since the refractive index of the CQW slab is larger than the neighbouring semi-infinite media, this configuration allows light propagation within the CQW media through total internal reflection off both interfaces. For understanding the propagation of guided modes, we use the well-established planar waveguide formalism. Accordingly, the wave equation to be solved is [168]

$$\left(\frac{\partial^2}{\partial x^2} + \frac{\partial^2}{\partial y^2}\right)\vec{E}(x,y) + (k_0^2 n_i^2 - k_{2z})\vec{E}(x,y) = 0 \tag{5.1}$$

where k_0 is the wavenumber in vacuum, k_{2z} is the z-component of the wavevector in the CQW medium and $i = 1$, 2 or 3. When $n_2 > n_1$, n_3, the boundary conditions for physically realizable solutions are the continuity of the tangential component of $\vec{E}$ at the boundaries and the field amplitudes to go to zero at infinity. This requires that the solution is sinusoidal within the slab and decaying exponentials in the semi-infinite media, which is possible when $k_{2z} > k_3$ and $k_{2z} > k_1$. Each independent solution to Equation 5.1 corresponds to a mode of the waveguide with its wavefunction and propagation constant. These modes can be transverse electric (TE), where the electric field is perpendicular to the plane of incidence, or transverse magnetic (TM), where the magnetic field is perpendicular to the plane of incidence. Considering the coordinate axes in Figure 5.3, where the plane of incidence is the xz-plane, the TE modes in this configuration have only the y-component of the electric field, E_y. Similarly, the TM modes will have only the y component of the magnetic field, H_z which means that x- and z-components will be present in the electric field wavefunction of the TM modes.

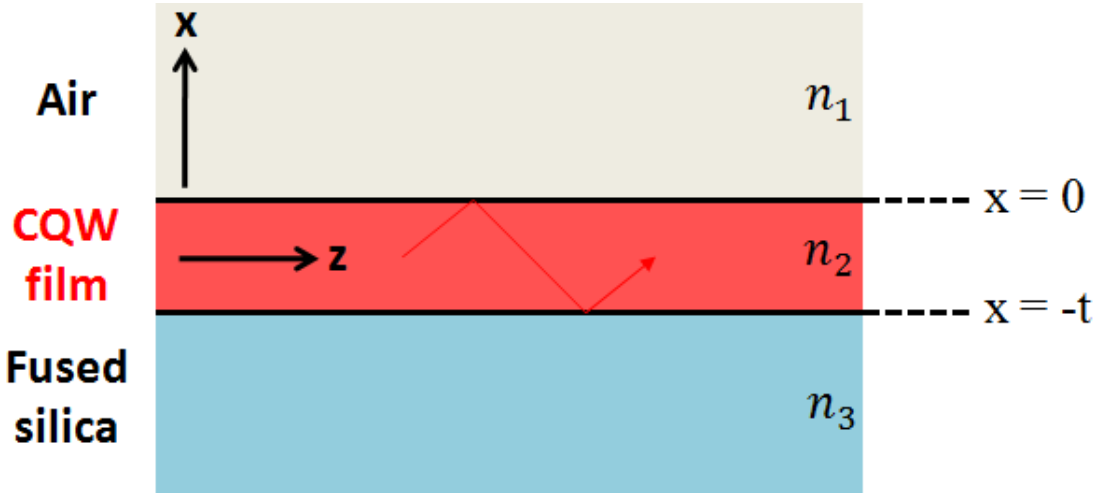

Figure 5.3: Asymmetric waveguide structure for a multilayered CQW construct of thickness t.

For the TE modes, the solution for the electric field will have the form

$$E_y = E_m(x)e^{i(\omega t - k_{2z}z)} \tag{5.2}$$

Due to the homogeneity along the yz-plane, the wavefunction E_m is only a function of x. In the case of nonmagnetic media, the general boundary conditions

mentioned above corresponds to the continuity of E_y and $\partial E_y/\partial x$ across the interfaces (i.e., $x = 0$ and $x = -t$). Imposing continuity of E_y at $x = 0$ and $x = -t$ as well as the continuity of $\partial E_y/\partial x$ at $x = 0$, we obtain

$$E_m = \begin{cases} Ce^{-qx}, & x \geq 0 \\ C\cos(hx) - \frac{q}{h}\sin(hx), & 0 \geq x \geq -t \\ C\cos(ht) + \frac{q}{h}\sin(ht), & x \leq -t \end{cases} \tag{5.3}$$

where C is a normalization constant, $h = \sqrt{k_2^2 - k_{2z}^2}$, $q = \sqrt{k_{2z}^2 - k_1^2}$ and $p = \sqrt{k_{2z}^2 - k_3^2}$. Finally, when the continuity of $\partial E_y/\partial x$ at $x = -t$ is also imposed, the relation

$$\tan(ht) = \frac{p+q}{h(1-pq/h^2)} \tag{5.4}$$

can be reached. This equality is called the mode condition, which determines the propagation constant k_{2z} of a guided mode.

Equation 5.4 indicates that there is a minimum slab thickness $t = t_c$ that enables the presence of the waveguiding modes. At this cutoff thickness, $k_{2z} = k_3$, i.e., $p = 0$. In this case, Equation 5.4 can be rewritten as

$$\tan(ht) = \frac{q}{h} \tag{5.5}$$

or equivalently

$$\tan\left(t_c \frac{2\pi}{\lambda}\sqrt{n_2^2 - n_3^2}\right) = \sqrt{\frac{n_3^2 - n_1^2}{n_2^2 - n_3^2}} \tag{5.6}$$

From this equation we can arrive at

$$t_c \frac{2\pi}{\lambda}\sqrt{n_2^2 - n_3^2} = m\pi + \tan^{-1}\left(\sqrt{\frac{n_3^2 - n_1^2}{n_2^2 - n_3^2}}\right) \tag{5.7}$$

where $m = 0, 1, 2...$ is an integer that denotes the m^{th} mode ($\mathrm{TE_m}$). The critical thickness for the ($\mathrm{TE_m}$) mode is then

$$t_c = \frac{\lambda}{2\pi\sqrt{n_2^2 - n_3^2}}\left(m\pi + \tan^{-1}\left(\sqrt{\frac{n_3^2 - n_1^2}{n_2^2 - n_3^2}}\right)\right) \tag{5.8}$$

Similarly, the critical thickness for the TM_m modes can be derived by [168]

$$t_c = \frac{\lambda}{2\pi\sqrt{n_2^2 - n_3^2}} \left(m\pi + \tan^{-1}\left(\frac{n_2^2}{n_1^2}\sqrt{\frac{n_3^2 - n_1^2}{n_2^2 - n_3^2}} \right) \right) \tag{5.9}$$

Since $n_2 > n_1$, t_c is larger for TM waves. We are going to limit the current discussion with the TE modes.

Equation 5.3 implies that even though the wave is guided, part of its energy flows outside the guiding layer. The fraction of the power that propagates within the waveguide depends on the waveguide thickness t and is given by

$$\Gamma = \frac{Re\left\{ \int_{-t}^{0} (\vec{E} \times \vec{H}^*) \cdot \vec{z} dx \right\}}{Re\left\{ \int_{-\infty}^{\infty} (\vec{E} \times \vec{H}^*) \cdot \vec{z} dx \right\}} \tag{5.10}$$

For our CQW slabs, inserting the parameters $n_1 = 1.00$, $n_2 = 2.10$, $n_3 = 1.45$ and $\lambda = 650$ nm into Equation 5.8 reveals the critical slab thickness to be 41.2 nm for TE_0 mode, which is in accordance with the experimental onset of ASE in our multilayered CQWs observed with 6 layers (film thickness of 42 nm). Due to the ultra-thin CQW film, only a small portion of the propagating field is confined within the actual gain medium, as seen in Figure 5.4a. The mode confinement factor Γ is calculated as 6.3×10^{-3} at this thickness. Using a commercially available mode solution software package (Lumerical FDTD) with a two-dimensional layout, we solve for the electric field distribution for all x and the resulting mode confinement factor for CQW slabs having different number of layers ranging from $n = 1$ to $n = 15$. The resulting confinement factor as a function of n is plotted in Figure 5.4b, where it is seen to increase monotonously with the number of CQW layers (i.e. CQW film thickness). More notably, Γ undergoes a significant jump of 4 orders of magnitude from $n = 5$ to $n = 6$ due to the onset of waveguiding. Γ increases further beyond $n = 6$, thereby effectively being able to confine more of the propagation field. By increasing the thickness of the gain medium, the optical gain is therefore facilitated by the stronger confinement of the optical mode within the CQW slab, which explains the continuously decreasing gain threshold with increasing film thickness.

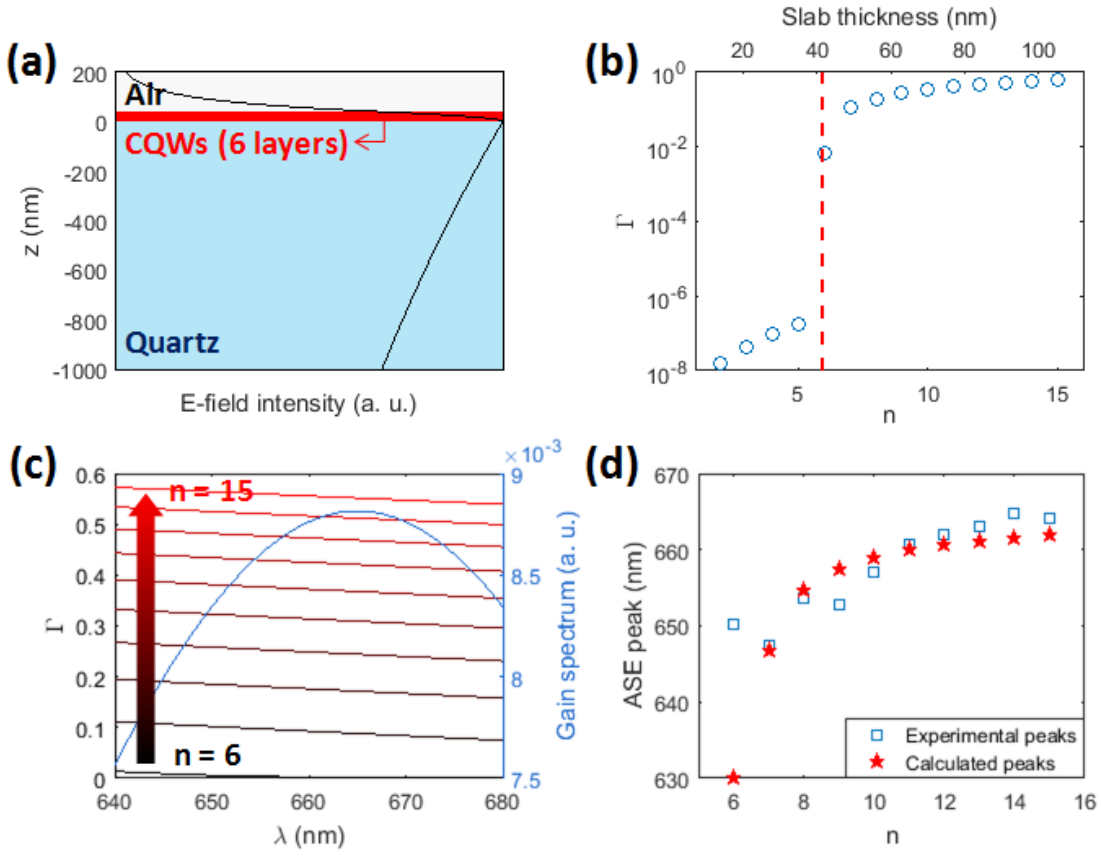

Figure 5.4: (a) Field intensity profile of the fundamental TE mode numerically calculated for the CQW slab with $n = 6$. (b) Optical confinement factor Γ calculated at 650 nm for varied numbers of CQW layers (and slab thickness). Dashed line indicates the critical thickness of 41.2 nm for the existence of propagating modes within the slab. (c) Left axis: Variation of the confinement factor Γ with wavelength for different numbers of layers. Right axis: Gain spectrum $\Gamma(\lambda)$ for our CQWs estimated using the measured ASE peaks at different film thicknesses, modeled as a Gaussian centered at 665 nm with a FWHM of 106.6 nm (blue) (d) ASE peaks calculated as the maximum of $\Gamma(\lambda) \times G(\lambda)$ for each n (red stars), together with the experimentally measured ASE peaks (blue squares). Adapted from Ref. [131].

To account for the spectral shifting of the ASE peak with film thickness, we consider the varience of the mode confinement with mode wavelength. Previously, observing a similar trend in the ASE peak of optically pumped polystyrene films, Calzado *et al.* argued qualitatively that each vibronic mode experiences a different propagation loss at different film thicknesses. As a result, the losses for the modes having longer wavelengths are enhanced compared to those supported at shorter wavelengths, which explains the blue-shift of the ASE peak at thinner polystyrene films [167]. A similar argument can be made for our CQW constructs as well since the mode confinement near the critical thickness is highly sensitive to the wavelength, as seen in Figure 5.4c. Furthermore, CQWs as well as other classes of NCs provide a certain gain bandwidth, which determines the spectral range of gain that can be observed from the material. In the generic case, this gain band is not flat, i.e., the material gain coefficient G is a function of λ. The total gain coefficient of a thin film is then given by $g(\lambda) = \Gamma(\lambda)G(\lambda)$, neglecting the losses. In this case, the peak of the ASE feature will be the maximum of $g(\lambda)$.

To test if this simple formalism can explain the observed shift in the ASE peak, we model the material gain spectrum as a generalized Gaussian function:

$$G(\lambda) = G_c e^{-\left(\frac{|\lambda-\lambda_c|}{\alpha}\right)^{\beta}} \tag{5.11}$$

where G_c is the gain coefficient at the peak wavelength λ_c, and α and β are parameters related to the width and shape of the lineshape, respectively. λ_c is fixed at 665 nm since it is the peak of the most red-shifted ASE feature among all the tested multilayered films. The parameters α and β are swept to find the parameter couple that minimizes the difference between the experimentally measured ASE peaks and the calculated ones. The optimum parameters found this way are $\alpha = 64$ and $\beta = 2.0$, for which Equation 5.11 is plotted in Figure 5.4c (blue curve). The calculated ASE peaks are plotted in Figure 5.4d, along with the experimentally determined peaks. We see that, apart from the ASE peak for $n = 6$, the assumed $G(\lambda)$ can estimate the trend in the ASE peak shift fairly well. The discrepancy at $n = 6$ is most likely due to the actual $G(\lambda)$ having a finite range that has a cut-off above 630 nm. Therefore, the blue-shift of the ASE peak at thinner films is limited by the finite gain band of the material. It is also worth noting that, because of very thick films $\Gamma(\lambda) \simeq 1$ throughout the gain band,

this model can readily predict that, with increasing thickness, the ASE peak will converge to λ_c. Indeed, the experimental ASE peaks are seen to be saturating towards a definite red-shift around $\lambda = 665$ nm. Although this type of red-shift is expected for NCs having type-I band alignment [118], here we show that it is possible to obtain non-shifting ASE from type-I NCs by using their ultra-thin films.

5.3 Summary and Discussion

In this work, we have created planar waveguides made out of CQW superstuctures in face-down orientation by sequentially-repeated liquid interface self-assembly technique, which is applicable to large scales. The films deposited with this technique is used to elaborate on the optical gain properties of the CQWs we used, by taking into account the film thickness, which can be controlled in monolayer precision. In these films, the degree of optical confinement is revealed as a function of the number of CQW layers, or equivalently, the film thickness. The gradually decreasing gain threshold observed with increasing number of layers is revealed to result from the increasing optical confinement with the number of deposited CQW layers. Furthermore, we showed that the ASE feature can be continuously tuned within a wavelength range of ∼18 nm simply by changing the film thickness. The analyses on the optical confinement as a function of the propagation wavelength can estimate this shift of the ASE peak in thin films.

The results of our thesis work paves the way for using ultra-thin CQW films, where thicker films impede the gain performance. In the case of electrically-driven NC films, for instance, the organic surfactants passivating the NC surface act as insulating barriers that hinder charge or heat transfer, limiting their use in electroluminescent devices. The ultimate thickness of our CQW film inducing optical gain is as small as ∼40 nm, with only 6 layers of CQWs, may help addressing this problem by reducing the organic barriers that should be overcome by the electric current in the vertical direction. This work may therefore serve as a foundation for developing the optically active media of electrically-driven CQW

lasers without having to switch to inorganic ligands.

Chapter 6

Conclusion

6.1 Future Outlook

In this thesis, based on the liquid-air interface self-assembly techniques we proposed and developed the construction of thickness- and orientation-controlled films of colloidal CQWs. These CQW films, which were deposited on a variety of surfaces, including silicon, fused silica and Al_2O_3, were used to study the optical properties of CQWs from various aspects, including their anisotropic dipole interactions and optical gain depending on the film thickness. Specifically, using orientation-controlled self-assembly, through which CdSe core CQWs were assembled onto cm^2-large areas with near-unity surface coverage and in desired orientation (i.e., either all face-down or all edge-up), we have shown that nonradiative energy transfer to a CQW monolayer can be tuned with the CQW orientation. We were able to explain our experimental results using a generalized Förster theory, where orientation- and position-dependent average dipole-dipole alignment factor and the delocalization of the excitonic state in the CQWs were taken into account. This work has been the first demonstration of orientation-controlled energy transfer with CQWs.

In the other study of this thesis, we deposited multiple layers of all-face-down CdSe/CdZnS core/shell CQWs sequentially, i.e., one layer at a time, which enabled precise control of film thickness while maintaining the excellent homogeneity across areas as large as several tens of cm^2. These high-quality films have been used to conduct a thickness-dependent optical gain study with CQWs for the first time. We have shown the gradual decrease in the gain threshold in these multilayered CQW films as the number of layers is progressively increased. Furthermore, we have demonstrated an uncharacteristic spectral shift of the amplified spontaneous emission (ASE) feature (by $\sim$18 nm) with changing film thickness. Using the mode confinement calculations, we have found that the decrease in the gain threshold as well as the gradual red-shift of the ASE peak can be accounted for by the variation in the mode confinement factor with the CQW film thickness as well as the propagation wavelength. Obtaining these results has been possible thanks to the large-area, orientation-controlled self-assembled CQWs, which enabled deposition of highly uniform, thickness-tunable CQW films.

Our results indicate that liquid-air interface self-assembly holds a great potential for being used in device fabrication as it presents a bottom-up approach for creating two- and three-dimensional CQW superstructures. The unprecedented precision in the CQW film thickness with ultra-low surface roughness enables utilization of these CQW constructs as optically active waveguides, which can be used for in- and out-of-plane optical applications. Furthermore, the orientation control of these anisotropic CQWs through self-assembly deposition presents interesting opportunities for optical applications that can make use of directed emission, such as LEDs and lasers. Therefore, liquid-air interface self-assembly not only facilitates the incorporation of CQWs into optoelectronic devices, but it also holds the potential to increase the efficiency of these devices due to their favorable optical properties including but not limited to enhanced absorption cross-section, narrow emission linewidth and intrinsic optical anisotropy.

Our self-assembly technique for bottom-up construction of three-dimensonal CQW films can also be extended to include deposition of colloidal semiconductor

nanocrystals (NCs) of other classes. In this case, the sequential deposition technique can be used to create hybrid NC superstructures where each layer is composed of a different type of of NC. Such an approach can potentially find use in applications such as photonic crystals.

In the future outlook, self-assembled deposition of CQWs opens up a lot of different possible directions in the utilization of CQWs for optoelectronics, only a small portion of which has been studied and demonstrated in this thesis. More thorough studies on the optical properties of the CQWs as well as their utilization in devices is possible through their orientation- and thickness-controlled thin films. Further optimization of the deposition techniques for various CQW dimensions and heterostructures can further broaden these possibilities.

6.2 Contributions to Literature

6.2.1 Publications

1. **O. Erdem**, K. Gungor, B. Guzelturk, I. Tanriover, M. Sak, M. Olutas, D. Dede, Y. Kelestemur, H. V. Demir. "Orientation-Controlled Nonradiative Energy Transfer to Colloidal Nanoplatelets: Engineering Dipole Orientation Factor," *Nano Letters*, vol. 19, no. 7, pp. 4297-4305, 2019

2. **O. Erdem**, S. Foroutan, N. Gheshlaghi, B. Guzelturk, Y. Altintas, H. V. Demir. "Orientation-Controlled Construction of Superstructures of Atomically-Flat Nanocrystals: Pushing the Limits of Ultra-Thin Colloidal Gain Media" arXiv: 2005.10724 [physics.app-ph], 2020 and *Nano Letters*, 2020 (in revision)

3. **O. Erdem**, M. Olutas, B. Guzelturk, Y. Kelestemur, H. V. Demir. "Temperature-Dependent Emission Kinetics of Colloidal Semiconductor Nanoplatelets Strongly Modified by Stacking," *The Journal of Physical Chemistry Letters*, vol. 7, no. 3, pp. 548-554, 2016

4. Y. Kelestemur, B. Guzelturk, **O. Erdem**, M. Olutas, K. Gungor, H. V. Demir. "Platelet-in-Box Colloidal Quantum Wells: CdSe/CdS@CdS Core/Crown@ Shell Heteronanoplatelets," *Advanced Functional Materials*, vol. 26, no. 21, pp. 3570-3579, 2016

5. Y. Kelestemur, B. Guzelturk, **O. Erdem**, M. Olutas, T. Erdem, C. F. Usanmaz, H. V. Demir. "$CdSe/CdSe_{1-x}Te_x$ Core/Crown Heteronanoplatelets: Tuning the Excitonic Properties without Changing the Thickness," *The Journal of Physical Chemistry C*, vol. 121, no. 8, pp. 4650-4658, 2017

6. Y. Kelestemur, D. Dede, K. Gungor, C. F. Usanmaz, **O. Erdem**, H. V. Demir. "Alloyed Heterostructures of $CdSe_xS_{1-x}$ Nanoplatelets with Highly Tunable Optical Gain Performance," *Chemistry of Materials*, vol. 29, no. 11, pp. 4857-4865, 2017

7. N. Taghipour, P. L. Hernandez-Martinez, A. Ozden, M. Olutas, D. Dede, K. Gungor, **O. Erdem**, N. K. Perkgoz, H. V. Demir. "Near-Unity Efficiency Energy Transfer from Colloidal Semiconductor Quantum Wells of CdSe/CdS Nanoplatelets to a Monolayer of MoS_2," *ACS Nano*, vol. 12, no. 8, pp. 8547-8554, 2018

8. M. Kaur, A. Sharma, M. Olutas, **O. Erdem**, A. Kumar, M. Sharma, H. V. Demir. "Cd-free Cu-doped ZnInS/ZnS Core/Shell Nanocrystals: Controlled Synthesis and Photophysical Properties," *Nanoscale Research Letters*, vol. 13, no. 1, pp. 182, 2018

9. S. Shendre, S. Delikanli, M. Li, D. Dede, Z. Pan, S. T. Ha, Y. H. Fu, P. L Hernandez-Martinez, J. Yu, **O. Erdem**, A. I. Kuznetsov, C. Dang, T. C. Sum, H. V. Demir. "Ultrahigh-Efficiency Aqueous Flat Nanocrystals of $CdSe/CdS@Cd_{1-x}Zn_xS$ Colloidal Core/Crown@Alloyed-Shell Quantum Wells," *Nanoscale*, vol. 11, no. 1, pp. 301-310, 2019

10. Y. Altintas, U. Quliyeva, K. Gungor, **O. Erdem**, Y. Kelestemur, E. Mutlugun, M. V. Kovalenko, H. V. Demir. "Highly Stable, Near-Unity Efficiency Atomically Flat Semiconductor Nanocrystals of CdSe/ZnS

Hetero-Nanoplatelets Enabled by ZnS-Shell Hot-Injection Growth," *Small*, vol. 15, no. 8, pp. 1804854, 2019

11. S. Delikanli, G. Yu, A. Yeltik, S. Bose, T. Erdem, J. Yu, **O. Erdem**, M. Sharma, V. K. Sharma, U. Quliyeva, S. Shendre, C. Dang, D. H. Zhang, T. C. Sum, W. Fan, H. V. Demir. "Ultrathin Highly Luminescent Two-Monolayer Colloidal CdSe Nanoplatelets," *Advanced Functional Materials*, vol. 29, no. 35, pp. 1901028, 2019

12. G. Jiang, **O. Erdem**, R. Hubner, M. Georgi, W. Wei, X. Fan, J. Wang, H. V. Demir, N. Gaponik. "Mechanosynthesis of Polymer-Stabilized Lead Bromide Perovskites: Insight into the Formation and Phase Conversion of Nanoparticles" *Chemistry of Materials*, 2020 (submitted)

6.2.2 Patents

1. S. Jun, H. V. Demir, E. J. Jang, B. Guzelturk, K. Gungor, **O. Erdem**. "Photoluminescent polarizers and electronic devices including the same," US Patent App. 15/862, 182

Bibliography

[1] C. B. Murray, D. J. Norris, and M. G. Bawendi, "Synthesis and characterization of nearly monodisperse CdE (E = sulfur, selenium, tellurium) semiconductor nanocrystallites," *Journal of the American Chemical Society*, vol. 115, no. 19, pp. 8706 – 8715, 1993.

[2] A. L. Rogach, D. V. Talapin, E. V. Shevchenko, A. Kornowski, M. Haase, and H. Weller, "Organization of matter on different size scales: Monodisperse nanocrystals and their superstructures," *Advanced Functional Materials*, vol. 12, no. 10, pp. 653 – 664, 2002.

[3] V. I. Klimov, A. A. Mikhailovsky, S. Xu, A. Malko, J. A. Hollingsworth, C. A. Leatherdale, H.-J. Eisler, and M. G. Bawendi, "Optical gain and stimulated emission in nanocrystal quantum dots," *Science*, vol. 290, no. 5490, pp. 314 – 317, 2000.

[4] M. Kazes, D. Y. Lewis, Y. Ebenstein, T. Mokari, and U. Banin, "Lasing from semiconductor quantum rods in a cylindrical microcavity," *Advanced Materials*, vol. 14, no. 4, pp. 317 – 321, 2002.

[5] B. Guzelturk, Y. Kelestemur, M. Olutas, S. Delikanli, and H. V. Demir, "Amplified spontaneous emission and lasing in colloidal nanoplatelets," *ACS Nano*, vol. 8, no. 7, pp. 6599 – 6605, 2014.

[6] V. L. Colvin, M. C. Schlamp, and A. P. Alivisatos, "Light-emitting diodes made from cadmium selenide nanocrystals and a semiconducting polymer," *Nature*, vol. 370, no. 6488, pp. 354 – 357, 1994.

[7] K. H. Lee, J. H. Lee, W. S. Song, H. Ko, C. Lee, J. H. Lee, and H. Yang, "Highly efficient, color-pure, color-stable blue quantum dot light-emitting devices," *ACS Nano*, vol. 7, no. 8, pp. 7295 – 7302, 2013.

[8] F. Fan, P. Kanjanaboos, M. Saravanapavanantham, E. Beauregard, G. Ingram, E. Yassitepe, M. M. Adachi, O. Voznyy, A. K. Johnston, G. Walters, *et al.*, "Colloidal $CdSe_{1-x}S_x$ nanoplatelets with narrow and continuously-tunable electroluminescence," *Nano Letters*, vol. 15, no. 7, pp. 4611 – 4615, 2015.

[9] B. Liu, Y. Altintas, L. Wang, S. Shendre, M. Sharma, H. Sun, E. Mutlugun, and H. V. Demir, "Record high external quantum efficiency of 19.2% achieved in light-emitting diodes of colloidal quantum wells enabled by hot-injection shell growth," *Advanced Materials*, vol. 32, no. 8, pp. 1 – 10, 2020.

[10] T.-H. Kim, K.-S. Cho, E. K. Lee, S. J. Lee, J. Chae, J. W. Kim, D. H. Kim, J.-Y. Kwon, G. Amaratunga, S. Y. Lee, B. L. Choi, Y. Kuk, J. M. Kim, and K. Kim, "Full-colour quantum dot displays fabricated by transfer printing," *Nature Photonics*, vol. 5, no. 3, pp. 176 – 182, 2011.

[11] S. Ithurria and B. Dubertret, "Quasi 2D colloidal CdSe platelets with thicknesses controlled at the atomic level," *Journal of the American Chemical Society*, vol. 130, no. 49, pp. 16504 – 16505, 2008.

[12] S. Ithurria, M. D. Tessier, B. Mahler, R. P. Lobo, B. Dubertret, and A. L. Efros, "Colloidal nanoplatelets with two-dimensional electronic structure," *Nature Materials*, vol. 10, no. 12, pp. 936 – 941, 2011.

[13] M. D. Tessier, C. Javaux, I. Maksimovic, V. Loriette, and B. Dubertret, "Spectroscopy of single CdSe nanoplatelets," *ACS Nano*, vol. 6, no. 8, pp. 6751 – 6758, 2012.

[14] M. D. Tessier, P. Spinicelli, D. Dupont, G. Patriarche, S. Ithurria, and B. Dubertret, "Efficient exciton concentrators built from colloidal core/crown CdSe/CdS semiconductor nanoplatelets," *Nano Letters*, vol. 14, no. 1, pp. 207 – 213, 2014.

[15] Y. Gao, M. C. Weidman, and W. A. Tisdale, "CdSe nanoplatelet films with controlled orientation of their transition dipole moment," *Nano Letters*, vol. 17, no. 6, pp. 3837 – 3843, 2017.

[16] W. D. Kim, D. Kim, D. E. Yoon, H. Lee, J. Lim, W. K. Bae, and D. C. Lee, "Pushing the efficiency envelope for semiconductor nanocrystal-based electroluminescence devices using anisotropic nanocrystals," *Chemistry of Materials*, vol. 31, no. 9, pp. 3066 – 3082, 2019.

[17] C. She, I. Fedin, D. S. Dolzhnikov, A. Demortiere, R. D. Schaller, M. Pelton, and D. V. Talapin, "Low-threshold stimulated emission using colloidal quantum wells," *Nano Letters*, vol. 14, no. 5, pp. 2772 – 2777, 2014.

[18] F. Feng, L. T. Nguyen, M. Nasilowski, B. Nadal, B. Dubertret, A. Maître, and L. Coolen, "Probing the fluorescence dipoles of single cubic CdSe/CdS nanoplatelets with vertical or horizontal orientations," *ACS Photonics*, vol. 5, no. 5, pp. 1994 – 1999, 2018.

[19] G. Yang, M. Kazes, and D. Oron, "Chiral 2D colloidal semiconductor quantum wells," *Advanced Functional Materials*, vol. 28, no. 28, p. 1802012, 2018.

[20] M. Achermann, M. A. Petruska, S. A. Crooker, and V. I. Klimov, "Picosecond energy transfer in quantum dot Langmuir-Blodgett nanoassemblies," *The Journal of Physical Chemistry B*, vol. 107, no. 50, pp. 13782 – 13787, 2003.

[21] T. Franzl, T. A. Klar, S. Schietinger, A. L. Rogach, and J. Feldmann, "Exciton recycling in graded gap nanocrystal structures," *Nano Letters*, vol. 4, no. 9, pp. 1599 – 1603, 2004.

[22] T. Ozel, S. Nizamoglu, M. A. Sefunc, O. Samarskaya, I. O. Ozel, E. Mutlugun, V. Lesnyak, N. Gaponik, A. Eychmuller, S. V. Gaponenko, and H. V. Demir, "Anisotropic emission from multilayered plasmon resonator nanocomposites of isotropic semiconductor quantum dots," *ACS Nano*, vol. 5, no. 2, pp. 1328 – 1334, 2011.

[23] F. Kim, S. Kwan, J. Akana, and P. Yang, "Langmuir-Blodgett nanorod assembly," *Journal of the American Chemical Society*, vol. 123, no. 18, pp. 4360 – 4361, 2001.

[24] I. Patla, S. Acharya, L. Zeiri, J. Israelachvili, S. Efrima, and Y. Golan, "Synthesis, two-dimensional assembly, and surface pressure-induced coalescence of ultranarrow PbS nanowires," *Nano Letters*, vol. 7, no. 6, pp. 1459 – 1462, 2007.

[25] A. Dong, J. Chen, P. M. Vora, J. M. Kikkawa, and C. B. Murray, "Binary nanocrystal superlattice membranes self-assembled at the liquid-air interface," *Nature*, vol. 466, no. 7305, pp. 474 – 477, 2010.

[26] B. T. Diroll, N. J. Greybush, C. R. Kagan, and C. B. Murray, "Smectic nanorod superlattices assembled on liquid subphases: Structure, orientation, defects, and optical polarization," *Chemistry of Materials*, vol. 27, no. 8, pp. 2998 – 3008, 2015.

[27] I. Suarez, R. Munoz, V. Chirvony, J. P. Martinez-Pastor, M. Artemyev, A. Prudnikau, A. Antanovich, and A. Mikhailov, "Multilayers of CdSe/CdS/ZnCdS core/wings/shell nanoplatelets integrated in a polymer waveguide," *IEEE Journal of Selected Topics in Quantum Electronics*, vol. 23, no. 5, pp. 1 – 8, 2017.

[28] O. Erdem, K. Gungor, B. Guzelturk, I. Tanriover, M. Sak, M. Olutas, D. Dede, Y. Kelestemur, and H. V. Demir, "Orientation-controlled nonradiative energy transfer to colloidal nanoplatelets: Engineering dipole orientation factor," *Nano Letters*, vol. 19, no. 7, pp. 4297 – 4305, 2019.

[29] B. E. A. Saleh and M. C. Teich, *Fundamentals of Photonics*. Hobojen, NJ: Wiley, 2007.

[30] S. V. Gaponenko, *Introduction to Nanophotonics*. New York: Cambridge University Press, 2010.

[31] J. A. McGuire, J. Joo, J. M. Pietryga, R. D. Schaller, and V. I. Klimov, "New aspects of carrier multiplication in semiconductor nanocrystals," *Accounts of Chemical Research*, vol. 41, no. 12, pp. 1810–1819, 2008.

[32] P. Kambhampati, "Hot exciton relaxation dynamics in semiconductor quantum dots: Radiationless transitions on the nanoscale," *The Journal of Physical Chemistry C*, vol. 115, no. 45, pp. 22089–22109, 2011.

[33] R. Dingle, W. Wiegmann, and C. H. Henry, "Quantum states of confined carriers in very thin $Al_xGa_{1-x}As$-GaAs-$Al_xGa_{1-x}As$ heterostructures," *Physical Review Letters*, vol. 33, no. 14, p. 827, 1974.

[34] L. E. Brus, "Interactions in small semiconductor crystallites: The size dependence of the lowest excited electronic state," *The Journal of Chemical Physics*, vol. 80, no. 9, pp. 4403–4409, 1984.

[35] A. I. Ekimov, A. L. Efros, and A. A. Onushchenko, "Quantum size effect in semiconductor microcrystals," *Solid State Communications*, vol. 56, no. 11, pp. 921–924, 1985.

[36] N. F. Borrelli, D. W. Hall, H. J. Holland, and D. W. Smith, "Quantum confinement effects of semiconducting microcrystallites in glass," *Journal of Applied Physics*, vol. 61, no. 12, pp. 5399–5409, 1987.

[37] N. Gaponik, D. V. Talapin, A. L. Rogach, K. Hoppe, E. V. Shevchenko, A. Kornowski, A. Eychmüller, and H. Weller, "Thiol-capping of CdTe nanocrystals: An alternative to organometallic synthetic routes," *The Journal of Physical Chemistry B*, vol. 106, no. 29, pp. 7177–7185, 2002.

[38] M. V. Kovalenko, M. Scheele, and D. V. Talapin, "Colloidal nanocrystals with molecular metal chalcogenide surface ligands," *Science*, vol. 324, no. 5933, pp. 1417–1420, 2009.

[39] J. I. Hollingsworth and V. I. Klimov, ""Soft" chemical synthesis and manipulation of semiconductor nanocrystals," in *Nanocrystal Quantum Dots* (V. I. Klimov, ed.), Boca Raton, FL: CRC Press, 2010.

[40] A. J. Nozik, "Quantum dot solar cells," *Physica E: Low-dimensional Systems and Nanostructures*, vol. 14, no. 1, pp. 115 – 120, 2002.

[41] O. E. Semonin, J. M. Luther, S. Choi, H.-Y. Chen, J. Gao, A. J. Nozik, and M. C. Beard, "Peak external photocurrent quantum efficiency exceeding

100% via MEG in a quantum dot solar cell," *Science*, vol. 334, no. 6062, pp. 1530–1533, 2011.

[42] J. Zhang, J. Gao, C. P. Church, E. M. Miller, J. M. Luther, V. I. Klimov, and M. C. Beard, "PbSe quantum dot solar cells with more than 6% efficiency fabricated in ambient atmosphere," *Nano Letters*, vol. 14, no. 10, pp. 6010–6015, 2014.

[43] J. R. Manders, L. Qian, A. Titov, J. Hyvonen, J. Tokarz-Scott, K. P. Acharya, Y. Yang, W. Cao, Y. Zheng, J. Xue, and P. H. Holloway, "High efficiency and ultra-wide color gamut quantum dot LEDs for next generation displays," *Journal of the Society for Information Display*, vol. 23, no. 11, pp. 523–528, 2015.

[44] B. Guzelturk, Y. Kelestemur, K. Gungor, A. Yeltik, M. Z. Akgul, Y. Wang, R. Chen, C. Dang, H. Sun, and H. V. Demir, "Stable and low-threshold optical gain in CdSe/CdS quantum dots: An all-colloidal frequency up-converted laser," *Advanced Materials*, vol. 27, no. 17, pp. 2741–2746, 2015.

[45] J. Roh, Y. S. Park, J. Lim, and V. I. Klimov, "Optically pumped colloidal-quantum-dot lasing in LED-like devices with an integrated optical cavity," *Nature Communications*, vol. 11, no. 1, p. 271, 2020.

[46] R. Yu, T. Ren, K. Sun, Z. Feng, G. Li, and C. Li, "Shape-controlled copper selenide nanocubes synthesized by an electrochemical crystallization method," *The Journal of Physical Chemistry C*, vol. 113, no. 25, pp. 10833–10837, 2009.

[47] L. Manna, D. J. Milliron, A. Meisel, E. C. Scher, and A. P. Alivisatos, "Controlled growth of tetrapod-branched inorganic nanocrystals," *Nature Materials*, vol. 2, no. 6, pp. 382–385, 2003.

[48] D. J. Milliron, S. M. Hughes, Y. Cui, L. Manna, J. Li, L.-W. Wang, and P. A. Alivisatos, "Colloidal nanocrystal heterostructures with linear and branched topology," *Nature*, vol. 430, no. 6996, pp. 190–195, 2004.

[49] X. Peng, L. Manna, W. Yang, J. Wickham, E. Scher, A. Kadavanich, and A. P. Alivisatos, "Shape control of CdSe nanocrystals," *Nature*, vol. 404, no. 6773, pp. 59–61, 2000.

[50] D. V. Talapin, J. H. Nelson, E. V. Shevchenko, S. Aloni, B. Sadtler, and A. P. Alivisatos, "Seeded growth of highly luminescent CdSe/CdS nanoheterostructures with rod and tetrapod morphologies," *Nano Letters*, vol. 7, no. 10, pp. 2951–2959, 2007.

[51] B. Mahler, B. Nadal, C. Bouet, G. Patriarche, and B. Dubertret, "Core/shell colloidal semiconductor nanoplatelets," *Journal of the American Chemical Society*, vol. 134, no. 45, pp. 18591–18598, 2012.

[52] A. Prudnikau, A. Chuvilin, and M. Artemyev, "CdSe/CdS nanoheteroplatelets with efficient photoexcitation of central CdSe region through epitaxially grown CdS wings," *Journal of the American Chemical Society*, vol. 135, no. 39, pp. 14476–14479, 2013.

[53] Y. Kelestemur, D. Dede, K. Gungor, C. F. Usanmaz, O. Erdem, and H. V. Demir, "Alloyed heterostructures of $CdSe_xS_{1-x}$ nanoplatelets with highly tunable optical gain performance," *Chemistry of Materials*, vol. 29, no. 11, pp. 4857–4865, 2017.

[54] Y. Kelestemur, B. Guzelturk, O. Erdem, M. Olutas, T. Erdem, C. F. Usanmaz, K. Gungor, and H. V. Demir, "$CdSe/CdSe_{1-x}Te_x$ core/crown heteronanoplatelets: Tuning the excitonic properties without changing the thickness," *The Journal of Physical Chemistry C*, vol. 121, no. 8, pp. 4650–4658, 2017.

[55] Y. Altintas, K. Gungor, Y. Gao, M. Sak, U. Quliyeva, G. Bappi, E. Mutlugun, E. H. Sargent, and H. V. Demir, "Giant alloyed hot injection shells enable ultralow optical gain threshold in colloidal quantum wells," *ACS Nano*, vol. 13, no. 9, pp. 10662–10670, 2019.

[56] A. A. Rossinelli, H. Rojo, A. S. Mule, M. Aellen, A. Cocina, E. De Leo, R. Schaublin, and D. J. Norris, "Compositional grading for efficient and

narrowband emission in CdSe-based core/shell nanoplatelets," *Chemistry of Materials*, vol. 31, no. 22, pp. 9567–9578, 2019.

[57] M. Sharma, K. Gungor, A. Yeltik, M. Olutas, B. Guzelturk, Y. Kelestemur, T. Erdem, S. Delikanli, J. R. McBride, and H. V. Demir, "Near-unity emitting copper-doped colloidal semiconductor quantum wells for luminescent solar concentrators," *Advanced Materials*, vol. 29, no. 30, p. 1700821, 2017.

[58] C. She, I. Fedin, D. S. Dolzhnikov, P. D. Dahlberg, G. S. Engel, R. D. Schaller, and D. V. Talapin, "Red, yellow, green, and blue amplified spontaneous emission and lasing using colloidal CdSe nanoplatelets," *ACS Nano*, vol. 9, no. 10, pp. 9475 – 9485, 2015.

[59] M. A. Boles, M. Engel, and D. V. Talapin, "Self-assembly of colloidal nanocrystals: From intricate structures to functional materials," *Chemical Reviews*, vol. 116, no. 18, pp. 11220–11289, 2016.

[60] K. Rajagopal and J. P. Schneider, "Self-assembling peptides and proteins for nanotechnological applications," *Current Opinion in Structural Biology*, vol. 14, no. 4, pp. 480 – 486, 2004.

[61] J. Wang, K. Liu, R. Xing, and X. Yan, "Peptide self-assembly: thermodynamics and kinetics," *Chemical Society Reviews*, vol. 45, no. 20, pp. 5589–5604, 2016.

[62] E. Winfree, F. Liu, L. A. Wenzler, and N. C. Seeman, "Design and self-assembly of two-dimensional DNA crystals," *Nature*, vol. 394, no. 6693, pp. 539–544, 1998.

[63] X. Sun, S. Hyeon Ko, C. Zhang, A. E. Ribbe, and C. Mao, "Surface-mediated DNA self-assembly," *Journal of the American Chemical Society*, vol. 131, no. 37, pp. 13248–13249, 2009.

[64] J. Kunzelman, B. R. Crenshaw, and C. Weder, "Self-assembly of chromogenic dyes: a new mechanism for humidity sensors," *Journal of Materials Chemistry*, vol. 17, no. 29, pp. 2989–2991, 2007.

[65] B. Heyne, "Self-assembly of organic dyes in supramolecular aggregates," *Photochemical & Photobiological Sciences*, vol. 15, no. 9, pp. 1103–1114, 2016.

[66] I. Langmuir, "Chemical reactions at low pressures," *Journal of the American Chemical Society*, vol. 37, no. 5, pp. 1139–1167, 1915.

[67] I. Langmuir, "The constitution and fundamental properties of solids and liquids. II. Liquids.," *Journal of the American Chemical Society*, vol. 39, no. 9, pp. 1848–1906, 1917.

[68] I. Langmuir, "The mechanism of the surface phenomena of flotation," *Transactions of the Faraday Society*, vol. 15, no. June, pp. 62–74, 1920.

[69] K. B. Blodgett, "Films built by depositing successive monomolecular layers on a solid surface," *Journal of the American Chemical Society*, vol. 57, no. 6, pp. 1007–1022, 1935.

[70] K. B. Blodgett and I. Langmuir, "Built-up films of barium stearate and their optical properties," *Physical Review*, vol. 51, no. 11, pp. 964–982, 1937.

[71] R. A. Hann, "Molecular structure and monolayer properties," in *Langmuir-Blodgett Films* (G. G. Roberts, ed.), New York: Springer US, 1990.

[72] M. Sugi, "Langmuir-Blodgett films - A course towards molecular electronics: A review," *Journal of Molecular Electronics*, vol. 1, pp. 3–17, 1985.

[73] J. Zasadzinski, R. Viswanathan, L. Madsen, J. Garnaes, and D. Schwartz, "Langmuir-Blodgett films," *Science*, vol. 263, no. 5154, pp. 1726–1733, 1994.

[74] T. Moriizumi, "Langmuir-Blodgett films as chemical sensors," *Thin Solid Films*, vol. 160, no. 1, pp. 413 – 429, 1988.

[75] S. Acharya, J. P. Hill, and K. Ariga, "Soft Langmuir-Blodgett technique for hard nanomaterials," *Advanced Materials*, vol. 21, no. 29, pp. 2959–2981, 2009.

[76] B. O. Dabbousi, C. B. Murray, M. F. Rubner, and M. G. Bawendi, "Langmuir-Blodgett manipulation of size-selected CdSe nanocrystallites," *Chemistry of Materials*, vol. 6, no. 2, pp. 216–219, 1994.

[77] C. B. Murray, C. R. Kagan, and M. G. Bawendi, "Self-organization of CdSe nanocrystallites into three-dimensional quantum dot superlattices," *Science*, vol. 270, no. 5240, pp. 1335–1338, 1995.

[78] B. Peng, G. Li, D. Li, S. Dodson, Q. Zhang, J. Zhang, Y. H. Lee, H. V. Demir, X. Yi Ling, and Q. Xiong, "Vertically aligned gold nanorod monolayer on arbitrary substrates: Self-assembly and femtomolar detection of food contaminants," *ACS Nano*, vol. 7, no. 7, pp. 5993–6000, 2013.

[79] S. M. Rupich, E. V. Shevchenko, M. I. Bodnarchuk, B. Lee, and D. V. Talapin, "Size-dependent multiple twinning in nanocrystal superlattices," *Journal of the American Chemical Society*, vol. 132, no. 1, pp. 289–296, 2010.

[80] B. Abecassis, M. D. Tessier, P. Davidson, and B. Dubertret, "Self-assembly of CdSe nanoplatelets into giant micrometer-scale needles emitting polarized light," *Nano Letters*, vol. 14, no. 2, pp. 710–715, 2014.

[81] B. Guzelturk, O. Erdem, M. Olutas, Y. Kelestemur, and H. V. Demir, "Stacking in colloidal nanoplatelets: Tuning excitonic properties," *ACS Nano*, vol. 8, no. 12, pp. 12524–12533, 2014.

[82] M. I. Bodnarchuk, M. V. Kovalenko, S. Pichler, G. Fritz-Popovski, G. Hesser, and W. Heiss, "Large-area ordered superlattices from magnetic wüstite/cobalt ferrite core/shell nanocrystals by doctor blade casting," *ACS Nano*, vol. 4, no. 1, pp. 423–431, 2010.

[83] T. Paik, D.-K. Ko, T. R. Gordon, V. Doan-Nguyen, and C. B. Murray, "Studies of liquid crystalline self-assembly of GdF_3 nanoplates by in-plane, out-of-plane SAXS," *ACS Nano*, vol. 5, no. 10, pp. 8322–8330, 2011.

[84] J. L. Baker, A. Widmer-Cooper, M. F. Toney, P. L. Geissler, and A. P. Alivisatos, "Device-scale perpendicular alignment of colloidal nanorods," *Nano Letters*, vol. 10, no. 1, pp. 195–201, 2010.

[85] C. B. Murray, C. R. Kagan, and M. G. Bawendi, "Synthesis and characterization of monodisperse nanocrystals and close-packed nanocrystal assemblies," *Annual Review of Materials Science*, vol. 30, no. 1, pp. 545–610, 2000.

[86] F. X. Redl, K.-S. Cho, C. B. Murray, and S. O'Brien, "Three-dimensional binary superlattices of magnetic nanocrystals and semiconductor quantum dots," *Nature*, vol. 423, no. 6943, pp. 968–971, 2003.

[87] K. Overgaag, W. Evers, B. de Nijs, R. Koole, J. Meeldijk, and D. Vanmaekelbergh, "Binary superlattices of PbSe and CdSe nanocrystals," *Journal of the American Chemical Society*, vol. 130, no. 25, pp. 7833–7835, 2008.

[88] H. Min, J. Zhou, X. Bai, L. Li, K. Zhang, T. Wang, X. Zhang, Y. Li, Y. Jiao, X. Qi, and Y. Fu, "Approach to fabricating a compact gold nanoparticle film with the assistance of a surfactant," *Langmuir*, vol. 33, no. 27, pp. 6732–6738, 2017.

[89] W. H. Evers, B. Goris, S. Bals, M. Casavola, J. de Graaf, R. van Roij, M. Dijkstra, and D. Vanmaekelbergh, "Low-dimensional semiconductor superlattices formed by geometric control over nanocrystal attachment," *Nano Letters*, vol. 13, no. 6, pp. 2317–2323, 2013.

[90] M. P. Boneschanscher, W. H. Evers, J. J. Geuchies, T. Altantzis, B. Goris, F. T. Rabouw, S. A. P. van Rossum, H. S. J. van der Zant, L. D. A. Siebbeles, G. Van Tendeloo, I. Swart, J. Hilhorst, A. V. Petukhov, S. Bals, and D. Vanmaekelbergh, "Long-range orientation and atomic attachment of nanocrystals in 2D honeycomb superlattices," *Science*, vol. 344, no. 6190, pp. 1377–1380, 2014.

[91] W. Walravens, E. Solano, F. Geenen, J. Dendooven, O. Gorobtsov, A. Tadjine, N. Mahmoud, P. P. Ding, J. P. C. Ruff, A. Singer, G. Roelkens, C. Delerue, C. Detavernier, and Z. Hens, "Setting carriers free: Healing faulty interfaces promotes delocalization and transport in nanocrystal solids," *ACS Nano*, vol. 13, no. 11, pp. 12774–12786, 2019.

[92] R. Momper, H. Zhang, S. Chen, H. Halim, E. Johannes, S. Yordanov, D. Braga, B. Blülle, D. Doblas, T. Kraus, M. Bonn, H. I. Wang, and A. Riedinger, "Kinetic control over self-assembly of semiconductor nanoplatelets," *Nano Letters*, 2020.

[93] T. Förster, "Zwischenmolekulare energiewanderung und fluoreszenz," *Annalen der Physik*, vol. 437, no. 1-2, pp. 55–75, 1948. English translation by R. S. Knox in *Biological Physics*. New York, NY: American Institute of Physics, 1993.

[94] J. R. Lakowicz, *Principles of Fluorescence Spectroscopy*. Singapore: Springer, 2007.

[95] R. Clegg, "Fluorescence resonance energy transfer," in *Fluorescence Imaging Spectroscopy and Microscopy* (X. F. Wang and B. Herman, eds.), Wiley, 1996.

[96] P. L. Hernandez-Martinez, A. O. Govorov, and H. V. Demir, "Generalized theory of Förster-type nonradiative energy transfer in nanostructures with mixed dimensionality," *The Journal of Physical Chemistry C*, vol. 117, no. 19, pp. 10203–10212, 2013.

[97] A. L. Rogach, T. A. Klar, J. M. Lupton, A. Meijerink, and J. Feldmann, "Energy transfer with semiconductor nanocrystals," *Journal of Materials Chemistry*, vol. 19, no. 9, pp. 1208–1221, 2009.

[98] D. Meadows and J. S. Schultz, "Fiber-optic biosensors based on fluorescence energy transfer," *Talanta*, vol. 35, no. 2, pp. 145 – 150, 1988.

[99] R. B. Sekar and A. Periasamy, "Fluorescence resonance energy transfer (FRET) microscopy imaging of live cell protein localizations," *Journal of Cell Biology*, vol. 160, pp. 629–633, 03 2003.

[100] R. L. Lu, N. L. Esmon, C. T. Esmon, and A. E. Johnson, "The active site of the thrombin-thrombomodulin complex. a fluorescence energy transfer measurement of its distance above the membrane surface.," *Journal of Biological Chemistry*, vol. 264, no. 22, pp. 12956–12962, 1989.

[101] Z. Shahrokh, A. S. Verkman, and S. B. Shohet, "Distance between skeletal protein 4.1 and the erythrocyte membrane bilayer measured by resonance energy transfer.," *Journal of Biological Chemistry*, vol. 266, no. 18, pp. 12082–12089, 1991.

[102] H.-h. Li, D. S. Lyles, M. J. Thomas, W. Pan, and M. G. Sorci-Thomas, "Structural determination of lipid-bound ApoA-I using fluorescence resonance energy transfer," *Journal of Biological Chemistry*, vol. 275, no. 47, pp. 37048–37054, 2000.

[103] E. W. Montroll, "Random walks on lattices. III. Calculation of first-passage times with application to exciton trapping on photosynthetic units," *Journal of Mathematical Physics*, vol. 10, no. 4, pp. 753–765, 1969.

[104] C. R. Kagan, C. B. Murray, M. Nirmal, and M. G. Bawendi, "Electronic energy transfer in CdSe quantum dot solids," *Phys. Rev. Lett.*, vol. 54, no. 12, pp. 1517–1520, 1996.

[105] J. Tian, H. Zhao, M. Liu, Y. Chen, and X. Quan, "Detection of influenza A virus based on fluorescence resonance energy transfer from quantum dots to carbon nanotubes," *Analytica Chimica Acta*, vol. 723, pp. 83 – 87, 2012.

[106] Z. S. Qian, X. Y. Shan, L. J. Chai, J. J. Ma, J. R. Chen, and H. Feng, "DNA nanosensor based on biocompatible graphene quantum dots and carbon nanotubes," *Biosensors and Bioelectronics*, vol. 60, pp. 64 – 70, 2014.

[107] A. R. Clapp, I. L. Medintz, J. M. Mauro, B. R. Fisher, M. G. Bawendi, and H. Mattoussi, "Fluorescence resonance energy transfer between quantum dot donors and dye-labeled protein acceptors," *Journal of the American Chemical Society*, vol. 126, no. 1, pp. 301–310, 2004.

[108] A. M. Dennis and G. Bao, "Quantum dot-fluorescent protein pairs as novel fluorescence resonance energy transfer probes," *Nano Letters*, vol. 8, no. 5, pp. 1439–1445, 2008.

[109] J. Lee, W. Bao, L. Ju, P. J. Schuck, F. Wang, and A. Weber-Bargioni, "Switching individual quantum dot emission through electrically controlling

resonant energy transfer to graphene," *Nano Letters*, vol. 14, no. 12, pp. 7115–7119, 2014.

[110] N. Taghipour, P. L. Hernandez Martinez, A. Ozden, M. Olutas, D. Dede, K. Gungor, O. Erdem, N. K. Perkgoz, and H. V. Demir, "Near-unity efficiency energy transfer from colloidal semiconductor quantum wells of CdSe/CdS nanoplatelets to a monolayer of MoS_2," *ACS Nano*, vol. 12, no. 8, pp. 8547–8554, 2018.

[111] H. M. Nguyen, O. Seitz, D. Aureau, A. Sra, N. Nijem, Y. N. Gartstein, Y. J. Chabal, and A. V. Malko, "Spectroscopic evidence for nonradiative energy transfer between colloidal CdSe/ZnS nanocrystals and functionalized silicon substrates," *Applied Physics Letters*, vol. 98, no. 16, p. 161904, 2011.

[112] A. Yeltik, B. Guzelturk, P. L. Hernandez-Martinez, A. O. Govorov, and H. V. Demir, "Phonon-assisted exciton transfer into silicon using nanoemitters: The role of phonons and temperature effects in Förster resonance energy transfer," *ACS Nano*, vol. 7, no. 12, pp. 10492–10501, 2013.

[113] Y. Ebenstein, T. Mokari, and U. Banin, "Quantum-dot-functionalized scanning probes for fluorescence-energy-transfer-based microscopy," *The Journal of Physical Chemistry B*, vol. 108, no. 1, pp. 93–99, 2004.

[114] Y.-S. Park, W. K. Bae, T. Baker, J. Lim, and V. I. Klimov, "Effect of Auger recombination on lasing in heterostructured quantum dots with engineered core/shell interfaces," *Nano Letters*, vol. 15, no. 11, pp. 7319–7328, 2015.

[115] K. Wu, Y.-S. Park, J. Lim, and V. I. Klimov, "Towards zero-threshold optical gain using charged semiconductor quantum dots," *Nature Nanotechnology*, vol. 12, no. 12, pp. 1140–1147, 2017.

[116] A. L. Efros, V. A. Kharchenko, and M. Rosen, "Breaking the phonon bottleneck in nanometer quantum dots: Role of Auger-like processes," *Solid State Communications*, vol. 93, no. 4, pp. 281 – 284, 1995.

[117] V. I. Klimov, A. A. Mikhailovsky, D. W. McBranch, C. A. Leatherdale, and M. G. Bawendi, "Quantization of multiparticle Auger rates in semiconductor quantum dots," *Science*, vol. 287, no. 5455, pp. 1011–1013, 2000.

[118] V. I. Klimov, S. A. Ivanov, J. Nanda, M. Achermann, I. Bezel, J. A. McGuire, and A. Piryatinski, "Single-exciton optical gain in semiconductor nanocrystals," *Nature*, vol. 447, no. 7143, pp. 441–446, 2007.

[119] C. Dang, J. Lee, C. Breen, J. S. Steckel, S. Coe-Sullivan, and A. Nurmikko, "Red, green and blue lasing enabled by single-exciton gain in colloidal quantum dot films," *Nature Nanotechnology*, vol. 7, no. 5, pp. 335–339, 2012.

[120] M. M. Adachi, F. Fan, D. P. Sellan, S. Hoogland, O. Voznyy, A. J. Houtepen, K. D. Parrish, P. Kanjanaboos, J. A. Malen, and E. H. Sargent, "Microsecond-sustained lasing from colloidal quantum dot solids," *Nature Communications*, vol. 6, no. 1, p. 8694, 2015.

[121] W. Xie, T. Stöferle, G. Raino, T. Aubert, S. Bisschop, Y. Zhu, R. F. Mahrt, P. Geiregat, E. Brainis, Z. Hens, and D. Van Thourhout, "On-chip integrated quantum-dot-silicon-nitride microdisk lasers," *Advanced Materials*, vol. 29, no. 16, p. 1604866, 2017.

[122] M. Sak, N. Taghipour, S. Delikanli, S. Shendre, I. Tanriover, S. Foroutan, Y. Gao, J. Yu, Z. Yanyan, S. Yoo, C. Dang, and H. V. Demir, "Coreless fiber-based whispering-gallery-mode assisted lasing from colloidal quantum well solids," *Advanced Functional Materials*, vol. 30, no. 1, p. 1907417, 2020.

[123] Y. Wang, K. S. Leck, V. D. Ta, R. Chen, V. Nalla, Y. Gao, T. He, H. V. Demir, and H. Sun, "Quantum dots: Blue liquid lasers from solution of CdZnS/ZnS ternary alloy quantum dots with quasi-continuous pumping," *Advanced Materials*, vol. 27, no. 1, pp. 168–168, 2015.

[124] M. Li, M. Zhi, H. Zhu, W.-Y. Wu, Q.-H. Xu, M. H. Jhon, and Y. Chan, "Ultralow-threshold multiphoton-pumped lasing from colloidal

nanoplatelets in solution," *Nature Communications*, vol. 6, no. 1, p. 8513, 2015.

[125] K. L. Shaklee and R. F. Leheny, "Direct determination of optical gain in semiconductor crystals," *Applied Physics Letters*, vol. 18, no. 11, pp. 475–477, 1971.

[126] K. L. Shaklee, R. E. Nahory, and R. F. Leheny, "Optical gain in semiconductors," *Journal of Luminescence*, vol. 7, pp. 284 – 309, 1973.

[127] A. G. Vitukhnovsky, V. S. Lebedev, A. S. Selyukov, A. A. Vashchenko, R. B. Vasiliev, and M. S. Sokolikova, "Electroluminescence from colloidal semiconductor CdSe nanoplatelets in hybrid organic-inorganic light emitting diode," *Chemical Physics Letters*, vol. 619, pp. 185 – 188, 2015.

[128] B. Liu, S. Delikanli, Y. Gao, D. Dede, K. Gungor, and H. V. Demir, "Nanocrystal light-emitting diodes based on type II nanoplatelets," *Nano Energy*, vol. 47, pp. 115 – 122, 2018.

[129] A. Yeltik, S. Delikanli, M. Olutas, Y. Kelestemur, B. Guzelturk, and H. V. Demir, "Experimental determination of the absorption cross-section and molar extinction coefficient of colloidal CdSe nanoplatelets," *The Journal of Physical Chemistry C*, vol. 119, no. 47, pp. 26768–26775, 2015.

[130] O. Erdem, M. Olutas, B. Guzelturk, Y. Kelestemur, and H. V. Demir, "Temperature-dependent emission kinetics of colloidal semiconductor nanoplatelets strongly modified by stacking," *The Journal of Physical Chemistry Letters*, vol. 7, no. 3, pp. 548–554, 2016.

[131] O. Erdem, S. Foroutan, N. Gheshlaghi, B. Guzelturk, Y. Altintas, and H. V. Demir, "Orientation-controlled construction of superstructures of atomically-flat nanocrystals: Pushing the limits of ultra-thin colloidal gain media." arXiv: 2005.10724 [physics.app-ph], 2020.

[132] K. Lambert, R. K. Capek, M. I. Bodnarchuk, M. V. Kovalenko, D. Van Thourhout, W. Heiss, and Z. Hens, "Langmuir-Schaefer deposition of quantum dot multilayers," *Langmuir*, vol. 26, no. 11, pp. 7732–7736, 2010.

[133] J. Roither, S. Pichler, M. V. Kovalenko, W. Heiss, P. Feychuk, O. Panchuk, J. Allam, and B. N. Murdin, "Two- and one-dimensional light propagations and gain in layer-by-layer-deposited colloidal nanocrystal waveguides," *Applied Physics Letters*, vol. 89, no. 11, p. 111120, 2006.

[134] E. A. Gaulding, B. T. Diroll, E. D. Goodwin, Z. J. Vrtis, C. R. Kagan, and C. B. Murray, "Deposition of wafer-scale single-component and binary nanocrystal superlattice thin films via dip-coating," *Advanced Materials*, vol. 27, no. 18, pp. 2846–2851, 2015.

[135] Y. Justo, I. Moreels, K. Lambert, and Z. Hens, "Langmuir-Blodgett monolayers of colloidal lead chalcogenide quantum dots: morphology and photoluminescence," *Nanotechnology*, vol. 21, p. 295606, jul 2010.

[136] F. Pietra, F. T. Rabouw, W. H. Evers, D. V. Byelov, A. V. Petukhov, C. de Mello Donegá, and D. Vanmaekelbergh, "Semiconductor nanorod self-assembly at the liquid/air interface studied by in situ gisaxs and ex situ TEM," *Nano Letters*, vol. 12, no. 11, pp. 5515–5523, 2012.

[137] M. Beck, M. Graczyk, I. Maximov, E.-L. Sarwe, T. G. I. Ling, M. Keil, and L. Montelius, "Improving stamps for 10 nm level wafer scale nanoimprint lithography," *Microelectronic Engineering*, vol. 61-62, pp. 441 – 448, 2002.

[138] G. Decher, "Fuzzy nanoassemblies: Toward layered polymeric multicomposites," *Science*, vol. 277, no. 5330, pp. 1232–1237, 1997.

[139] T. J. Halthur, P. M. Claesson, and U. M. Elofsson, "Stability of polypeptide multilayers as studied by in situ ellipsometry: Effects of drying and post-buildup changes in temperature and pH," *Journal of the American Chemical Society*, vol. 126, no. 51, pp. 17009–17015, 2004.

[140] P. T. Hammond, "Engineering materials layer-by-layer: Challenges and opportunities in multilayer assembly," *AIChE Journal*, vol. 57, no. 11, pp. 2928–2940, 2011.

[141] H. Kuhn, "Classical aspects of energy transfer in molecular systems," *The Journal of Chemical Physics*, vol. 53, no. 1, pp. 101–108, 1970.

[142] B. Guzelturk and H. V. Demir, "Near-field energy transfer using nanoemitters for optoelectronics," *Advanced Functional Materials*, vol. 26, no. 45, pp. 8158–8177, 2016.

[143] Z. Tang, B. Ozturk, Y. Wang, and N. A. Kotov, "Simple preparation strategy and one-dimensional energy transfer in cdte nanoparticle chains," *The Journal of Physical Chemistry B*, vol. 108, no. 22, pp. 6927–6931, 2004.

[144] M. Achermann, M. A. Petruska, S. Kos, D. L. Smith, D. D. Koleske, and V. I. Klimov, "Energy-transfer pumping of semiconductor nanocrystals using an epitaxial quantum well," *Nature*, vol. 429, no. 6992, pp. 642–646, 2004.

[145] A. P. Alivisatos, W. Gu, and C. Larabell, "Quantum dots as cellular probes," *Annual Review of Biomedical Engineering*, vol. 7, no. 1, pp. 55–76, 2005.

[146] L. Guo, T. D. Krauss, C. B. Poitras, M. Lipson, X. Teng, and H. Yang, "Energy transfer between colloidal semiconductor nanocrystals in an optical microcavity," *Applied Physics Letters*, vol. 89, no. 6, p. 061104, 2006.

[147] K. Becker, J. M. Lupton, J. Müller, A. L. Rogach, D. V. Talapin, H. Weller, and J. Feldmann, "Electrical control of Förster energy transfer," *Nature Materials*, vol. 5, no. 10, pp. 777–781, 2006.

[148] D. M. Willard, L. L. Carillo, J. Jung, and A. Van Orden, "CdSe/ZnS quantum dots as resonance energy transfer donors in a model protein-protein binding assay," *Nano Letters*, vol. 1, no. 9, pp. 469–474, 2001.

[149] I. L. Medintz, A. R. Clapp, H. Mattoussi, E. R. Goldman, B. Fisher, and J. M. Mauro, "Self-assembled nanoscale biosensors based on quantum dot FRET donors," *Nature Materials*, vol. 2, no. 9, pp. 630–638, 2003.

[150] P. G. Wu and L. Brand, "Resonance energy transfer: Methods and applications.," *Analytical Biochemistry*, vol. 218, no. 1, pp. 1–13, 1994.

[151] W. J. I. De Benedetti, M. T. Nimmo, S. M. Rupich, L. M. Caillard, Y. N. Gartstein, Y. J. Chabal, and A. V. Malko, "Efficient directed energy

transfer through size-gradient nanocrystal layers into silicon substrates," *Advanced Functional Materials*, vol. 24, no. 31, pp. 5002–5010, 2014.

[152] R. S. Swathi and K. L. Sebastian, "Long range resonance energy transfer from a dye molecule to graphene has (distance)$^{-4}$ dependence," *The Journal of Chemical Physics*, vol. 130, no. 8, p. 086101, 2009.

[153] F. Prins, A. J. Goodman, and W. A. Tisdale, "Reduced dielectric screening and enhanced energy transfer in single- and few-layer MoS_2," *Nano Letters*, vol. 14, no. 11, pp. 6087–6091, 2014.

[154] P. L. Hernandez-Martinez, A. O. Govorov, and H. V. Demir, "Förster-type nonradiative energy transfer for assemblies of arrayed nanostructures: Confinement dimension vs stacking dimension," *The Journal of Physical Chemistry C*, vol. 118, no. 9, pp. 4951–4958, 2014.

[155] E. Shafran, B. D. Mangum, and J. M. Gerton, "Energy transfer from an individual quantum dot to a carbon nanotube," *Nano Letters*, vol. 10, no. 10, pp. 4049–4054, 2010.

[156] M. Pelton, "Modified spontaneous emission in nanophotonic structures," *Nature Photonics*, vol. 9, no. 7, pp. 427–435, 2015.

[157] H. M. Nguyen, O. Seitz, W. Peng, Y. N. Gartstein, Y. J. Chabal, and A. V. Malko, "Efficient radiative and nonradiative energy transfer from proximal CdSe/ZnS nanocrystals into silicon nanomembranes," *ACS Nano*, vol. 6, no. 6, pp. 5574–5582, 2012.

[158] L. Novotny and B. Hecht, *Principles of Nano-Optics*. New York: Cambridge University Press, 2006.

[159] H. Htoon, J. A. Hollingworth, A. V. Malko, R. Dickerson, and V. I. Klimov, "Light amplification in semiconductor nanocrystals: Quantum rods versus quantum dots," *Applied Physics Letters*, vol. 82, no. 26, pp. 4776–4778, 2003.

[160] Y. Gao, X. Zhao, Y. Wang, R. Chen, E. Mutlugun, K. E. Fong, S. T. Tan, C. Dang, X. W. Sun, H. Sun, *et al.*, "Observation of polarized gain from aligned colloidal nanorods," *Nanoscale*, vol. 7, no. 15, pp. 6481–6486, 2015.

[161] B. T. Diroll, D. V. Talapin, and R. D. Schaller, "Violet-to-blue gain and lasing from colloidal CdS nanoplatelets: Low-threshold stimulated emission despite low photoluminescence quantum yield," *ACS Photonics*, vol. 4, no. 3, pp. 576–583, 2017.

[162] B. Guzelturk, M. Pelton, M. Olutas, and H. V. Demir, "Giant modal gain coefficients in colloidal II-VI nanoplatelets," *Nano Letters*, vol. 19, no. 1, pp. 277–282, 2019.

[163] Y. Chan, J.-M. Caruge, P. T. Snee, and M. G. Bawendi, "Multiexcitonic two-state lasing in a CdSe nanocrystal laser," *Applied Physics Letters*, vol. 85, no. 13, pp. 2460–2462, 2004.

[164] Y. Altintas, U. Quliyeva, K. Gungor, O. Erdem, Y. Kelestemur, E. Mutlugun, M. V. Kovalenko, and H. V. Demir, "Highly stable, near-unity efficiency atomically flat semiconductor nanocrystals of CdSe/ZnS hetero-nanoplatelets enabled by ZnS-shell hot-injection growth," *Small*, vol. 15, no. 8, p. 1804854, 2019.

[165] L. Zhang, H. Yang, B. Yu, Y. Tang, C. Zhang, X. Wang, M. Xiao, Y. Cui, and J. Zhang, "Low-threshold amplified spontaneous emission and lasing from thick-shell CdSe/CdS core/shell nanoplatelets enabled by high-temperature growth," *Advanced Optical Materials*, vol. 8, no. 4, p. 1901615, 2020.

[166] A. K. Sheridan, G. A. Turnbull, A. N. Safonov, and I. D. W. Samuel, "Tuneability of amplified spontaneous emission through control of the waveguide-mode structure in conjugated polymer films," *Phys. Rev. B*, vol. 62, no. 18, pp. R11929–R11932, 2000.

[167] E. M. Calzado, J. M. Villalvilla, P. G. Boj, J. A. Quintana, and M. A. Diaz-Garcia, "Tuneability of amplified spontaneous emission through control of

the thickness in organic-based waveguides," *Journal of Applied Physics*, vol. 97, no. 9, p. 093103, 2005.

[168] A. Yariv and P. Yeh, *Photonics: Optical Electronics in Modern Communications*. New York: Oxford University Press, 2007.